

UNIVERSIDAD DE CONCEPCION

Facultad de Ingeniería

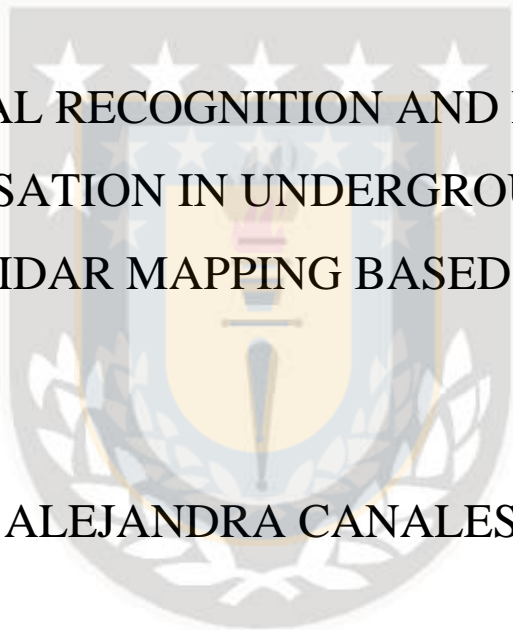
Departamento de Ingeniería Metalúrgica

Profesor Patrocinante

Prof. Constanza Paredes Bujes

Ingeniero Supervisor

Dr. Ewan Sellers



**STRUCTURAL RECOGNITION AND ROCK MASS
CHARACTERISATION IN UNDERGROUND MINES: A
UAV AND LIDAR MAPPING BASED APPROACH**

CATALINA ALEJANDRA CANALES VALLEJOS

Informe de Memoria de Título para optar al Título de
Ingeniera Civil de Minas

Febrero 2019



Porque desde donde estás, sé que gritas:

!! Cata, Cata, Ra, Ra, Ra!!

Te amo Abuelo

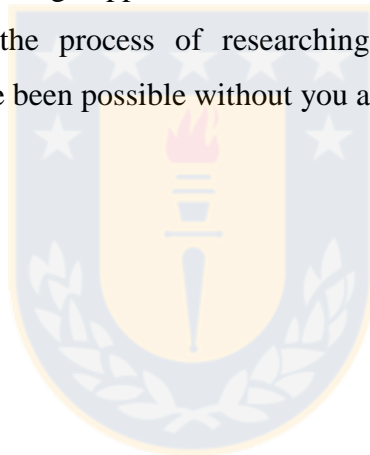
Acknowledgments

I would first like to thank my tutor Prof. Constanza Paredes Bujes and my supervisor Dr. Ewan Sellers, without you both i wouldnt have had such an amazing opportunity. Thanks to all the friends I made in CSIRO, you were like a family for me.

I also would like to thank my university friends, the department personnel, professors and all the beautiful people I met during these six years, you made from this experience one the best stages of my life.

Finally, I must express my very profound gratitude to my parents and grandparents, I know it was hard but we did it. To the rest of my family; my sister, aunt, uncle and cousins for been always with me, many times you believed more in me than I did. Thanks to all of you for providing me with unfailing support and continuous encouragement throughout my years of study and through the process of researching and writing this thesis. This accomplishment would not have been possible without you all. Thank you.

Catalina



Abstract

The geotechnical challenges in underground mining from a productive and stability point of view, make it necessary to incorporate tools that allow for the safe and quick evaluation of the operation of the mines. The purpose of this research is to test and validate the use of a new type of technology for these conditions and open the way to a new source of information.

Hovermap, a tool developed by the robotics area of CSIRO, Data61, combines the autonomous management of a drone with the ability to generate 3D representations using LiDAR, a remote sensing technique that allows the creation of high density and quality point clouds, using light pulses to estimate distances and location.

In the research two case studies are carried out; the first of them concentrated in the identification of geological structures and validation of the new version of Sirovision software for point clouds, comparing its results with the automatic extraction software, DSE. Once the structures have been identified, the results are analysed to determine the potential of their use in underground excavation stability evaluations.

The second case study is a comparison between data collected by the mine with traditional methods such as CMS and Core logging, passing also through a blasting simulation to determine the factors causing Overbreak and Underbreak without success. In the case of CMS the analysis focuses on the quality of surface representation and volume measurement, meanwhile, for Core Logging in a complete study of wall stability comparing the structures obtained in the sampling campaign against those identified with Hovermap.

Finally, the quality of the scans, in terms of recognition of geological structure for geotechnical purposes, is compared between both cases through an analysis of trajectories and exposure times of the drones, estimating that in order to achieve an optimal and reliable scan. The drone must take care to maintain the SEV or speed ratio, this suggests the incorporation of "static" scanning points within the flight, a flight velocity between 0.12 – 0.2 meters per second when this is not possible, a distance from the walls no higher than 5 meters and also is possible to conclude that the relationship between these variables; SEV, speed and distance is the key to get good representations.

Resumen

Los desafíos geotécnicos en minería subterránea, tanto a nivel productivo como de estabilidad hacen necesaria la incorporación de herramientas que permitan evaluar el funcionamiento de faenas de una forma segura y rápida. El propósito de esta investigación es probar y validar la utilización de un nuevo tipo de tecnología para estas condiciones y abrir el paso a una nueva fuente de información. Hovermap, una herramienta desarrollada por el área de robótica de CSIRO, Data61. Combina el manejo autónomo de un dron con la habilidad de generar representaciones en 3D usando LiDAR, técnica de teledetección que permite crear nubes de puntos de alta densidad y calidad, utilizando pulsos de luz para estimar distancias y ubicación.

En la investigación se realizan dos casos de estudio; el primero de ellos concentrado en la identificación de estructuras geológicas y validación de la nueva versión del software Sirovision para nubes de puntos para caracterización de macizos rocosos, comparando sus resultados con el programa de extracción automática, DSE. Una vez identificadas las estructuras los resultados son analizados, para determinar el potencial del uso de ellos en evaluaciones de estabilidad de excavaciones subterráneas.

El segundo caso de estudio es una comparación entre datos recopilados por la mina con métodos tradicionales como lo son CMS y Core logging, pasando también por una simulación de tronadura para determinar los factores causantes de sobreexcavación y subexcavación sin éxito. En el caso de CMS el análisis se enfoca en la calidad de la representación de superficies y medición de volúmenes, mientras tanto, para Core Logging en un estudio completo de estabilidad de paredes comparando las estructuras obtenidas en la campaña de muestreo contra las extraídas gracias a Hovermap.

Para finalizar, la calidad de los escaneos, en cuanto a reconocimiento de estructura geológicas con fines, es comparado entre ambos casos a través de un análisis de trayectorias y tiempos de exposición de los drones, estimando que para poder lograr un escaneo óptimo y confiable para propósitos geotécnicos o de reconocimiento estructural el dron debe cuidar mantener el SEV o la relación velocidad, patrón y distancia a la hora de realizar el vuelo, viajando a una velocidad no mayor a 2 metros por segundo y a una distancia de las paredes no mayor a 5 metros, lo que sugiere la incorporación de puntos de escaneo “estático” dentro del vuelo y también concluye que la relación entre estas variables; SEV, velocidad y distancia es la clave para lograr buenas representaciones.

Contents

| | |
|---|----|
| 1. Introduction | 15 |
| 1.1 Project Background | 15 |
| 1.2 Objectives and Scopes | 16 |
| 1.2.1 Research Questions | 16 |
| 1.2.2 Specific Objectives | 16 |
| 1.2.3 Significance and relevance to industry | 17 |
| 2. General Background | 18 |
| 2.1 Rock mechanics | 18 |
| 2.2 Sublevel Stopping | 18 |
| 2.3 Stope stability | 21 |
| 2.4 Stopes Drill and Blast | 25 |
| 2.4.1 Background | 25 |
| 2.4.2 Blast design and Geological structures | 26 |
| 2.4.3 Blast design | 28 |
| 3. General Review of Mapping Techniques in Underground Mines | 31 |
| 3.1 Structural mapping background | 31 |
| 3.2 Short overview of mapping techniques in underground mines | 32 |
| 3.3 Traditional mapping techniques in underground mines | 33 |
| 3.3.1 Core Logging | 33 |
| 3.3.2 Scanline Sampling | 35 |
| 3.3.3 Window or Cell Sampling | 36 |
| 3.4 Remote sensing techniques | 37 |
| 3.4.1 Photogrammetry | 37 |
| 3.4.2 LiDAR sampling technique | 39 |
| 3.5 Hovermap: A tool for mapping in unexpected places | 42 |
| 3.5.1 Short Overview of remote sensing in stopes underground mines | 42 |
| 3.5.2 Cavity Monitoring Surveys | 43 |
| 3.5.3 Hovermap | 45 |
| 3.5.4 Current applications of UAVs and HM | 46 |
| 4. Visualisation and Recognition Software | 48 |
| 4.1 Background | 48 |
| 4.2 CloudCompare | 48 |
| 4.3 Discontinuity Set Extractor | 48 |
| 4.4 Sirovision | 49 |

| | |
|--|-----|
| 5. Research Methodology | 51 |
| 5.1 Research context | 51 |
| 5.2 Presentation case studies | 51 |
| 5.2.1 Case Study 1 | 51 |
| 5.2.2 Case Study 2 | 52 |
| 5.3 Structural analysis | 54 |
| 5.4 Blasting energy distribution | 54 |
| 5.5 CMS versus Hovermap | 54 |
| 5.6 First Case Study | 55 |
| 5.6.1 Structural recognition | 55 |
| 5.6.2 Semiautomatic versus Automatic | 56 |
| 5.6.3 Rock mass characterisation | 57 |
| 5.7 Second Case Study | 58 |
| 5.7.2 Stability analysis | 59 |
| 5.7.3 Energy distribution | 60 |
| 5.7.4 HM Comparison to CMS | 63 |
| 5.8 Case 1 and Case 2: Comparison of resolution | 64 |
| 5.8.1 First analysis | 64 |
| 5.8.2 Second analysis | 64 |
| 6. Results Analysis | 66 |
| 6.1 First Case Study | 66 |
| 6.1.1 Structural recognition | 66 |
| 6.2 Second Case Study | 70 |
| 6.2.1 Structural recognition | 70 |
| 6.2.2 Stability analysis | 72 |
| 6.2.3 Energy distribution | 74 |
| 6.3 Case 1 and Case 2: Point clouds difference | 78 |
| 6.3.1 First analysis | 78 |
| 6.3.2 Second analysis | 83 |
| 7. Conclusions | 84 |
| 8. Future work and recommendations | 86 |
| 9. References | 87 |
| Appendix A | 92 |
| Appendix B | 94 |
| Appendix C | 97 |
| Appendix D | 101 |

Appendix E 104
Appendix F 105



List of Figures

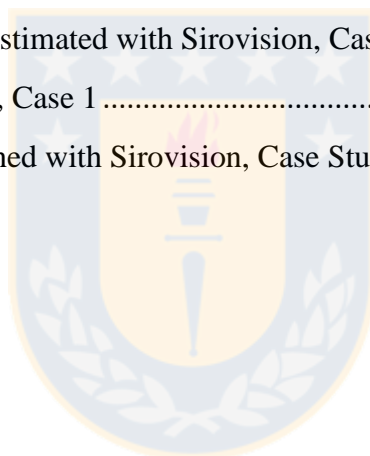
| | |
|--|----|
| Figure 1. Stable shape of stopes, relation between height and width [6]..... | 21 |
| Figure 2. RQD orientation bias, core run perpendicular to structures | 22 |
| Figure 3. RQD orientation bias, core run parallel to structures | 23 |
| Figure 4. Length influence in RQD | 23 |
| Figure 5. Extended Mathews stability graph [16]..... | 25 |
| Figure 6. Crack formation around the blasthole [22]..... | 28 |
| Figure 7. True toe spacing and effective toe spacing [17]..... | 29 |
| Figure 8. Factors influencing the RM behaviour [2] | 32 |
| Figure 9. Exploration and Underground drilling campaigns [6]..... | 34 |
| Figure 10. Secondary drilling campaign for characterisation and ore distribution estimation [6]..... | 34 |
| Figure 11. Example of camera positions for distortion correction | 35 |
| Figure 12. Example of scanline photograph for analysis [6] | 36 |
| Figure 13. Window sampling example with the three types of classification | 37 |
| Figure 14. Photogrammetry camera position to correct distortion and create a 3D model [32] | 38 |
| Figure 15. Distance measurement effect; a) Higher distance increase de angular distance between light pulses; and b) Lower distance provides more detail | 41 |
| Figure 16. Problem of angle incidence with LiDAR | 42 |
| Figure 17. Stope access method, lateral access [49]..... | 43 |
| Figure 18. Point cloud of a mine drift captured by V-SCAN3D [52]..... | 44 |
| Figure 19. Wire frame scan performed by (a) Traditional CMS; and, (b) By V-SAN3D [52]..... | 45 |
| Figure 20. Hovermap approach based on the combination of three main technologies | 45 |
| Figure 21. Hovermap, LiDAR tool mounted at the bottom of the drone..... | 46 |
| Figure 22. Stope A point cloud visualisation: a) Isometric view; b) Roof. | 52 |
| Figure 23. Stope B point cloud visualisation, coloured by depth were red indicates the higher zone and blue the deeper..... | 52 |
| Figure 24. Stope B location and adjacent stopes | 53 |
| Figure 25. HW Case Study 1, CC visualisation..... | 56 |
| Figure 26. Sirovision3D visualisation with zoom, a) Trace in the HW and b) Planes in the HW | 56 |

| | |
|--|----|
| Figure 27. Stope B; a Designed Stope; b) Designed Stope and final shape difference; and c) Final Shape scanned with CMS | 58 |
| Figure 28. Stope B point cloud; a) East Side inside view; b) Isometric view complete stope; and c) West Side inside view | 59 |
| Figure 29. . Rings involved in the UB; a) Designed stope and blastholes disposition; b) Final shape and evident UB | 60 |
| Figure 30. Rings involved on a good performance; a) Designed stope and blasthole disposition; b) Final shape | 61 |
| Figure 31. Dip angle difference between JKSimBlast and company design..... | 62 |
| Figure 32. a) Joint sets visualisation; and b) Planes poles concentration estimated with DSE67 | |
| Figure 33. a) Joint sets visualisation; and b) Planes poles concentration estimated with Sirovision | 68 |
| Figure 34. Histogram of spacing per set calculated with Sirovision, Case 1..... | 69 |
| Figure 35. a) Joint sets visualisation; and b) Planes poles concentration estimated with Sirovision, Case2 | 70 |
| Figure 36.a) Planes estimated with core logging; and b) Plane continuation obtained with Sirovision | 71 |
| Figure 37. a) RQD estimated with core logging; and b) Joint concentration calculated with Sirovision | 72 |
| Figure 38. Spacing per set calculated with Sirovision, Case 2 | 73 |
| Figure 39. a) Isometric view; and b) plan view of energy distribution in the UB zone, Stope B | 75 |
| Figure 40. a) Plan view; and b) Front view of energy distribution in the zone with good performance, Stope B..... | 76 |
| Figure 41. Volume measurements a) CMS mesh; and b) HM mesh | 77 |
| Figure 42. Point cloud obtained with HM (green) against point cloud generated with CMS (black) | 78 |
| Figure 43. Point density a) HW Case 2; b) HW Case 1. Zones with the similar density represented by red squares | 79 |
| Figure 44. Velocity during the flight; green zone shows an “Optimum” performance, Case 1 | 80 |
| Figure 45. Distance to the wall during the flight; green zone shows an “Optimum” performance, Case 1..... | 80 |
| Figure 46. Range during the flight; green zone shows an “Optimum” performance, Case 1 .. | 81 |

| | |
|---|-----|
| Figure 47. a)Limited trajectory, zones normally scanned (green), zones with shadow and angular obstruction(red); and b) Trajectory includes a flight along the stope to avoid shadow and angular obstruction..... | 82 |
| Figure 48. Relationship between Volumetric joint count and RQD [2] | 92 |
| Figure 49. Stress factor A, Stability number [2] | 92 |
| Figure 50. Influence of joint orientation - factor B, Stability number [2] | 92 |
| Figure 51. Determination gravity effect - Factor C, Stability number [2]..... | 93 |
| Figure 52. Determination of sliding effect on critical joint - Factor C, Stability number [2].. | 93 |
| Figure 53. a) Isometric view Stope A; and b) HW view of Stope A | 94 |
| Figure 54. Geologic structures identified with core logging, lateral view..... | 94 |
| Figure 55. Set 1, HW Case Study 1 | 95 |
| Figure 56. Set 2, HW Case Study 1 | 95 |
| Figure 57. Set 3, HW Case Study 1 | 96 |
| Figure 58. UB Section a) Inside view; and b) Outside view. | 97 |
| Figure 59. Mathew's Graph Analysis, Study Case 2 | 100 |
| Figure 60. JKSimblast Energy distribution scale..... | 101 |
| Figure 61. Plan view energy distribution UB zone; every 4 meters from 314mLv until 282mLv | 102 |
| Figure 62. Plan view energy distribution" Good Performance" zone; every 4 meters from 264mLv until 280mLv | 103 |
| Figure 63. Volume measurement with lower density and faster interpolation process..... | 104 |
| Figure 64. Difference in the point cloud density; a) HM scan; and b) CSM scan..... | 104 |
| Figure 65. Drone trajectories, Case 2..... | 105 |
| Figure 66. First scan; a) Point cloud results; and b) Point cloud density, Case 2..... | 106 |
| Figure 67. First scan density distribution, Case 2 | 106 |
| Figure 68. Second scan; a) Point cloud results; and b) Point cloud density, Case 2 | 107 |
| Figure 69. Second scan density distribution, Case 2 | 107 |
| Figure 70. Drone trajectory, Case 1 | 108 |
| Figure 71. HM scan; a) Point cloud results; and b) Point cloud density, Case 1..... | 108 |
| Figure 72. HM scan density distribution, Case 1 | 109 |
| Figure 73. Range calculation for Track 1 | 109 |
| Figure 74. Range calculation for Track 2 | 110 |
| Figure 75. Range calculation for Track 3 | 110 |

List of Tables

| | |
|---|----|
| Table 1. Stope B geotechnical properties | 59 |
| Table 2. Ring information to set up the blast..... | 61 |
| Table 3. Angles adjustment to work with JKSimBlast | 62 |
| Table 4. Volume measurements performed with CMS | 63 |
| Table 5. Joint sets determined with DSE in the HW | 66 |
| Table 6. Joint sets estimated with Sirovision in the HW, Case1 | 68 |
| Table 7. Comparison and angular difference between results obtained with DSE and Sirovision | 68 |
| Table 8. RQD and Sn factors estimated with Sirovision, set influence | 69 |
| Table 9. Joint sets estimated with Sirovision in the HW, Case 1 | 70 |
| Table 10. Joint sets estimated with Sirovision in the Stope B HW, Case 2..... | 73 |
| Table 11. RQD and Sn factors estimated with Sirovision, Case 2 | 74 |
| Table 12. Track analysis results, Case 1 | 83 |
| Table 13. GS information obtained with Sirovision, Case Study 2..... | 98 |



List of Equations

| | |
|---|-----|
| Equation 1. Modified Q | 22 |
| Equation 2. Estimation volumetric joint count factor | 24 |
| Equation 3. Rock Quality Designation estimation using the volumetric factor | 24 |
| Equation 4. Stability Number | 24 |
| Equation 5. Estimation of S factor or hydraulic radius..... | 24 |
| Equation 6. Distance between two points in 3D space | 105 |



Nomenclature

| | |
|--------------|--|
| AGA | AngloGold Ashanti |
| CC | CloudCompare |
| CMS | Cavity Monitoring Surveys |
| CSIRO | Commonwealth Scientific and Industrial Research Organisation |
| DSE | Discontinuity Set Extractor Software |
| FW | Foot Wall |
| GPS | Global Positioning System |
| GS | Geological Structures |
| HM | Hovermap |
| HR | Hydraulic Radius |
| HW | Hanging Wall |
| JKMRC | Julius Kruttschnitt Mineral Research Centre |
| LiDAR | Light Detection And Ranging |
| N | Stability Number |
| OB | Overbreak |
| Q' | Barton's Q modified |
| RM | Rock Mass |
| RQD | Rock Quality Designation |
| SEV | Sampling Effort Variable |
| SLAM | Simultaneous Localisation and Mapping |
| SLS | Sub Level Stoping |
| UB | Underbreak |
| UAV | Unmanned Aerial Vehicle |

1. Introduction

1.1 Project Background

In the current economic background, mining companies are under pressure to increase production in an efficient way, which means, to have the capacity of meeting the demand using the least amount of in situ resources. Rocks mechanics as the science that studies the behaviour of the rock mass [1] has been updated over the years and now integrates the concept of efficiency, providing tools that allow safe, fast and informed operations, positively affecting the entire value chain from its base.

One of the methods to improve efficiency is to predict the behaviour of the operation through an increment of information and a better knowledge of the geotechnical conditions, environment and material that it will be extracted. This principle in combination with rock mechanics is being applied to mitigate two common issues in underground mines, specifically in Sublevel Stopping (SLS) extractions, with direct consequences in the efficiency: Overbreak (OB) and Underbreak (UB)[2, 3]. Both result in an increase of cost, time and risks. To avoid these issues, it is crucial to predict the key rock mechanics drivers that influence the performance of the stopes, in particular those parameters related to discontinuities, such as orientation, frequency, persistency and spacing [4, 5].

Currently, the estimation of these factors can only be done in zones with direct access (tunnels, stables caves), allowing visual recognition and simple measurements. This leaves aside sectors with limited/complex access such as stopes, hindering possible economic benefits. Is here where the use of a new and ground-breaking remote sensing technique, Hovermap (HM), opens a new field of possibilities, enabling the study of geological features and stope performance in complex places that can't be reach by personnel or other remote technologies.

HM combines three main technologies: Drones, LiDAR and Autonomy to acquire accurate information in a safe and fast way. The key objectives of this study are to demonstrate the capability of HM mapping in:

1. Performing a geological characterisation inside the stopes (recognition of principal discontinuities).
2. Assessing the stope performance (difference of volumes and blasting performance through the comparison between energy distribution and final shape).

3. Analyse the advantages of this technology against the technology and systems already in use for geotechnical purposes in underground mines.

1.2 Objectives and Scopes

1.2.1 Research Questions

The main research questions are:

1. Can HM generate an accurate mapping of the stope surfaces to evaluate the stope performance and identify geological structures?
2. Is the information obtained with HM suitable for a process of continuous improvement?

1.2.2 Specific Objectives

1. To analyse the drone trajectory and data quality, demonstrating the increased capabilities and accuracy of HM over other remote technologies such as Caving Monitoring System (CMS) and traditional mapping techniques.
2. To evaluate the results obtained with HM and CMS in a case study, “Stope A”, elaborating a comparison between them.
3. To extract the major geological structures, demonstrating the level of detail and different applications of the information obtained with HM in assessments of blasting performance and stability analysis as a reconciliation tool with two case studies, “Stope A” and “Stope B”.
4. To perform a stability analysis to evidence and verify the ability of HM maps to provide geological characterisation with the utilisation of Sirovision to estimate stopes stability.
5. To develop a comparison between the RQD values obtained with Core Logging and HM to validate the use of Sirovision Beta version for geological structure recognition and show the compatibility with point clouds.
6. To suggest a new approach: “Minesweeper”, which demonstrates how this technology can be implemented during the entire process of extraction, enabling continuous improvements on an optimisation process.

1.2.3 Significance and relevance to industry

Presently, the extraction of minerals in open pit and underground labours is on race to improve the efficiency. This happens because of the current operational conditions and characteristics of ore extraction: deposits are located in increasingly deep areas and have lower grades, increasing the extraction and processing costs.

One of the ways to improve the efficiency is the implementation of a well-informed extraction chain, as more information allows for more accurate and precise operations. The first stage in all projects is the drilling campaign where the grades and geological features are determined; these processes will be repeated in a small scale as the extraction progresses followed by a visual inspection and recognition process to complement the initial rock mass characterisation. All these stages aim to improve the knowledge of the rock mass attributes and with that, the outcomes of the rock mass behaviour prediction. In this context, What happens with the characterisation in those areas of difficult, limited or non-access? This question is key in underground mines with a SLS extraction method, where those conditions are common. Usually for these cases, the answer will be either additional exploration drilling to obtain more information, incurring in additional costs, risks and time-consuming tasks or continuing with the extraction with limited data obtained from past drilling campaigns and mapping from accessible zones.

To avoid these issues, it is necessary to innovate and create new information sources.

2. General Background

2.1 Rock mechanics

The Rock Mass (RM) can be defined as a “Three dimensional discontinuous medium that can be formed by an assembly of blocks with the potential of being disaggregated during the excavation process”[6]. In this context, the size, shape and degree of interlock of the blocks are functions of the distribution and nature of geological structures (GS).

Geological structures are discontinuities such faults, joints, micro and macro fractures that can be generated before or after the excavation process. These structures represent planes of weakness through the rock mass, their incidence in the rock mass behaviour is directly dependent on a scale effect: from the perspective of rock strength and deformability, this effect is a decrease of the RM strength and changes in rock deformation properties with an increase in the volume studied. This happens because a larger volume has a higher probability of containing defects and structures within the RM. The study of these properties is part of Rock Mechanics, a branch of geomechanics that studies the geologic properties of the rock mass and their behaviour under different stress conditions.

Rock Mechanics is one of the most important disciplines for mining projects, especially for underground labours including SLS, key to assess the stability and achieve the required performance.

2.2 Sublevel Stopping

2.2.1 Background

Several parameters, conditions and characteristics determine the extraction method in underground conditions, with the rock mass stability as one of the most important factors.

Stable rock masses allow extensive zones of exposure without the need of artificial support, enabling the application of self-supported openings methods. On these methods, the ore is removed leaving an open gap in middle of the RM and depending on the RM stability conditions, the cavity can be left empty or filled after the operations. During the process of extraction and for a period after it is finished, the overlaying load is redistributed through the rock mass and supported by the side walls and pillars [6].

SLS is a well-known self-supported method, used to extract massive or tabular, often steeply dipping, competent orebodies surrounded by competent host rocks [7]. This method offers several advantages including:

- Low cost and efficient non-entry production operations where direct contact with the extraction it is not necessary.
- Highly mechanised production systems.
- High production rates with a minimum level of workers.

On the other hand, SLS key disadvantage is:

- The need for a high level of development infrastructure to start the production, which translates in a high initial capital investment (however almost all the developments tend to occur within the orebody).

2.2.2 Stopes

The basic components of extraction of SLS are stopes with a box geometry, their performance controls the success of the operation.

The stope performance is measured as the ability to achieve a maximum extraction with minimal dilution and ore losses. Dilution is defined as any material (waste or backfill) which comes into an ore flow, reducing its value and ore losses are defined as unrecoverable economic portions of the ore left inside a stope after the extraction is finished [7, 8]. The two practical measurements designed to assess the stope performance are:

1. Overbreak (OB): Defined as the volume of rock by which the actual stope shape exceeds the planned extracted volume, extracting waste material and decreasing the ore grade[2]. In some cases can affect the stope stability, changing the direction of the main stresses, veering from the desired stress redistribution in magnitude and direction.
2. Underbreak (UB): Defined as the volume of ore left in the stope due to insufficient breakage generation. If the volume extracted is less than planned extra costs for secondary blasting and/or diminution of the production may occur[9]. Furthermore, a secondary blasting process to extract the missing material can lead to an increase in the dilution rate, because secondary blasting can damage the walls and cause OB [2, 10].

It must be noted that secondary blasting can only be performed under specific conditions, because usually once the stope is fired and emptied, the chance for secondary blasting is low or null, leaving two last options: to extract the material while operating the adjacent stope or to leave the material there. These two issues are caused by geological conditions, blasting factors, or a combination of both. Their control is usually carried out by adjusting the blast pattern as geological conditions cannot be changed, the usual blast design conundrum is that an adjustment to prevent UB typically generates OB and vice versa[2].

2.2.3 Stope design

The main purpose in the design of stopes is to ensure high performance and proper stability during the production period. Common features considered in the design are:

1. The stopes are open and can be extracted without substantial wall collapse or caving.
2. The blasted rock moves by gravity alone to the stope drawpoint.
3. The blast method uses long blastholes for rock breakage, achieving good fragmentation.
4. The blastholes are located within planes called rings and can be drilled downwards or upwards.
5. The initial expansion slot is located on the side, centre, or bottom of each stope.
6. The method is non-entry, therefore personnel do not have access to the stope.

The first stage in the design is the rock mass characterisation, determining geotechnical and geological characteristics. That information enables the estimation of strength and deformation characteristics of jointed rock masses with the purpose of ensuring the stability and performance of the stope.

The rock mass characterisation starts with the orebody delineation and core logging, then a series of visual methods can be applied to define the quality of the stope boundaries in more detail. The idea is localise discontinuities within the rock mass to predict their incidence in the process of extraction and prevent geotechnical risks as stability problems, wedge formation and stress concentration. The next step is to determinate an optimal geometry ensuring an intrinsic stability. Because the success of the method relies on the stability of large stope walls and crowns, as well of the stability of any fill masses exposed, the determination of an appropriate geometry is critical.

The geometry depends on two factors: the RM strength (highly affected by discontinuities, influencing the rock resistance to any type of failure-inducing stress) and ore location as shown in the Figure 1. The final stope shape will be defined by the stability, according to the RM conditions and ore disposition.

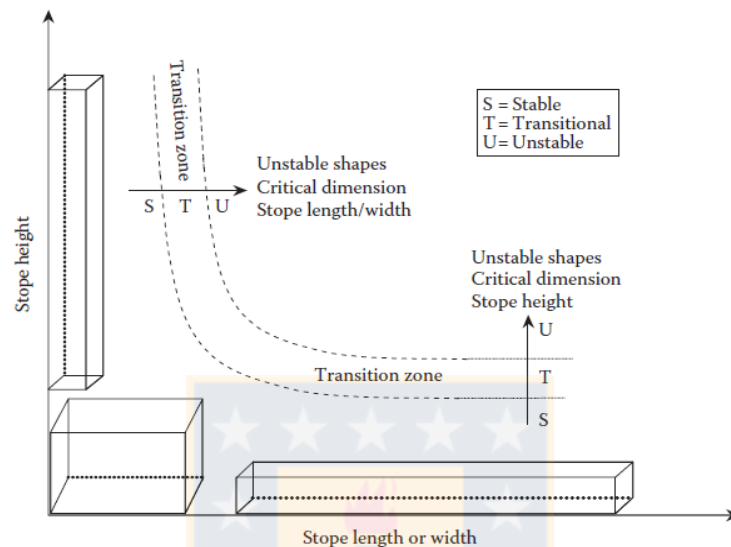


Figure 1. Stable shape of stopes, relation between height and width [6]

2.3 Stope stability

The stope stability can be analysed using different methods as for example: limit-equilibrium methods (LEM), finite-element methods (FEM) and empirical methods. Putting more attention in the last one, an empirical graphic method developed by Mathews [5] has been continually extended through a significantly increased database of mining cases [4]. The approach relies on relating a stability number “ N ” to the stope wall hydraulic radius known as shape factor “ S ”.

The N estimation utilises a modification of Barton’s Q value based on the Q - System, an empirical model originally developed for rock masses and ground classification with the aim of evaluate the need of support in tunnels and rock caverns depending on the structural conditions [11, 12]. The modified Q “ Q' ” is calculated from the results of structural mapping and its factor is defined as:

Equation 1. Modified Q

$$Q' = \frac{RQD}{J_n} \times \frac{J_r}{J_a}$$

Where:

- J_n is the joint set number
- J_r is the joint roughness parameter
- J_a is the joint alteration parameter
- RQD is the rock quality designation, indicator of how fractured is the rock mass. The range goes from 0% to 100%, where 100% represents an excellent quality of the rock mass and 0% represents crushed material.

An important point to mention about RQD is the bias risk involved in the determination of this parameter. RQD is defined as the ratio of the sum of lengths of core pieces longer than 10 cm to the total core or scanline run length[13]. Some of the issues of this technique are that the value of RQD can change according to the orientation and length of measurement as is shown in Figures 2, 3 and 4, losing representativeness and accuracy[14].

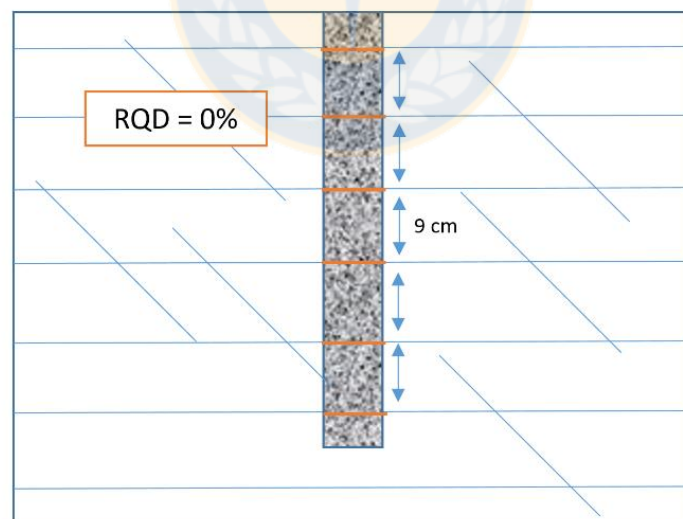


Figure 2. RQD orientation bias, core run perpendicular to structures

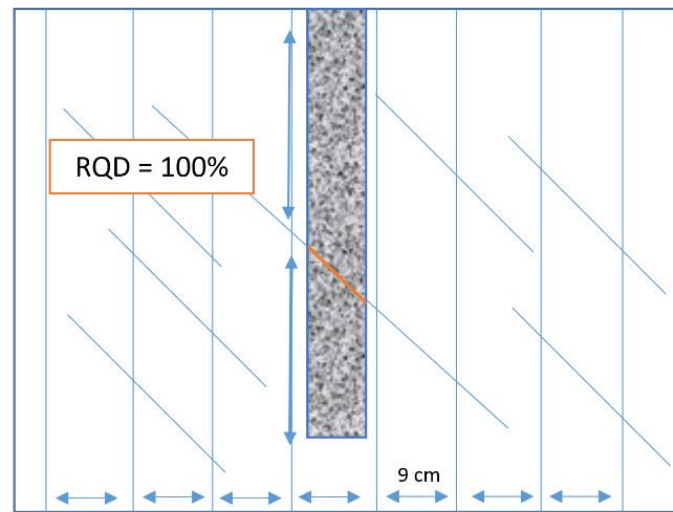


Figure 3. RQD orientation bias, core run parallel to structures

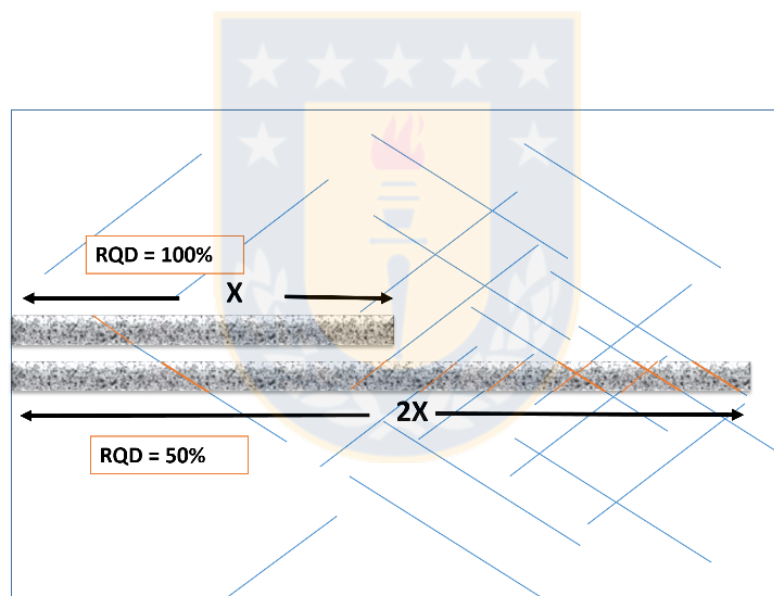


Figure 4. Length influence in RQD

When the RQD is used as input in Q it may be estimated utilising the volumetric joint count factor (J_v) defined as the number of joints in one cubic meter. Is an alternative to incorporate three-dimensional measurements in a directional technique (one – dimensional) as RQD and scanline, to improve the representativeness and avoid the bias [15]. Where the jointing occurs mainly as joint sets the joint count factor can be calculated as appears in Equation 2:

Equation 2. Estimation volumetric joint count factor

$$J_v = \frac{1}{S_1} + \frac{1}{S_2} + \frac{1}{S_3} + \dots + \frac{1}{S_n} \quad (2)$$

Where S_1, S_2, S_3 and S_n represent the average spacing for each one of the joints sets respectively. Randomly oriented joints can also be included as may influence the rock mass quality using a modification to Equation 2:

$$J_v = \frac{1}{S_1} + \frac{1}{S_2} + \frac{1}{S_3} + \dots + \frac{1}{S_n} + \frac{N_r}{5\sqrt{a}} \quad (2.1)$$

Where N_r is the number of random joints in an actual location with an area of am^2 . Finally the expression for the relationship between RQD and J_v [15] is defined by Equation 3:

Equation 3. Rock Quality Designation estimation using the volumetric factor

$$RQD = 110 - 2.5 \times J_v$$

The Q' parameter is required to determine the stability number N adjusting Q' according to discontinuities, stresses and wall orientation, finally the N factor is calculated as follows:

Equation 4. Stability Number

$$N = Q' \times A \times B \times C$$

Where A is a stress factor, B is a rock defect orientation factor and C is a design surface orientation factor

These three factors are determined by graphic analysis (Figure 45- 49). The hydraulic radius is obtained by wall geometric measurements, the S factor or HR is defined by:

Equation 5. Estimation of S factor or hydraulic radius

$$HR = S = \frac{H \times L}{2(H + L)}$$

HR is basically the area of surface under study divided by the perimeter of a rectangle of the same surface with H as the height and L the length.

Both factors, N and S are inputs in Mathew's Graph to determine the stable and unstable zones or caving zones directly [4].

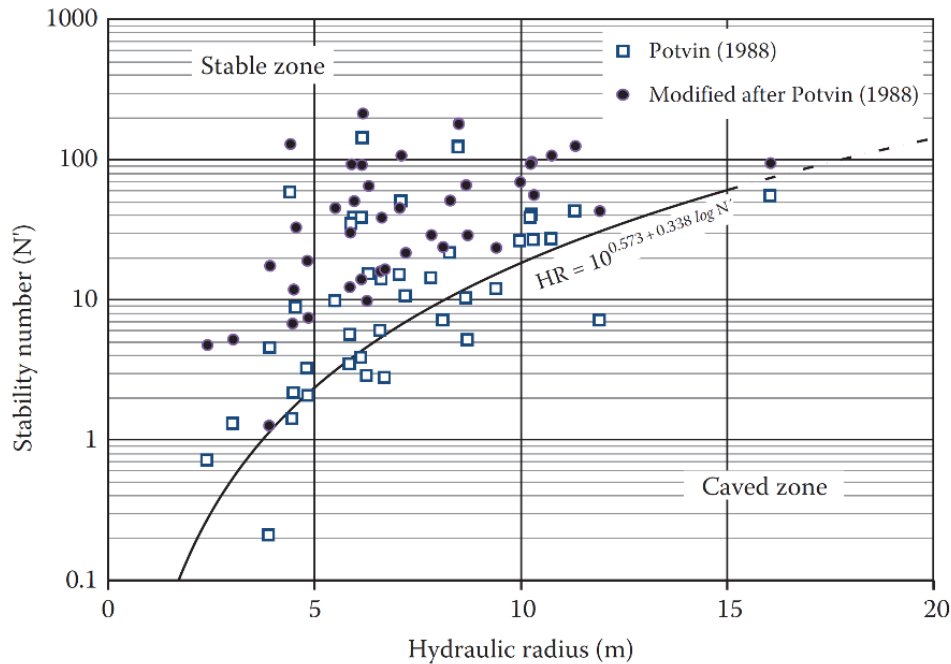


Figure 5. Extended Mathews stability graph [16]

2.4 Stopes Drill and Blast

2.4.1 Background

The Drill and Blast processes used in SLS are based on Longhole Drilling and Ring Blasting Pattern techniques incorporated in the design. The objective of the blast design is to achieve a desired fragmentation to ensure a good extraction of the material (fragments not too large to block the draw point but big enough to ensure an appropriated digging). The blast design defines the number, position and length of blastholes to achieve the desired size distribution of fragments, considering the orebody shape, rock mass conditions, groundwater, available equipment, stopes access and explosive type. The final aim of the blast design is to allow for the extraction material and start with the mineral processing stages.

Furthermore, there is an economic incentive to achieve the desired fragmentation distribution: minimising the damage and staying within certain vibration thresholds, minimising the OB and UB, by means of a minimal use of explosives, materials, and labour hours, whilst still achieving loading and handling productivity targets [6, 17].

2.4.2 Blast design and Geological structures

More than thirty years ago researches began to study the relationship between GS and blasting outcomes [18]. Ibarra & Franklin were one amongst the first to mention the existence of tentative evidence of that relationship noted that RM quality could be slightly more influential in causing OB, being jointing the major responsible, and that explosive energy might be slightly more influential in causing UB” [2].

One year later, Germain [10] explained that in good quality rock masses, with few discontinuities present, the strain energy from the blast generated OB, and in heavily fractured rock masses rock blast damage mechanism will be dominated by gas expansion along discontinuities. In that case, the strain energy is rapidly absorbed by shearing mechanisms along joints. This is evidence of the complex link between the GS and the performance of the stope, through their effect in the blasting outcomes.

The factors that influence OB and UB can be classified in two groups:

- Geological conditions with more emphasis in GS and their characteristics.
- Blasting, considering their design, execution and distribution of energy.

Nevertheless, because the RM features cannot be changed, any modifications to prevent OB and UB must be done in the blast design, without a real knowledge of how discontinuities influence blasting. Singh and Xavier [3] supports this and stated that the knowledge of rock mass feature implication in blasting can facilitate the judicious selection of explosive characteristics and blast design parameters to obtain optimum results.

The orientation of discontinuities relative to the stope walls and roofs one of the principal features of the GS that can have a significant effect in the generation of OB and UB as the presence of joints affects the attenuation of the blast-induced stress wave, depending on the incidence angle. For bench blasting it was determined that the attenuation is minimal when the angle of incidence is parallel or perpendicular to the face and increases to a maximum when the angle is between 15° and 45°, this leads to a similar suggestion to crack propagation in SLS stope perimeter (stope walls) [3, 19]. In summary, a good knowledge of the blasting behaviour in presence of discontinuities in combination with an informed blast design could be the solution to prevent dilution and ore loss problems.

2.4.2.1 Breakage mechanisms

Blasting is one of the most inexpensive methods of breakage in hard rock fragmentation [3] and bulk mining, thus a good understanding of the process is paramount.

The process of fragmentation is achieved by the combination of two processes: the activation of pre-existing micro and macro fractures within the rock mass and the creation of new structures while the material tends to dissipate potential energy through the extension of GS, heat and sound .All that from an energetic point of view [20].

Mechanical waves produced by blasting are the cause of GS activation, with an important characteristic: these waves need a physical medium to be transmitted. Considering that, a small portion of the blast wave is transmitted or dissipated through the air and the rest travels within the RM as a strain wave, once that wave reaches a free surface (an interface between the RM and the air), it is reflected and may cause spalling of surficial slabs [21]. The efficiency of the transmission depends on the rock impedance, which in turn has a direct dependence on RM conditions and presence of discontinuities. Discontinuities decrease the impedance by generation of open space that breaks the connectivity of the RM.

If a crack is modelled as a thin trace with a point of start and end, and there is a stress wave moving perpendicular to the crack, the stress is going to be concentrated in the ends of the crack. At some point, the concentration of energy is so high that the only way to liberate it is creating new surface: in macroscopic terms, this happens when the traction resistance (tensile strength) of the rock is overcome.

In hard rock blasting three zones can be identified around the blasthole area within the rock mass (Figure 6):

1. **Crushed zone:** Associated with a higher concentration of energy, the hydrodynamic zone is immediately next to the blasthole, showing an excessive disintegration created by the impact of the compression wave and gas expansion during the instants following the detonation.
2. **Radial Fractures:** Beyond the crushed zone starts an area where the creation of radial structures, as product of gases expansion and tensile failure in a direction perpendicular to the compression wave, is the key to the fragmentation.

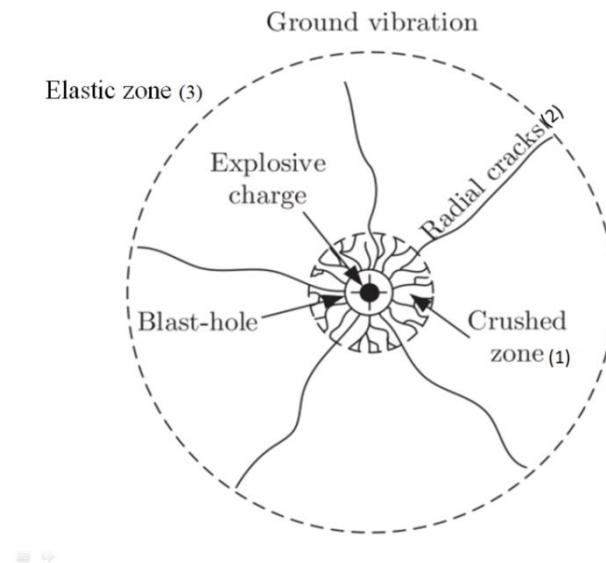


Figure 6. Crack formation around the blasthole [22]

3. Elastic zone: The compressive wave continues travelling beyond the zone of radial fracture until discontinuities in the RM limit the wave propagation. This also means that the pre-existing joints and fractures define the extent and shape of the blast damage zone. After the compressive wave hits a discontinuity or structure with the characteristics of a free face, the wave is reflected as a tension wave enabling the extension and propagation of the new structures formed previously and pre-existed, as the resistance of the RM to tension is always lower to compression [23].

2.4.3 Blast design

The blast pattern used in SLS has a particular design called “Ring Blasting” and employs long hole drilling to achieve the desired geometry. The ring is a collection of blastholes in a given plane forming what is often termed a blasthole fan [17].

Blastholes are generally drilled radially from a central point or pivot point, located inside a development drive. The pivot point is the initial reference for all the holes that shape the fan with variable angle and length of drilling for each hole according to the requirements.

The factors in considered part of the blast design are [17]:

1. Spacing: Because of the fan geometry, in ring blasting the spacing is defined by the toe spacing. The measure has different definitions, the definition use in this research

is the JKMRC approach, which define a True toe spacing (S) and an Effective toe spacing (T), being S the perpendicular distance between from the shortest to the longest hole [17] as depicted by Figure 7.

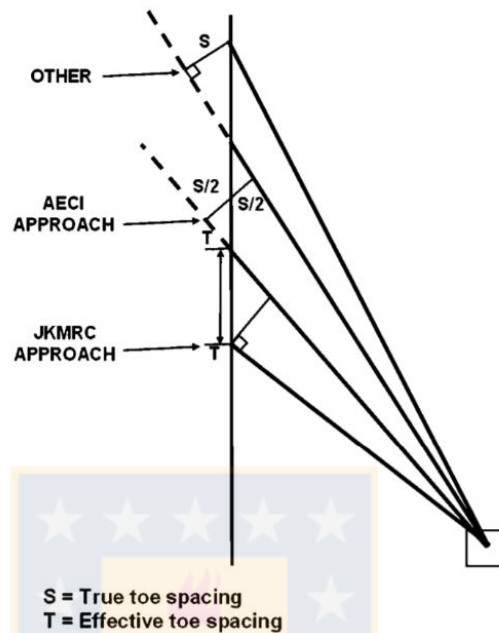


Figure 7. True toe spacing and effective toe spacing [17]

2. Burden: Is the distance between the ring plane and the next free face, typically equivalent to the distance between rings.
3. Offset: Distance between blasthole or toe and an excavation boundary.
4. Charge Length: The length of explosive charge in a blasthole, with a specific density.

The blastholes in the ring are typically drilled parallel to the wall to enable a good control of damage in boundaries and their diameter is defined following the same principle, bearing in mind that large-diameter holes tend to create a greater damage to the surrounding rock due to the increased explosive concentration. As a result, these factors must be simulated and analysed to calculate the resulting powder factor in different parts of the stope to avoid excessive concentrations of energy or possible damage to the walls, as well as problems in the fragmentation.

Even when this process is done carefully there are some problems that still cannot be controlled, for example: hole deviation is a recurrent problem in long hole drilling. Another issue can be the complex simulation and representation of the blasting energy distribution in the potential presence of geological structures that were not detected in the initial mapping.

The changes within the rock mass which can have an influence in the blast design are divided into two groups:

1. Natural alterations: Intrinsic characteristics of the rock mass such as changes of hardness, geological structures, weathering, time, others.
2. Post explosion: After blasting, the seismic wave can generate the propagation/activation of geological structures and this needs to be considered in subsequent blast designs to ensure the accuracy and safety. This can have a considerable effect in adjacent stopes, which is not usually considered in the design process.



3. General Review of Mapping Techniques in Underground Mines

3.1 Structural mapping background

Mapping and analysis of natural structures in the rock mass is essential for underground projects, especially those involving infrastructures required for civil use and mining where humans lives are involved [24], becoming the first and most important step to be undertaken in any type of rock engineering project to maintain safety and engineering standards.

In underground mining, engineers have the responsibility to detect hazardous zones whilst complying with the planned production, which is why fracture mapping acquires greater importance. This is especially true in SLS where the structural mapping is used in all extraction process stages [1, 25].

Geotechnical analysis provides the input for the entire design process of stopes and drives [6]. The features of geological structures and their characteristics within the rock mass are incorporated in 2D maps and more recently in 3D structures models, used in the prediction of the rock mass behaviour and the possible influence of structures in the construction and operation. Generally, the most important factors influencing the rock mass (Figure 8) behaviour according Villaescusa [6] are:

1. Intact rock: Solid material between the discontinuities. Failure modes may involve failure of intact rock bridges.
2. Rock Stress: The vertical stress caused by the weight of overlying strata and the horizontal stress caused by tectonic forces.
3. Number of sets of discontinuities: A discontinuity is a mechanical break (of geological origin) within the rock mass and because of geological process; discontinuities can be formed in sets containing parallel structures.
4. Orientation of discontinuities: This characteristic is measured using dip direction and dip angle, represents the geometry of the structure.
5. Frequency and spacing of discontinuities: The frequency is the number of discontinuities per unit distance in space within a given set. It is reciprocal of the spacing and can be measured globally for all discontinuity sets or by individual set.

6. Persistence and termination of discontinuities: Persistence is the observed trace length of a discontinuity within the rock mass. Termination of a discontinuity can be either in intact rock or against another discontinuity.
7. Block shape and size: The block size is a function of the number of sets, frequency, orientation, size and termination of the discontinuities, represents the in situ fragmentation of the rock mass.
8. Roughness of discontinuities: Inherent surface roughness and planarity, with respect to the naturally occurring mean plane defining a discontinuity. Both roughness and planarity contribute to shear strength.
9. Aperture: Perpendicular distance across adjacent surfaces of a discontinuity.
10. Wall strength: Compressive strength of adjacent surfaces of a discontinuity. Usually lower than the rock block strength.
11. Infill: Material between adjacent rock surfaces of a discontinuity.
12. Water seepage: Moisture or water within individual discontinuities or through intact rock.

Unfortunately, a detailed description of some of these factors can only be obtained on exposed surfaces through visual inspection, a complex job in SLS.

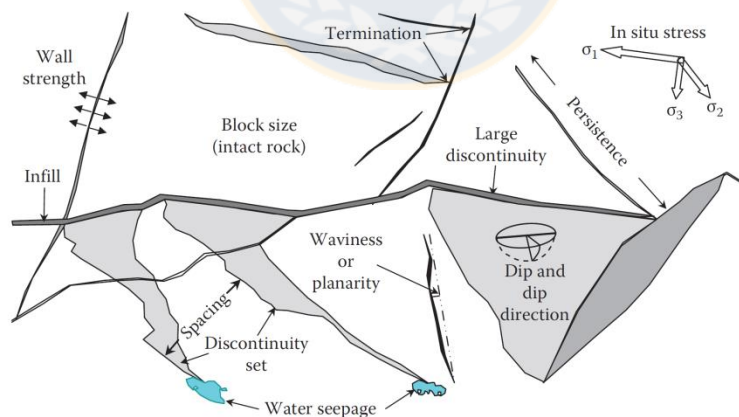


Figure 8. Factors influencing the RM behaviour [2]

3.2 Short overview of mapping techniques in underground mines

A series of instruments and techniques have been developed over the years to obtain representative information while mapping in underground conditions, with limited exposed

surfaces to achieve the task [26]. They include techniques ranging from traditional visual method to sophisticated remote technologies, among them LiDAR(Light Detection and Ranging)[27, 28].

Currently the determination of the orientation of discontinuities that compose the fracture map is typically measured from the rock face using compasses and inclinometers, while the other fracture characteristics are obtained through visual inspection. The measurements are usually collected using the scanline method or other traditional methods that involve window and borehole mapping [29].The main shortcoming of these techniques is that too many people are involved in the data acquisition stage, making it a time-consuming process and generating inaccurate data because of the individual interpretation of visual inspection. Another critical issue linked to the presence of workers in the stope entrances, tunnels and faces is the limited safe access to the unsupported zones [25, 27]. In the case of stopes it is practically impossible to perform fracture mapping of a complete wall from the inside of the structure.

3.3 Traditional mapping techniques in underground mines

3.3.1 Core Logging

Geotechnical information about the RM is initially obtained during the exploration stage. The standard method used for orebody delineation involves diamond drilling in combination with core logging, which also helps collect information about the general geotechnical conditions. This process includes data collection from widely spaced surface drilling programs and any subsequent underground drilling for detailed stope characterisation purposes.

An advantage of this method is the long depth reach, providing critical information from the centre of the mineralisation zone used for stope design. In this process faults, dikes, and shear zones on each section can be identified. The mechanical behaviour of underground constructions and geological dilution can be estimated from the design stage through the determination of geological domains, joint condition and strength of the RM.

The method has some disadvantages as well, as the logging may be performed by a large number of geologists, all of them with different geological and geotechnical interpretations opening the way to bias problems. Another issue is the mechanical disturbance of the core during the drilling, core loss in heavily fractured rock, wash out of infill material

during the drilling process and drill deviation, as well as the orientation bias discussed in section 2.3 in the context of the RQD bias description. All together can achieve an important loss of representativeness [6].

To improve the accuracy and representativeness it is necessary to complement core logging with an underground drilling campaign, better known as underground delineation. The level of detail required depends on the stage of the project (mine prefeasibility, feasibility, etc.) sometimes a secondary campaign is required to increase the accuracy as is shown in Figure 9 and Figure 10.

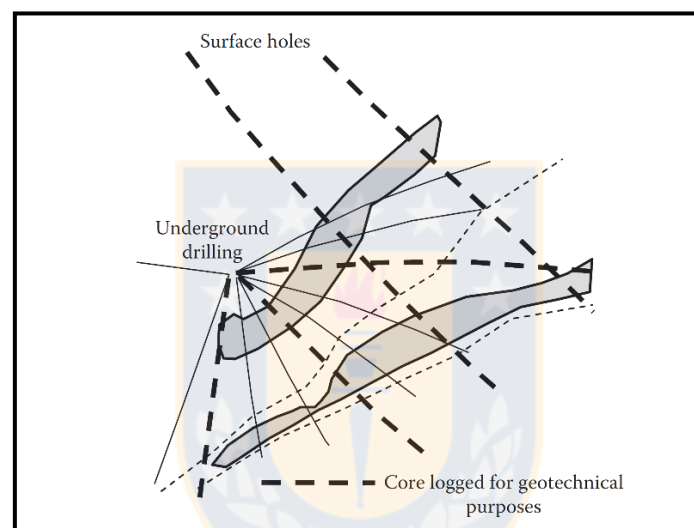


Figure 9. Exploration and Underground drilling campaigns [6]

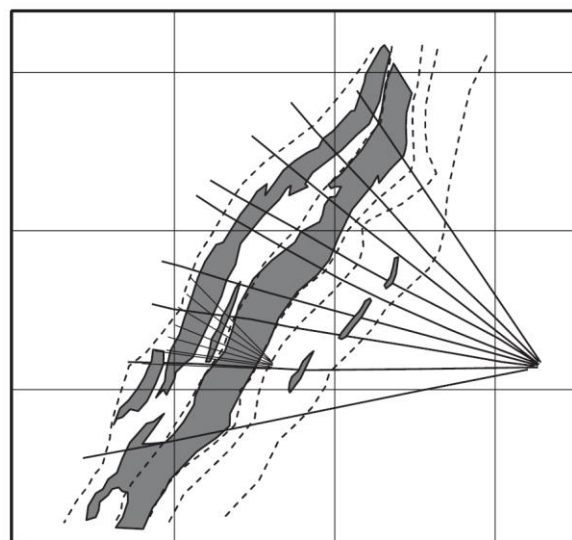


Figure 10. Secondary drilling campaign for characterisation and ore distribution estimation [6]

3.3.2 Scanline Sampling

Scanline is a standard method to measure the spacing and persistency of fractures in exposed rock faces. It has the advantage of covering a large area of rock allowing for direct measurements of discontinuity orientation, size and other large scale geometrical features [30]. The technique starts by choosing a clean, approximately planar rock surface sampling area with an important visualisation of fractures to base the calculations on.

The intersection between the discontinuities and the rock face will produce linear traces establishing a two- dimensional sample of the discontinuity network. A virtual line between 50 and 100m long (known as the scanline) is set above the rock outcrop and the location, orientation and condition of the rock face are recorded [29] . The orientation and dip of the visible geological structures is calculated using compass and inclinometer; all the information is recorded and photographed from different perspectives in order to obtain a scale of the features and minimise the impact of the image distortion in the measurements (Figure 11).

The photographs (Figure 12) are analysed and the trace of every discontinuity that intersects the scanline is mapped. A series of scanlines with different length can be measured based on the major fluctuations of rock mass properties such as lithological changes, structural changes and changes in weathering rate, in order to obtain the most representative data[31].

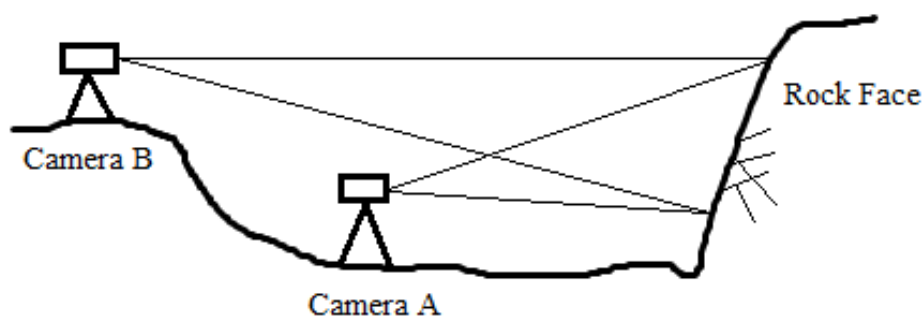


Figure 11. Example of camera positions for distortion correction



Figure 12. Example of scanline photograph for analysis [6]

Two key limitations that reduce the accuracy of this technique are the difficulty to decide whether a given fracture is a geological natural discontinuity or if it was introduced during blasting, and the impossibility of measuring fractures that run in parallel to the scanline. Nevertheless, the main issue for the use of this method in SLS is the field data acquisition process, impossible to perform in hazardous areas like unsupported zones and stopes [26].

3.3.3 Window or Cell Sampling

The background and measurement technique of cell sampling is essentially the same as for scanline, but the sampling domain is two-dimensional. The difference is that instead of defining a scanline and measuring all discontinuities that intersect that line, an area of the rock face is defined and all structures with a portion of their trace inside the area are measured [30]. Thus the technique sets up a virtual rectangle in the rock face (as big as possible in order to avoid the bias effect) and then classifies the joints into three groups (Figure 13):

1. Contained: Discontinuities that intersect the window and have both ends visible.
2. Dissect: Discontinuities that have only one end visible and the other end is obscured, extending beyond the limits of the window.
3. Neither: Both ends are obscured, extending beyond the limits of the window.

To estimate the main trace length, it is necessary to count the number of discontinuities in each group and then apply a method of approximation, usually for this purpose colour photographs are required to have a good visualisation.

Shortcomings of this method include the lack of information about the orientation, frequency or qualitative characteristics of the discontinuities or geological surfaces and the laborious areal sampling; since the window contain a large number of small structures, it can be difficult to keep track of which discontinuities have been measured. As scanline, window sampling has the limitation of the data collection technique, limited by the safety standards. Furthermore, window sampling needs a larger study area which is even more infeasible in stopes and unsupported sections.

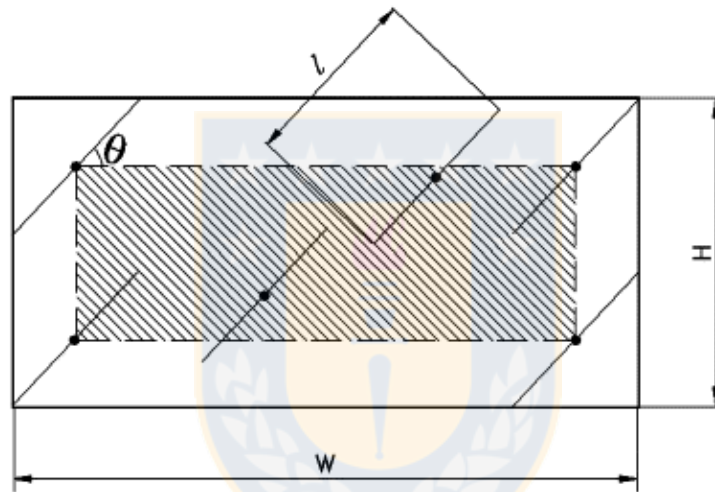


Figure 13. Window sampling example with the three types of classification

3.4 Remote sensing techniques

3.4.1 Photogrammetry

Photogrammetry is the process of constructing maps or 3D models of real world objects or scenes of underground tunnels and caves based on distance measurements from photographs. Currently this remote sensing method is used in mining for stability studies and structural mapping, specifically development of Discrete Fracture Network (DFN) models across all the sections with exposure of rock faces. The models include the length of the traces, persistency, joint orientation and spacing for underground mines characterisation [26, 32, 33].

The outset of this technology involves careful positioning of the two stereo cameras in front of the wall selected to be studied. The accuracy varies as function of base-to-distance ratio, where “base” is the distance between the cameras and “distance” is the distance from the cameras to the subject(see Figure 14).Low base-to-distance improves the accuracy of the measurements [33]. The objective of the process is to overlap two images in order to correct distortion and create a 3D model with two perspectives of a same surface [32]. Data collection takes a few minutes and can be performed with minimal operational disruption, however this will be depend on how crowded the site under study is [32].

Photogrammetry has some clear advantages over traditional field sampling techniques: it is possible to perform it at a safe distance from hazardous conditions and can generate a permanent geometric record for future analysis. Current mine drive developments are completed within a few hours of blasting with the application of shotcrete or other reinforcement systems which disturb the surface, thus there is a short interval of time available for face mapping. Photogrammetry can be performed in a short time frame and the mapping completed and preserved without delaying the reinforcement stage [26].

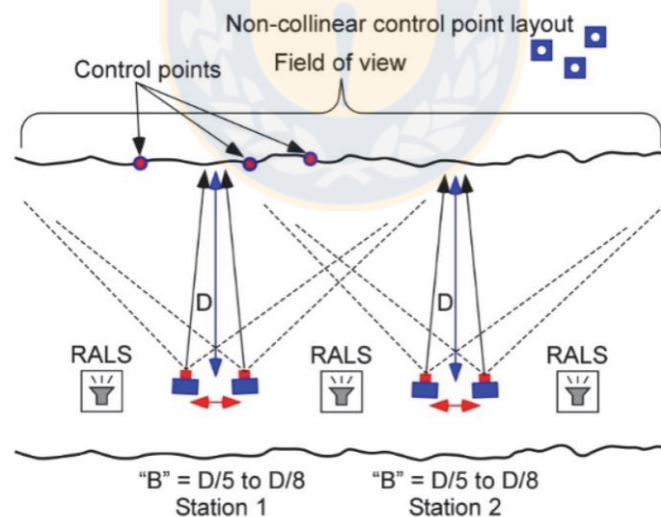


Figure 14. Photogrammetry camera position to correct distortion and create a 3D model [32]

Photogrammetry also has advantages over other remote sensing techniques, specifically over Laser scanning:

1. The data can be collected with relatively inexpensive devices that require minimal operator training and can be completed in approximately 20 minutes [32].

2. The photographs themselves contain more information useful for analysis, such as water intrusions, evidence of damage and characteristics determined through the image colour, features that previously had to be obtained in the field.

Some of the limitations of photogrammetry are:

1. Difficult work in murky walls, poorly illuminated areas or dusty environment. Is highly susceptible to occlusion [34].
2. Inability to provide immediate or continuous data due to the significant time required to process and analyse the information [26, 32, 35].

3.4.2 LiDAR sampling technique

LiDAR is a imaging technique based on measuring the reflection of a focused light beam, usually a laser [36]. This instrument fires a rapid pulse of light at the surface and a sensor measures the time the reflected pulse takes to return to the origin. On this process the laser can generate tens to hundreds of thousands of referenced 3D locations in a short interval of time (more than 220.000 measurements per second) building a high resolution virtual 3-dimensional point cloud, which after processing supplies an accurate image of the surface measured for a given location (obtaining the coordinates X, Y and Z). LiDAR enables the measurement of surfaces with dimensions up to $6.000m^2$ [29, 37].

LiDAR has been applied in mining operations, specifically in open pit mines, where the visualisation and manipulation of point clouds allows for performance assessments, RM characterisation and identification of hazards [25, 38, 39]. For underground mining the applications have been limited to geotechnical data collection in tunnels, with the potential to add efficiency and accuracy to this task [29].The image generated with the point cloud is clear and accessible, enabling the recognition of discontinuities and their orientation at the boundaries [29] and even the measurement of spacing, roughness and persistence of discontinuities [39-41], key factors for assessing underground stability and blasting results among others analyses [3, 42].

3.4.2.1 Advantages of LiDAR

LiDAR has many advantages over the traditional manual and remote sensing technologies:

1. Is effective in dusty, damp and/or dark conditions. LiDAR's ability to work without external light is a key advantage over other remote sensing technologies, such as photogrammetry [27]. This characteristic is particularly important in the case study of this research as it is nearly impossible to fully illuminate stopes because of their dimension and restricted access.
2. Improves workers safety, allowing the data collection from a prudent distance to the rock surface, decreasing the risks [43].
3. The identification of the discontinuities and their characteristics can be done interactively or automatically. The interactive extraction consumes more time but allows the engineers/geologists expertise to be incorporated, enabling for example the differentiation between natural fractures and fractures produced by blasting based on an expert analysis [37, 40, 44]. The automatic recognition, in turn, facilitates the generation of large amounts of accurate models [25, 45, 46].
4. The method is less time consuming than hand mapping and photogrammetry because the image processing is instant. In comparison, photogrammetry has a processing time of up to 30 minutes and hand mapping information can take much longer to be processed [35]. The fast processing time of LiDAR leaves time for the experts to analyse more carefully the joint conditions and determine alterations, water inflow and discontinuity filling. Furthermore, as LiDAR produces the point cloud automatically the analysis can start immediately, without the need of previous preparation.
5. LiDAR increases the quantity and accuracy of measurements. This means that fluctuations in the discontinuity surface are better represented. Moreover, it is possible to create extensive rock mass models, improving the chance of identifying key discontinuities and key failure modes [27, 43]. The detection and representation of each discontinuity in 3D enables the evaluation of joint spacing and structures interaction.
6. LiDAR generates a permanent documentation of the rock condition and analysis after the rock face is covered by reinforcement or others structures [27].

These highlights show the key features of a method that has never been explored in the context of SLS, with the potential of generating advantages in the long-term and throughout all the value chain [34].

3.4.2.2 Disadvantages of LiDAR

The key shortcomings of the LiDAR technique to be considered are:

1. The ability of the scanner to identify and measure surfaces through the return wave depends on the reflectivity of the material, which can hinder LiDAR measurements. A solution is employing a LiDAR system with variable wavelength (colour) and/or intensity to adjust for different material surface properties [43].
2. There is a direct effect in the intensity of the scanner that affects the point cloud quality and accuracy in terms of low point density, presence of noise and lack of representativeness (points seem to be floating disjointed from a surface). This is caused by an inadequate distance between the laser and the measured surface, as is shown in Figure 15. For large distances the pulse of light has to travel through dust and humidity, losing intensity and the distance between points increases product of the angular projection. Closer distances are expected to build point clouds of high density and representativeness [47].

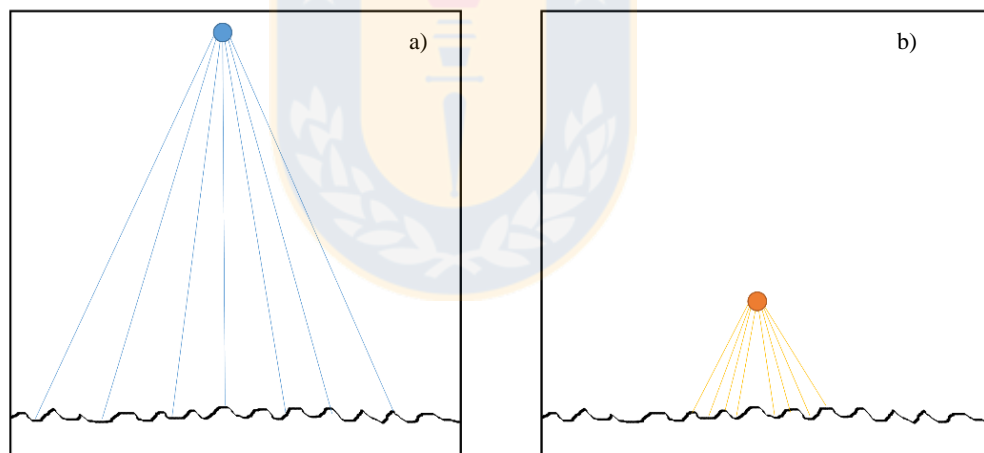


Figure 15. Distance measurement effect; a) Higher distance increase de angular distance between light pulses; and b) Lower distance provides more detail

3. The angle of incidence is an important factor for a good representation of the surface. Frequently, an increase in the angle of incidence decreases the density of points in the cloud because a decreased probability of return (Figure 16). This factor can be controlled and adjusted changing the position of the laser [29].

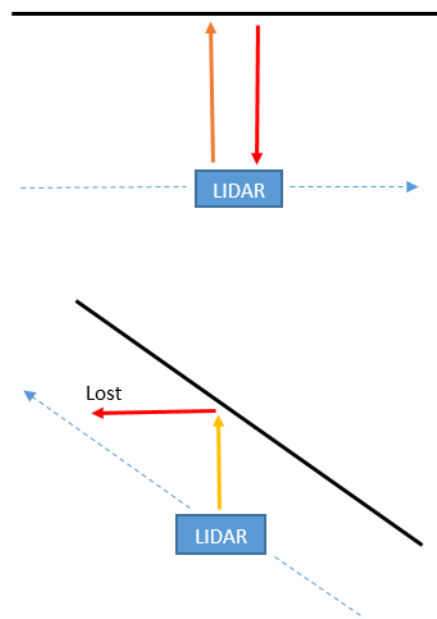


Figure 16. Problem of angle incidence with LiDAR

4. The cost of the instrument higher than other technologies such as photogrammetry or hand mapping [27, 43].

3.5 Hovermap: A tool for mapping in unexpected places

As previously mentioned, a recurrent issue across the literature regarding mapping is the impossibility to perform this activity under risky conditions as areas of imminent collapse, lacking fortification or areas simply impossible to reach [32, 43].

In answer to this concern a new technology was developed: a tool that combines remote sensing technologies and unmanned aerial vehicles (UAVs). Hovermap (HM) aims to generate maps in unexpected places in a safe way, without disturbing work areas or disrupting the mine production cycle [32], with the ability of provide instant information.

3.5.1 Short Overview of remote sensing in stopes underground mines

Remote sensing in underground excavations allows for the capture of information, without the need of be near unsafe zones, providing results within a few minutes. It also generates a permanent record of geometry and other characteristics for posterior analysis [43] in order to predict wedges, instability, future design requirements and other factors.

The first attempts at this approach applied photogrammetry and LiDAR in caves and tunnels, with the installation of bases (tripods) in sequence to record the information, in different positions and angles to avoid shadow areas during the data collection [26, 27, 48].

Because measurements must be performed on clean rock mass faces, without material obstructing the surface, the main risk arises from the lack of fortification (as fortification would obstruct the sensing). Thus the problem of accessibility remains, even if the process of base installation only takes a few minutes, it is still a potential risk for people involved in this task.

3.5.2 Cavity Monitoring Surveys

If mapping tunnels and caves is a complex task, mapping of stopes can be a real engineering challenge. Several case studies of stopes monitoring have employed 3D Cavity Monitoring Surveys (CMS) [49-51]. This system is composed by a single laser, which scans the surfaces. The scanner head is mounted on a boom that is pushed into the cave [52], allowing for almost complete rotation for mapping of all the walls, as shown in Figure 17, where the access to stopes is lateral or from the bottom.

In the context of SLS, this kind of scans from stopes provide information about the deviations of the final shape from the designed stope as: dilution, backfill volume, depth of main failures. It also enables the identification of structural control by large faults at the stopes boundaries [7, 53].

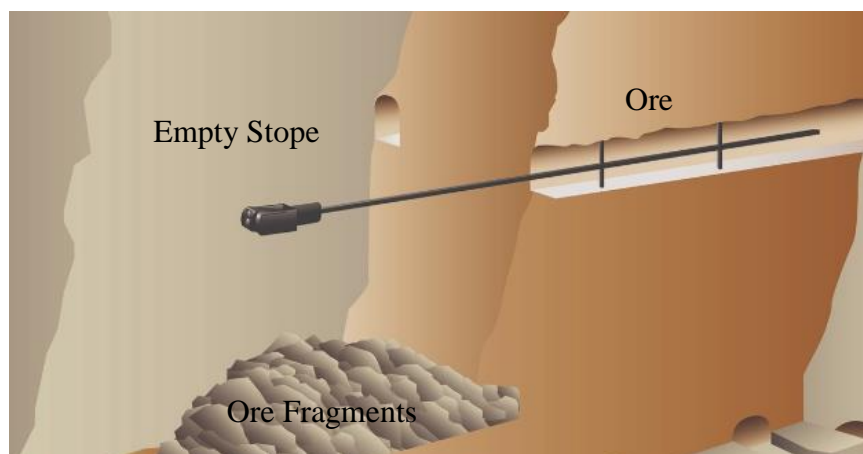


Figure 17. Stope access method, lateral access [49]

CMS represents a good alternative to access difficult places but needs special conditions to obtain an optimum performance. In particular, once the system is into the cavity it has to be held stationary at a point where the possibility of shadows is minimised. In many cases this produces only a partial map of the stope because of shadowing and can also be a laborious job in stopes with complex geometry [52].

Other disadvantages must be considered, for example:

1. The measuring tool is heavy and requires more than one person to perform the survey, normally the expert and two surveyors.
2. The scanning process can take more than an hour.
3. Point cloud density ($x \text{ points}/m^2$) is low and varies with the distance from the scanner.

A new approach to overcome the drawbacks mentioned above was successfully developed. It allows for more accurate, faster and cost-effective monitoring of mine cavities. The method is composed of a laser system which rotates in 360° (VM-SCAN 3D), light enough to be mounted on a drone and capable of performing stationary and mobile scans [52]. The results are ideal in terms of resolution and quality to estimate volumes (Figure 18) but still require improvements in resolution and autonomy to identify geological structures and navigate inside stopes.

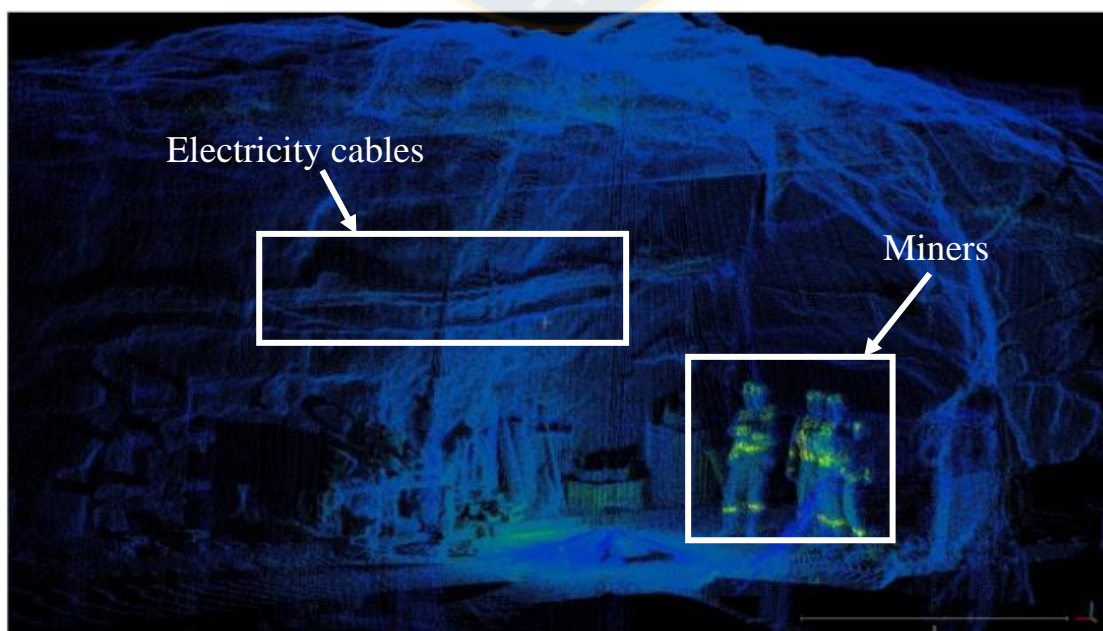


Figure 18. Point cloud of a mine drift captured by V-SCAN3D [52]

Figure 19 shows the difference between a point cloud obtained with CMS (a) and V-SCAN3D of a stope entrance from the base, is possible to see a portion of the tunnel and the bottom of the cavity. Both present similar characteristics in terms of shape representation and for volume measurements, but the mesh generated with V-SCAN3D is more detailed and dense, for two reasons: in the new approach the laser rotates in 360°, and there is complete access to the stope which reduces obstruction and decreases the angular deviation.

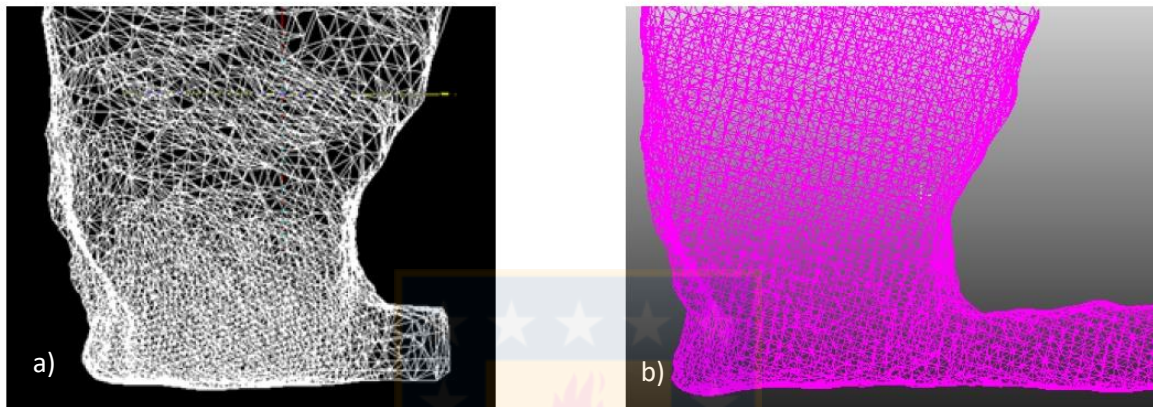


Figure 19. Wire frame scan performed by (a) Traditional CMS; and, (b) By V-SAN3D [52]

3.5.3 Hovermap

HM was developed by CSIRO'S (Commonwealth Scientific and Industrial Research Organisation) Data61 business unit and CSIRO ON accelerator as a new support alternative on 3D mapping tasks. Basically, is a self-contained LiDAR mapping mounted on top of a drone to map 3D spaces and objects in 360°, with special capabilities that makes this approach a unique technology through the combination of three main tools (Figure 20).



Figure 20. Hovermap approach based on the combination of three main technologies

LiDAR both performs the mapping and gives autonomy to the system using a Simultaneous Localisation and Mapping (SLAM) algorithm. SLAM is a solution to generate 3D point clouds and navigate without necessity of Global Positioning System (GPS), not available underground.

The working principle is: after a first input localisation the SLAM algorithm instantly estimates how the drone is moving relative to the localisation, using the start point as reference, fulfilling the function of a GPS and allowing the drone to navigate avoiding obstructions. The LiDAR data is also stored on-board and retrieved after the flight. The SLAM algorithm is used to generate the 3D point cloud with this data. The full autonomy function is still under development; currently it is still necessary a first guided flight of recognition. The key benefit is that drones (Figure 21) replace humans in the task of collecting field data, avoiding risk and reaching places previously inaccessible.



Figure 21. Hovermap, LiDAR tool mounted at the bottom of the drone

In the context of the mining industry, LiDAR is classified as one of the most expensive sensors when compared with other remote sensing techniques. The combination of LiDAR with UAVs could result in a decrease in the net final cost, since it is not necessary to stop the production to carry out the mapping. It might also involve savings in data collection through improved safety, because there is no human personnel in hazard zones involved in the collection. The new sources of information with high data density and accuracy could help optimise and improve processes, among other benefits.

3.5.4 Current applications of UAVs and HM

UAVs are a well-tested technology in multiple fields of research, and thus more common than the new HM technique. They have been widely employed in monitoring inaccessible areas such a volcanic areas, tailing dumps, management and supervision of construction sites and also as a passive method for remote sensing of submerged aquatic vegetation, monitoring of soil erosion and tunnel monitoring [14, 54].

HM is a fairly recent mining practice used to survey and monitor structures in open pit and underground mines (tunnelling). For the latter, the advantages that HM provides fit perfectly with the needs of that environment, opening new research opportunities and industrial benefit such had the possibility of get a complete 3D map inside a stope, with sufficient accuracy for effective recognition of GS.

This tool represents important progress but its application has not been proved yet. This is the core of this thesis, to test the ability of this tool to provide useful information to understand, asses and predict the rock mass behaviour.



4. Visualisation and Recognition Software

4.1 Background

The use of remote sensing tools such as LiDAR has become an essential tool for fault displacement and slope analysis over the last decade [37], acquiring dense 3D point clouds constituted a big challenge. This technology has been dynamically developed and improved and currently it is possible to envision important applications in underground mines. After revolutionising the acquisition of rock slope parameters in open pit, there was a surge in research of applications in the acquisition of exposed rock masses in underground environments for tunnelling projects, caves and, more recently, stopes. All these research tends to be focused on one specific geometrical property that retains users attention on 3D environments: Fractures Planes [55].

The new technology requires tools to support the big amount of information obtained with the ability to provide useful displays of the data while maintaining the accuracy.

4.2 CloudCompare

Cloudcompare (CC) is an open source 3D visualisation and computation software, created to analyse and estimate the differences between point clouds surface representations, widely employed across technical disciplines such as energy production, engineering, geoscience, etc.

As previously mentioned, the main geometrical property in this study are planes, which can be seen as a simple 2D geometric figure or as one of the most meaningful elementary objects for many applications in their 3D visualisation and interpretation [55]. For geotechnical applications, the representation of planes is key.

CC enables the visualisation and analysis of these planes with high accuracy. The performance of these features rely on data quality (shadow, time of exposure) and density of points (smoothness in the surface may difficult the recognition of structures with low density).

4.3 Discontinuity Set Extractor

The automatic recognition of planes and analysis is possible through software working on point clouds of high density. Computational programs such as Discontinuity Set

Extractor Software (DSE) and FACETS (a CC plugin for automatic extraction of planar facets from a point cloud) have been developed to perform this task and simplify the geologists job. These software have been trialled in open pit conditions making a comparison between the compass measurements or results obtained manually versus automatic recognition showing good results with a difference under 5° through main planes [41, 55].

DSE has been employed more frequently than other software because it is an open source software. Developed by Riquelme (2014) to address the key role played by discontinuities in the global and local stability of slopes, DSE was designed specifically for this aim: rock mass characterisation of slopes using point cloud [37].

The software automatically measures the dip and dip direction of planes, additionally it performs an analysis of joint sets calculating their spacing, persistency and roughness [37, 40, 56]. Only one study using DSE has been carried out in underground environments, in specific on a cavern face [51], showing satisfactory results but highlighting some restrictions:

1. Rock bridges or discontinuities hidden within the rock mass (e.g. Stratification planes) cannot be scanned because the features of interest are not expressed as a measurable surface (plane).
2. With the point cloud visualisation traces of discontinuities can be identified, but as they usually do not show a representative surface to create a sizeable neighbourhood of coplanar vectors, or they are hidden behind a shadow, the software doesn't measure them. The following sections will show that this shortcoming leads to the lost of important information.

Another important conclusion to this review of the software tools available is the need of considerable sensing expertise and geological knowledge in assessing the quality of the computational analysis. There are situations where compass/clinometer and visual analysis cannot be replaced, virtual outcrop geology is very advantageous tool for many applications (places difficult or impossible to reach as stopes) but does not replace fieldwork [55, 56].

4.4 Sirovision

Continuing the topic of discontinuities recognition and assessment, Sirovision was created as a 3D digital geological mapping acquisition and analysis tool, produced on a collaboration project amongst the Australian CSIRO, Datamine Software Ltd and AngloGold Ashanti Ltd (AGA).

In its initial stages Sirovision was designed only for geotechnical applications on open pit tasks with results that allows a DFN construction using Siromodel. The respective stability analysis [34] brings the possibility of working remotely using a 3D model created with photogrammetry without the hazards and time constraints associated with physical mapping in a underground mines. The system is continuously being improved to make it suitable as a total structural mapping solution [57, 58].

As part of the same project CSIRO developed a portable camera rig for underground use and created a 3D model with photogrammetry. The tool is a single unit which consists on a built-in, rechargeable power supply, an illumination system and a laser guidance system. Nevertheless, that format was deemed impractical for daily routine tasks [58]. The size and weight of the camera rig has a large impact on transportation within the underground mining [58], this derived in effective changes in the stereo camera to make it portable and lighter. However, the problems behind photogrammetry such as occlusion and time-consuming models creation persisted.

A new version of Sirovision is under development to address these issues with the utilisation of point clouds, the same data format obtained with HM. This Sirovision beta tester was provided to be used for the first time to test the efficiency of this software in the discontinuities analysis in combination with HM, bringing a new system to evaluate underground performance. It is expected to deliver:

- A complete and accurate recognition of the structures: faults, beds and joints.
- Measures of the properties of structures: size, orientation, shape.
- A stability analysis assessing the presence and stability of wedges or blocks that may fall.

5. Research Methodology

5.1 Research context

One of the main purposes of this work is to show evidence of the different applications and the data that can be obtained with HM. Two cases of study will be presented, each of them with special conditions enabling achieve a series of outcomes.

The first case study focused on a comparison between CMS and HM for a structural analysis. The second case of study will be focused on the stability analysis and the capacity of HM point clouds to show detailed surfaces and the effect of the density in the resolution.

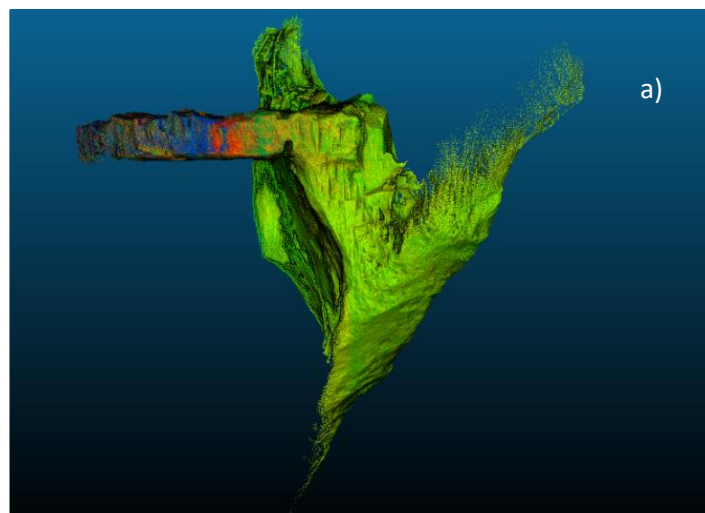
5.2 Presentation case studies

The data analysis process is different for each case study depending on the quality of scan and information available. It is worth mentioning that these are the only two scans currently available considering that HM is a new technology.

5.2.1 Case Study 1

The first case study is the slope “A” with dimensions 30m (length) x 12 m (width) x 30m (height). It is a SLS extraction slope (Figure 22) situated in the province of Ontario, Canada. Due to confidentiality agreements no further information can be disclosed.

The main characteristic of this slope is the clear visualisation of GS with deficiencies in the Hanging Wall (HW) (Figure 25) and Roof (Figure 22b)) becoming a good candidate to perform the Beta test version of Sirovision, utilising the software for the first time in geotechnical assessment of stopes.



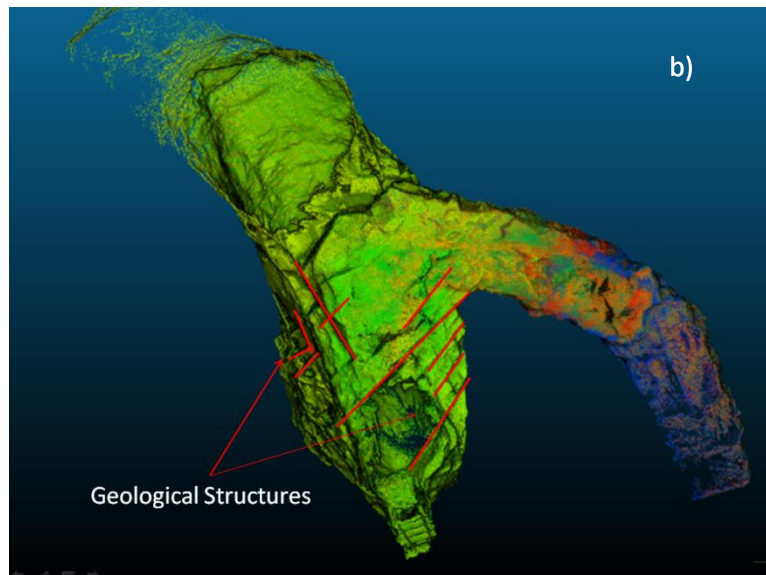


Figure 22. Stope A point cloud visualisation: a) Isometric view; b) Roof.

5.2.2 Case Study 2

The second case study, stope “B” (Figure 23) is part of a SLS extraction located in the north of Queensland, Australia. Located at a depth of 320m (base), with dimensions of 20m (length) x 23 m (width) x 68 m (height), composed only of one type of rock and mineralisation, presenting an RQD average of 82 and surrounded by three filled stopes in the north, south and west walls, which show good stability and performance (Figure 22 a)).

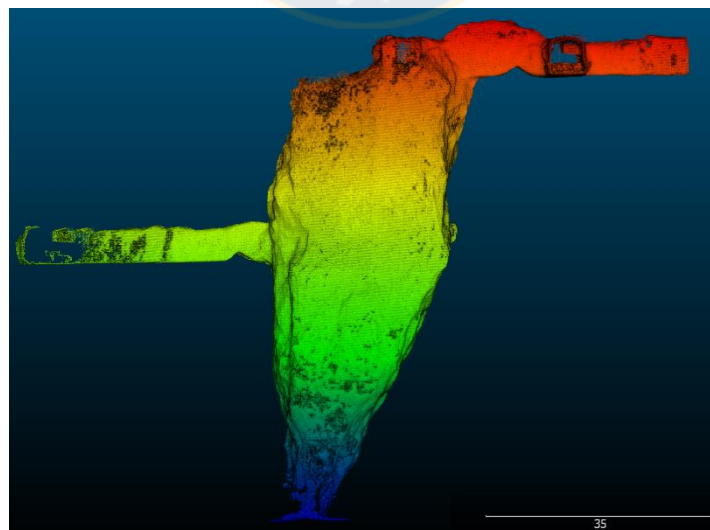


Figure 23. Stope B point cloud visualisation, coloured by depth where red indicates the higher zone and blue the deeper

There is only one main geological structure; a lizard fault formed by fragments or slices of continental and oceanic components that have been obducted over younger rocks and commons in zones with mineral enrichment, this fault cross the stope from the roof to the foot wall (FW) (Figure 54, Appendix B) and other few small structures determined by core logging located at the bottom of the stope near the HW. Is exactly in this area were a zone of UB was reported, from an 8.2% of total UB in the stope.

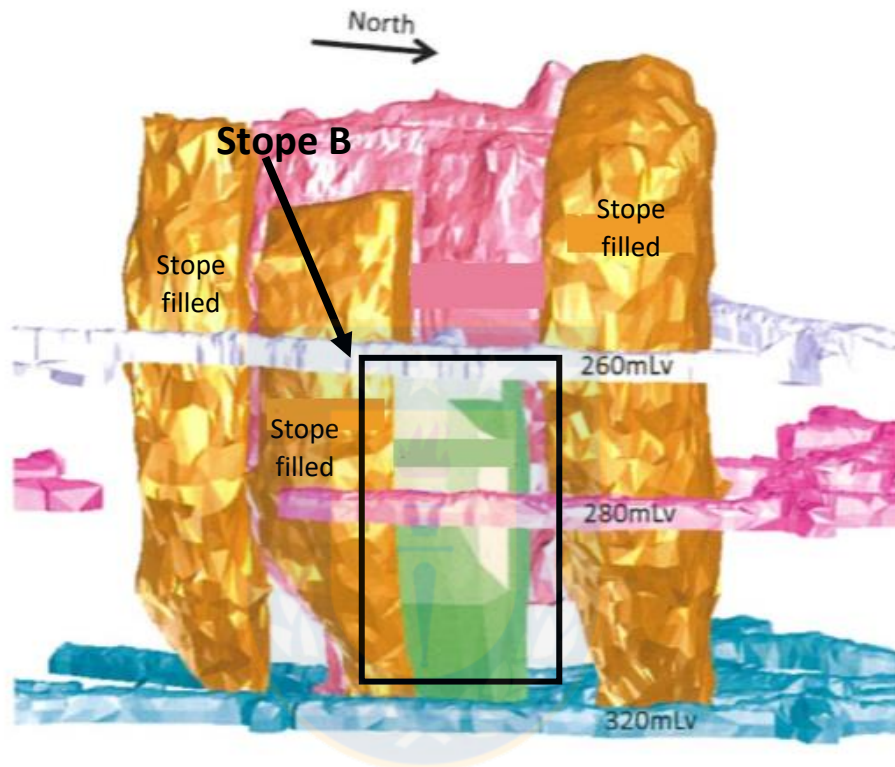


Figure 24. Stope B location and adjacent stopes

The main purpose for this case study is to evidence the potential of HM and its advantages over other mapping techniques, as well as the different uses for the HM data. The applications investigated in this case are:

1. Geotechnical analysis, with the estimation of wall stability with Mathew's graph. The results obtained will be compared with the information provided by the mine.
2. Blast performance assessment; in specific the possible link between the UB zone and the structures recognised.
3. Comparison of the results with obtained with CMS, measuring the difference in volume and point cloud quality (through point density comparison)

5.3 Structural analysis

Considering the simple recognition of GS in the point clouds, with a clear visualisation of structures and their planes. Sirovision is implemented to determine the main characteristics of the GS such as: Dip, Dip/Direction and persistency. All this to determine and classify the GS according their Dip/Direction into groups called families.

Finally, Sirovision efficiency is compared against an open source and automatic recognition software, DSE in the First Case Study.

5.4 Blasting energy distribution

The first task in the energy distribution is to determine a problematic area to analyse and a section with good performance to compare against. The conflictive areas are usually those with OB and UB, because they represent a stability and economic issue.

After the selection of the areas of study a 4D energy distribution analysis is implemented using a software for blasting simulation and information management in mines related operations, JKSimblast and its plugin JKBMS. This criterion enables the incorporation of timing in the blast simulation producing more realistic results.

The principal objective of these simulations is to determine with proper evidence the origin of UB and OB, if the origin of these issues was an inefficient blast design or the GS blocking the energy transmission.

5.5 CMS versus Hovermap

To demonstrate the advantages and the quality of the information that HM can provide over other conventional technologies such as CMS, some key factors were measured and compared. Key factors measured were the point cloud density reach, quality of visualisation and accuracy in terms of volume measurements.

The visualisation comparison is a simple task, using the same software (CC) for the same wall two projections (one point cloud obtained with CMS and the other with HM) are selected and assessed. The idea is to show the differences that are noticeable even to users with no mapping experience.

In the case of density comparison, within the same wall a small area is selected in the centre of the wall which corresponds to an area with some structural visualisation for the HM

scan, in this way the analysis it will be also easier and faster to process as the surface under study is less. The points inside this area are counted to determine the number of point per square meter with CC through the determination of number of points inside certain radius, or number of neighbours for a point inside certain radius. The radius utilised to perform the study is 0.5642m as with this the area of analysis is approximately $1m^2$ based on a circular neighbourhood.

In terms of accuracy, CMS outputs volume measurements and through that OB and UB can be calculated, comparing the difference of volumes between the extracted tonnes and measured tonnes. With HM scan the same measurement can be done and results compared with CMS.

5.6 First Case Study

5.6.1 Structural recognition

The first stage in determining the principal features of the GS is to cut the Stope A point cloud in CC, separating each wall. Despite Sirovision's ability to produce a 3D visualisation, the selection of the fractures needs to be done from a certain distance, enough to see the beginning and end of structures, thus rendering a 3D visual without overlap opposite walls. If the selection is made from inside the stope the distance is not enough to visualise the fractures in all their extension without running into the opposite wall. In other words, the idea is to visualise stope walls as if they were individual features in a similar fashion to slope analysis.

The analysis and comparisons will be performed in the HW, determining planes and traces on it, utilising an algorithm built in Sirovision. The structures are selected as follow:

- Plane: A plane can be selected when the surface has a clear shape and limits. Extreme points in the boundary of the plane are selected (a minimum of 3) the software instantly calculates the plane which better fits them (Figure 26a)).
- Traces: Sometimes the selection of a plane is not possible because the surface available is too small to recreate it, but the presence of a discontinuity is evident (Figure 26b)). The trace tool enables the selection of the points throughout the discontinuities calculating their normal vector, enabling a clustering process to select a plane that contains those vectors.

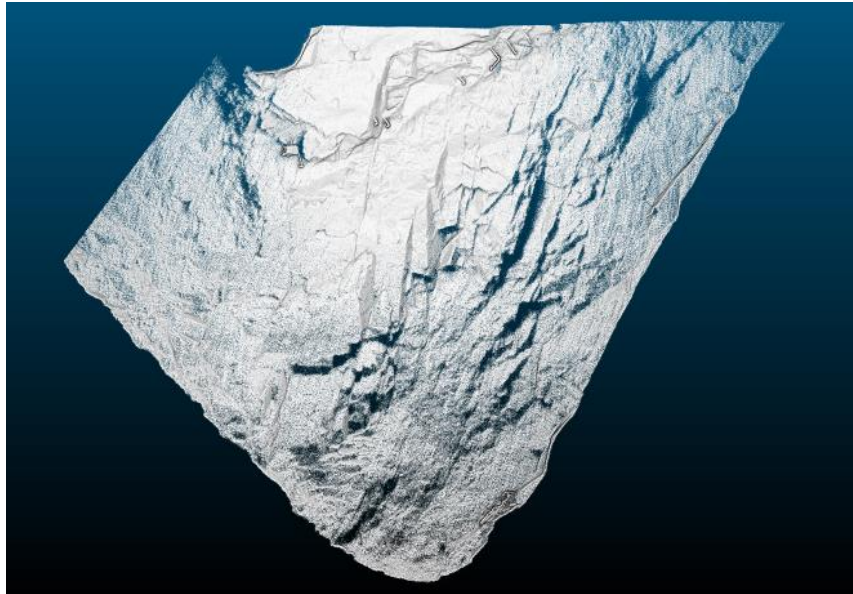


Figure 25. HW Case Study 1, CC visualisation

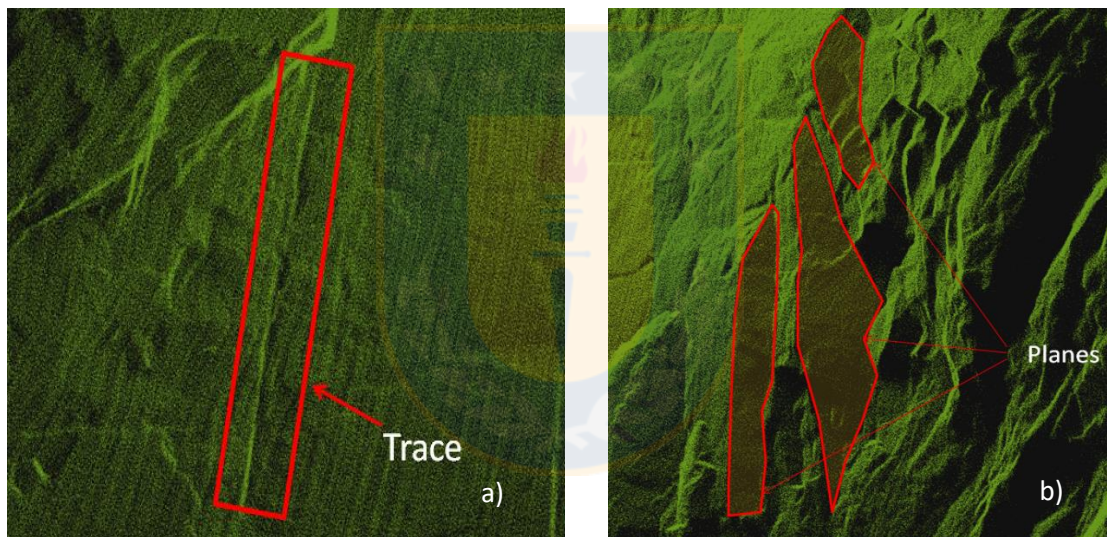


Figure 26. Sirovision3D visualisation with zoom, a) Trace in the HW and b) Planes in the HW

The results enable the determination of joint sets with Sirvision, choosing manually the groups of structures which will form the families with the tool “Define Set Orientation”. For each set defined, a list of information is obtained including the spacing, to determine the RQD using the J_v factor.

5.6.2 Semiautomatic versus Automatic

The second stage is to compare the results obtained with Sirovision (a semiautomatic recognition) against DSE (automatic recognition) and to estimate and show their differences in joints set determination.

Special attention must be paid to the recognition of traces, which can be one of the main problems in the automatic process. DSE works with the k-nearest neighbours (Knn) classification algorithm[59]that requires a minimum number of neighbours to create a cluster and traces sometimes don't have enough exposed surface to build the number of vectors required.

The data loaded in DSE is the same sample of the HW, containing up to 5.050.028 points in $405m^2$. A total of 5 tests were run to establish the optimum input parameters required to do the statistical analysis and perform the normal vector calculation, these are:

1. K or number of neighbours, in this case 50 neighbours are necessary to create a plane. Less than that will divide the surface in multiple planes because of a small angle of difference between normal vectors and number higher than 50 will render a single plane
2. The number of bins or categories of classification considered is 16, this establish that maximum of 16 families would be formed. For a statistical purpose is enough. A higher number of bins will increase the time of calculation and the number of joint families even without significant differences amongst them.
3. Minimum angle between principal poles is 15 to ensure the correct classification. The principal pole correspond to the normal vector of each selected plane and to classify the planes as part of the same group the difference between their principal pole is going to be less than 15° .

5.6.3 Rock mass characterisation

To demonstrate the different applications and to probe the use of HM for geotechnical purposes a rock mass characterisation is performed in the HW using the structures and information obtained with Sirovision (Table 13, Appendix B) and taking advantage of the good resolution achieved with the scan. The calculation will performed in the centre of the wall to ensure representativeness.

After determining the principal joint sets and calculate the main spacing of each (measured with the same software) the S_n factor is ready to be used enabling the determination of the J_v factor (Equation 2.1) to finally estimate the RQD of the rock mass.

A complete stability analysis cannot be executed due to lack of key geotechnical information as principal efforts, slope orientation, and RM density.

5.7 Second Case Study

The first step for this case study is determine a problematic area to work on it, the area selected is the one with presence of UB, because it is one of the principal components with direct effect on slope performance and in specific for this case study .

The UB zone is located between the HW and the east wall (Figure 27) showing more evidence of damage in the HW.

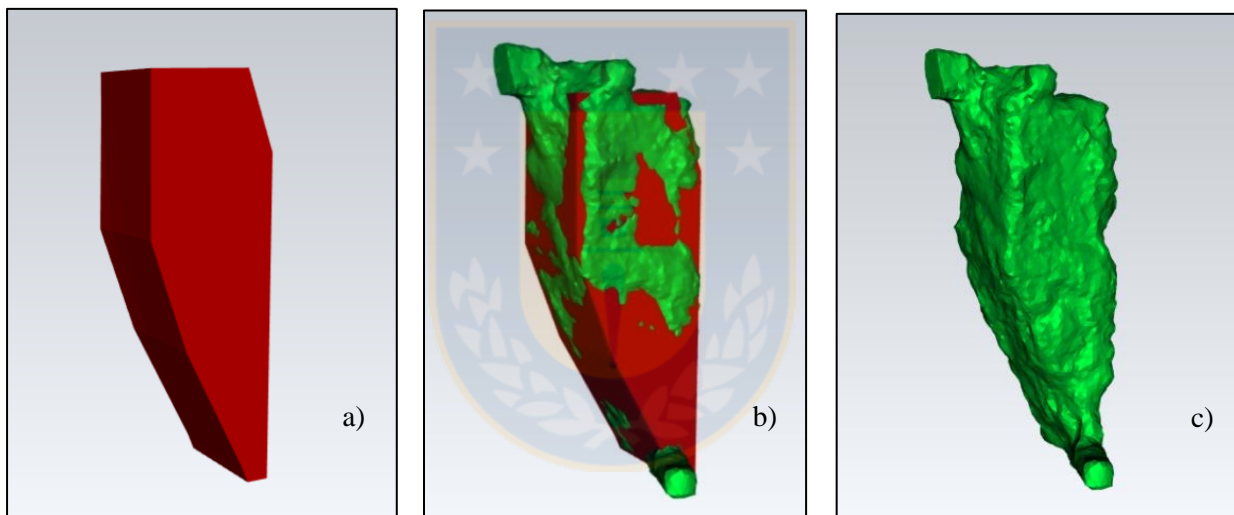


Figure 27. Slope B; a) Designed Slope; b) Designed Slope and final shape difference; and c) Final Shape scanned with CMS

5.7.1 Structural recognition

Figure 28 shows the Slope B point cloud scanned with HM, presenting a good resolution product of a high point density, for the structural recognition analysis purposes is an important feature. In this case only one wall is selected, based on the blasting results on it and UB presence, the HW.

The software utilised for the extraction of GS is Sirovision as most of the structures visualised are traces or not defined enough to use DSE.

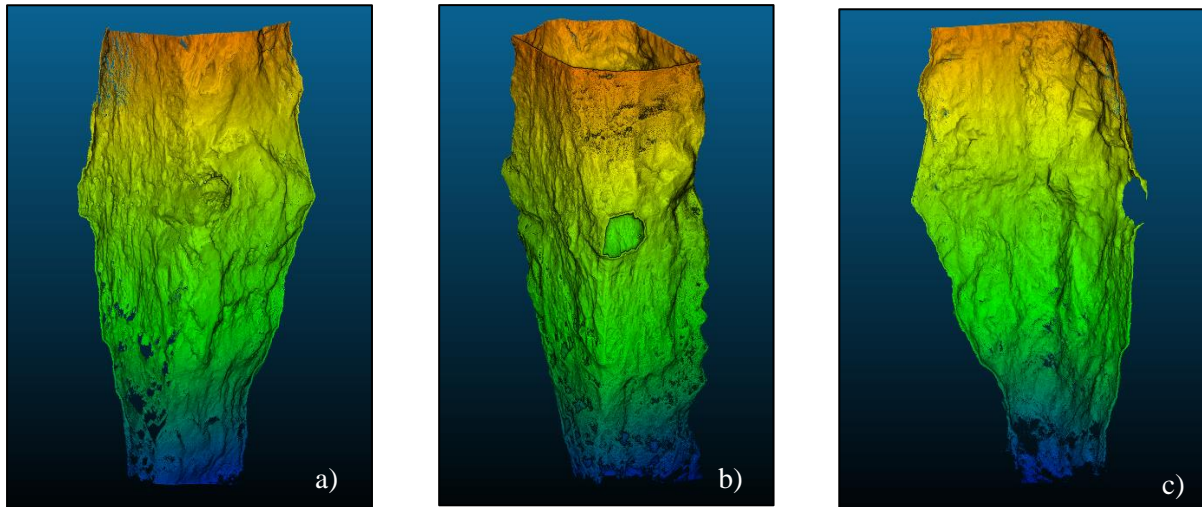


Figure 28. Stope B point cloud; a) East Side inside view; b) Isometric view complete stope; and c) West Side inside view

5.7.2 Stability analysis

The stability analysis was performed using Mathew's Graph. The inputs for this study correspond to a geotechnical information proportionated by the mine company (Table 1) and parameters calculated in the structural recognition stage. As in the previous case the first step is estimate the RQD (Equation 3) using Sirovision spacing results to calculate the J_v factor.

Table 1. Stope B geotechnical properties

| Property(HW) | Value |
|----------------------|-----------------------|
| Density | 2.84 t/m ³ |
| Friction Angle | 34.5° |
| Compressive Strength | 48 MPa |
| Q' | Good (10.3) |
| HR | 7.7 |
| RQD | Good (82%) |
| N | 6.2 |
| Portencial Stability | Unstable |

The information available allows a comparison between the stability estimated by the company, with core logging and the stability estimated with the extraction of GS on the HM scans.

5.7.3 Energy distribution

Figure 29 a) shows the designed stope with position of the blastholes in the UB zone while in 29 b) the CMS scan enables the projection of the blast design and the virtual position of the blastholes on them, making the UB problem patent. The study starts picking the rings directly involved in the UB generation per level, to perform a blast simulation in the zone (Figure 29b)):

- 320 m level: ring 3, ring4, ring 5 and ring6, all the holes drilled up from the drive.
- 280 m level: ring 4, ring5 and ring 6, all of them drilled down from the drive.

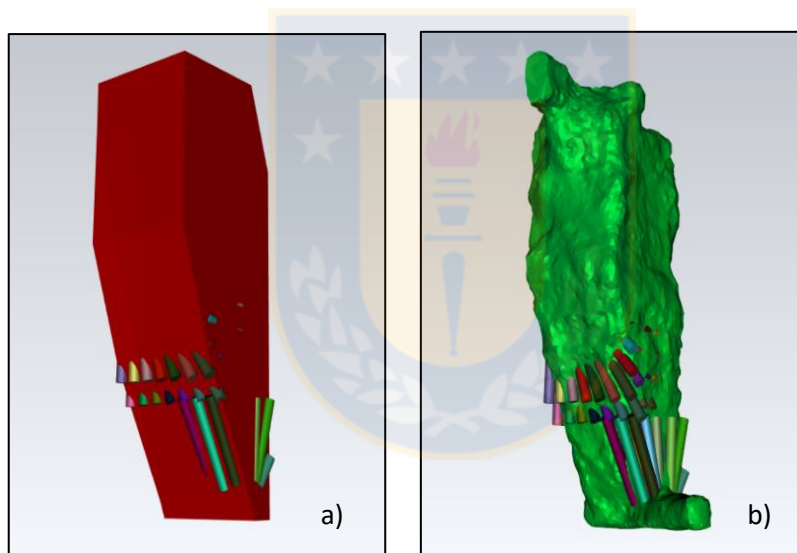


Figure 29. . Rings involved in the UB; a) Designed stope and blastholes disposition; b) Final shape and evident UB

It is also necessary to perform the same assessment on a zone with good performance to have a base of comparison. In the good performance section the rings involved selected are in the same level (Figure 30):

- 260 m level : ring1, ring2 and ring3. All of them drilled down from the drive

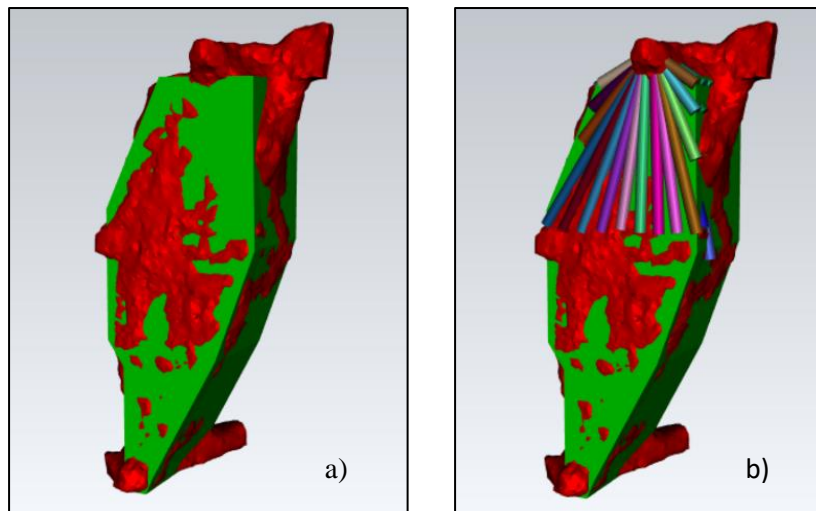


Figure 30. Rings involved on a good performance; a) Designed stope and blasthole disposition; b) Final shape

Each blast ring contains information such like: dip angle, length of charge, stemming length, emulsion density and superficial delays as is shown in Table 2, an example of information from the Ring 6 in level 280mLv.

Table 2. Ring information to set up the blast

| Ring | Emulsion density (Kg/m ³) | Real Length (m) | Stemming (m) | Charge Length (m) | Dip (grades) | Surface Delay (ms) |
|------|--|--------------------|-----------------|----------------------|-----------------|-----------------------|
| 1 | 0.96 | 18.9 | 1.0 | 17.9 | 272.0° | 6125 |
| 2 | 0.96 | 19.0 | 1.0 | 18.0 | 269.0° | 6135 |
| 3 | 0.96 | 19.2 | 7.8 | 11.4 | 261.0° | 6145 |
| 4 | 0.96 | 19.9 | 3.0 | 16.9 | 253.0° | 6155 |
| 5 | 0.96 | 20.8 | 9.5 | 11.3 | 246.0° | 6165 |
| 6 | 0.96 | 22.4 | 1.0 | 21.4 | 239.0° | 6175 |
| 7 | 0.96 | 24.1 | 10.1 | 14.0 | 232.0° | 6185 |
| 8 | 0.96 | 21.4 | 3.0 | 18.4 | 226.0° | 6190 |
| 9 | 0.96 | 19.2 | 9.3 | 9.9 | 220.0° | 6195 |
| 10 | 0.96 | 16.8 | 1.0 | 15.8 | 212.0° | 6200 |
| 11 | 0.96 | 15.8 | 7.4 | 8.4 | 204.0° | 6205 |
| 12 | 0.96 | 14.8 | 1.0 | 13.8 | 195.0° | 6210 |

The simulation in JkSimBlast requires an adjustment in the dip angle (Table 3). In the blast design a dip of 0° means a horizontal drilling on east direction and from there angles are measured in counter clockwise direction up to 359° , which would leave 180° as an horizontal hole in west direction. In JkSimBlast the 0° is considered as a vertical uphole, from there in the angles are measured in two ways: counter clockwise, with negatives going down until -179° and on clockwise direction or positive from 0° to 180° . A graphic representation in Figure 31 describes the difference.

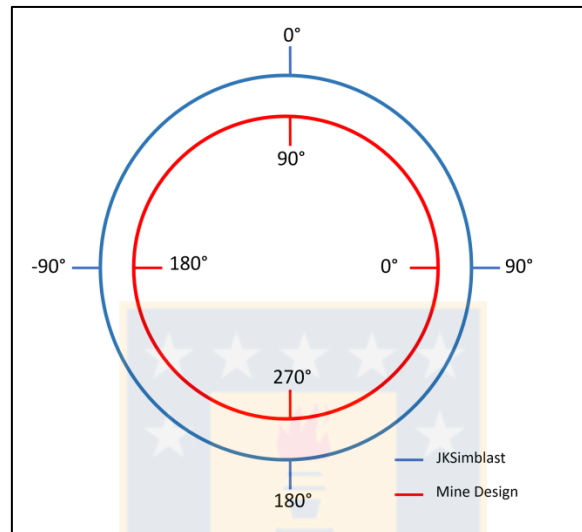


Figure 31. Dip angle difference between JkSimBlast and company design

Table 3. Angles adjustment to work with JkSimBlast

| RING6 | Dip | Dip Adjusted |
|--------------|------------|---------------------|
| 1 | 272.0° | 178.0° |
| 2 | 269.0° | -179.0° |
| 3 | 261.0° | -171.0° |
| 4 | 253.0° | -163.0° |
| 5 | 246.0° | -156.0° |
| 6 | 239.0° | -149.0° |
| 7 | 232.0° | -142.0° |
| 8 | 226.0° | -136.0° |
| 9 | 220.0° | -130.0° |
| 10 | 212.0° | -122.0° |
| 11 | 204.0° | -114.0° |
| 12 | 195.0° | -105.0° |

The blast design supplied by the mine company is loaded in GEM4D (an open source software focused on geotechnical engineering purposes), to get the X, Y, Z coordinates of the ring pivot and ring plane.

Then the model construction starts, situating each ring on their respective position for a 3D representation, once the process of design is finished the blast simulation can be implemented. With the 4D energy distribution analysis is possible to visualise the blasting results considering the timing. The main purpose is to execute a back analysis of the wall conditions after blasting to figure out the impact of GS in blasting outcomes and stope performance.

5.7.4 HM Comparison to CMS

5.7.4.1 Difference of volumes

The main purpose of CMS is measure the volume of the empty cavern left after the mineral extraction is finished and the percentage of UB and OB and their location can be based on this information. The area of short term planification use the Mined Tonnes as reference to estimate the discordance with the Disagned Tonnes, leaving CMS as a reconciliation tool or a tool to ensure the results (measurement of volume) and identify the areas of OB and UB.in terms of geometry

The results obtained with CMS provided by the mine are displayed on Table 4:

Table 4. Volume measurements performed with CMS

| Mined Tonnes (Mine Market) | Designed Tonnes | CMS Tonnes (Recognised) | Overbreak (%) | Underbreak (%) |
|---------------------------------------|----------------------------|------------------------------------|--------------------------|---------------------------|
| 67406 | 68436 | 65560 | 5.8% | 8.2% |

CMS results are calculated again using the stope design as reference (Figure 30) which is the same base of comparison to the HM scan. The process starts with the conversion of the point cloud scan (entire stope) to a mesh, then the new surface is closed and the volume inside can be calculated. All the procedure is done using 3DReshaper software [60] through an interpolation process of two steps, entering a minimum distance between points and an area of triangulation, after that the software calculates the volume (Figure 41).

5.7.4.2 *Difference of density*

In this case study the point density of the clouds obtained with HM and CMS respectively will be calculated using CC through the estimation of neighbours for the radio of analysis. The density calculated for CMS will be corroborated using the “power function” in Microsoft Excel, for that is necessary to export the coordenates X, Y Zof the points and apply Equation 6 to calculate distances.

5.8 Case 1 and Case 2: Comparison of resolution

The quality of the point clouds and their surface representation suggest an analysis and comparison of them to figure out the optimum point of work for geotechnical purposes.

5.8.1 First analysis

As a first stage, a density analysis is carried out using CC, analysing the point clouds quality (resolution)focused in the HW sample both case study. Furthermore, the density is going to be related with the drone trajectory information, based on the velocity, distance from walls and quality reached.

To measure the velocity the trajectory will be divided in intervals of 10 seconds, considering only the portion of the trajectory inside the stope and measuring the distance per interval; the perpendicular distance between the drone and wall is also considered. Then the scan quality per track would be classified in three categories:

1. Basic: Null structural representation, the information can be used for volume measurements but not for geotechnical analysis. Quality similar to CMS.
2. Nominal: It is possible to recognise some of the principal structures but the determination of their Dip and Dip/Direction is complicated.
3. Optimum: The presence of structures is clear, determining the Dip/Dip Direction can be simple, in combination with previous and subsequent tracks it is possible to appreciate the structures persistency.

5.8.2 Second analysis

A surface of 119 m^2 with good structural resolution in the HW from Case 1 is selected to determine three features that set up an efficient scan flight for geotechnical purposes:

1. Distance (m): Trajectory or total length described by the drone during a certain flight time.
2. Pattern (sec/m): Describes the different diagrams or shapes in which the flight can be performed above the surface, considering the time, distance and area involved. The pattern is calculated multiplying the total time of flight by the distance; all that divided by the area scanned.
3. Range (m): Is the perpendicular distance between the drone and the surface under analysis. A higher range means a bigger area of measurement but at the same time a higher distance from the surface.
4. Sampling Effort Variable (sec/m^2): Is a factor which measures how much effort or how much time should be applied on a surface (area). The Sampling Effort Variable is calculated dividing the Pattern by Range.

The trajectory of the drone in this case is divided in three tracks:

1. 39 – 70 sec: Flight from entry to the bottom of the stope, travelling downwards
2. 71 – 110 sec: Drone travelling at the bottom of the stope, approaching the wall.
3. 111 – 140 sec: Flight back from the bottom to the exit of the stope.

The trajectory file from CC is exported in .csv format with the respective coordinates X, Y and Z, then the distances are calculated. The trajectory is divided according to the timing (three sections described above), then the distance between each point is obtained using the Equation 6 to finally sum all the distances between subsequent points contained in each period of time. Range estimation is carried out with 3DReshaper using a measuring tool to calculate distance between pointclouds, this is because the surface under study and the trajectory are loaded as pointclouds, with the difference in the Z axis corresponding to the distance between the surface and the drone.

6. Results Analysis

6.1 First Case Study

6.1.1 Structural recognition

a) DSE Analysis

The automatic recognition determined three joint sets (Table 5).

Table 5. Joint sets determined with DSE in the HW

| Set | Type | Dip | Dip Direction | Density | % |
|------------|-------------|------------|--------------------------|----------------|----------|
| J1 | Pale blue | 54.03 | 78.68 | 3.41 | 62 |
| J2 | Yellow | 70.52 | 278.13 | 0.31 | 7.3 |
| J3 | Red | 81.37 | 215.56 | 0.11 | 5.8 |

The results are not considered representative or reliable enough because:

1. According to DSE, the first set determined (J1) represents 62% (Figure 32) of the total surface, which is not correct. There is indeed a set of structures with a similar Dip and Dip-Direction as the measured J1 in the HW but the software classifies the entire wall as part of the same family of structures.
2. The software does not recognise traces, which can lead to loss of important information.
3. A recurrent problem in the data collected with LiDAR is the presence of shadow or low-density sectors especially in non-planar surface such as stopes, produced by the angular deviation. The areas without sufficient points were ignored leaving behind relevant parameters and information as spacing and persistency. For example in Figure 32 a), there are a series of structures in the right side of the wall (inside the circle) which should have been classified as part of the J2 set (yellow).
4. For walls of this size the processing time can take longer than an hour.

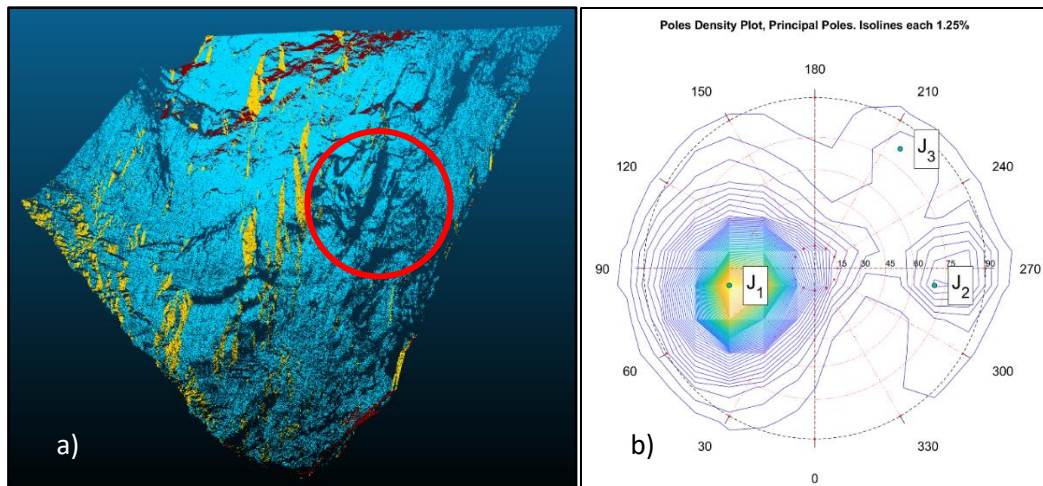


Figure 32. a) Joint sets visualisation; and b) Planes poles concentration estimated with DSE

B) Sirovision analysis

With the structural analysis made with Sirovision 4 main joints sets were determined using more than 80 structures (Table 13, Appendix B) to estimate the families. It is important to mention that this selection of families was not automatic, after the structural recognition Sirovision plots the concentration of poles planes and allows for automatic or manual selection, the former was chosen.

Sirovision presented several advantages over DSE:

1. Sirovision enables the recognition of traces
2. Sirovision enables the determination of planes in low-density areas
3. It is possible to locate a new set of structures J4, in the centre of the stereogram (purple structures in Figure 33 b)).

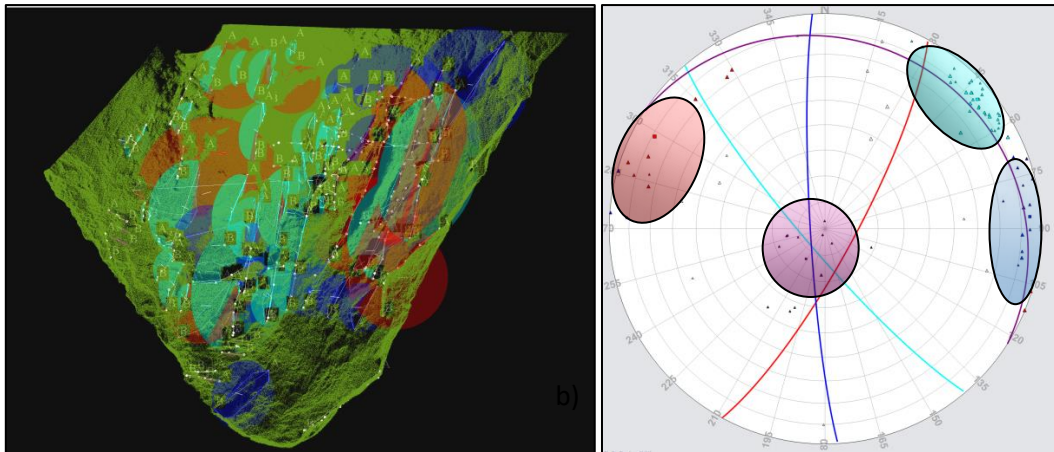


Figure 33. a) Joint sets visualisation; and b) Planes poles concentration estimated with Sirovision

These two points increase the accuracy of the results and with that the analysis acquires greater representativeness. It is possible to obtain a better characterisation of each set, calculating the spacing, persistency, orientation and maximum persistency (Table 6).

Table 6. Joint sets estimated with Sirovision in the HW, Case1

| Set | Type | Dip (°) | Dip Direction (°) | Max Persistence (m) |
|-----------|--------|---------|-------------------|---------------------|
| J1 | Aqua | 81.9 | 229.5 | 9.011 |
| J2 | Red | 78.9 | 118.5 | 12.433 |
| J3 | Blue | 84.4 | 266.6 | 6.863 |
| J4 | Purple | 13.4 | 32.3 | 2.966 |

Some similarities with DSE can be mentioned, amongst them the joint sets recognised had similar features, although DSE utilised less structures to characterise each set and the difference in terms of Dip and Dip Direction is important (Table 7). The biggest difference occurs in the J1 because with a net difference of 24.87° , as was mentioned before, this set was built in DSE using the wrong normal vectors due to a lack of points, losing representativeness.

Table 7. Comparison and angular difference between results obtained with DSE and Sirovision

| | Dip Net Difference (°) |
|-----------|------------------------|
| J1 | 24.87 |
| J2 | 13.88 |
| J3 | 0.53 |

6.1.2 Rock mass characterisation

Using the structures and information obtained with Sirovision (Table 13, Appendix B) the RM characterisation is displayed to determine the RQD of the HW. The calculation will be performed in the centre of the wall to ensure representativeness.

The spacing for each set was calculated also with Sirovision (Figure 34) measuring the perpendicular distance between structures per set. For families with an irregular fracture frequency this can be an issue at the moment of estimating an average spacing within a large surface.

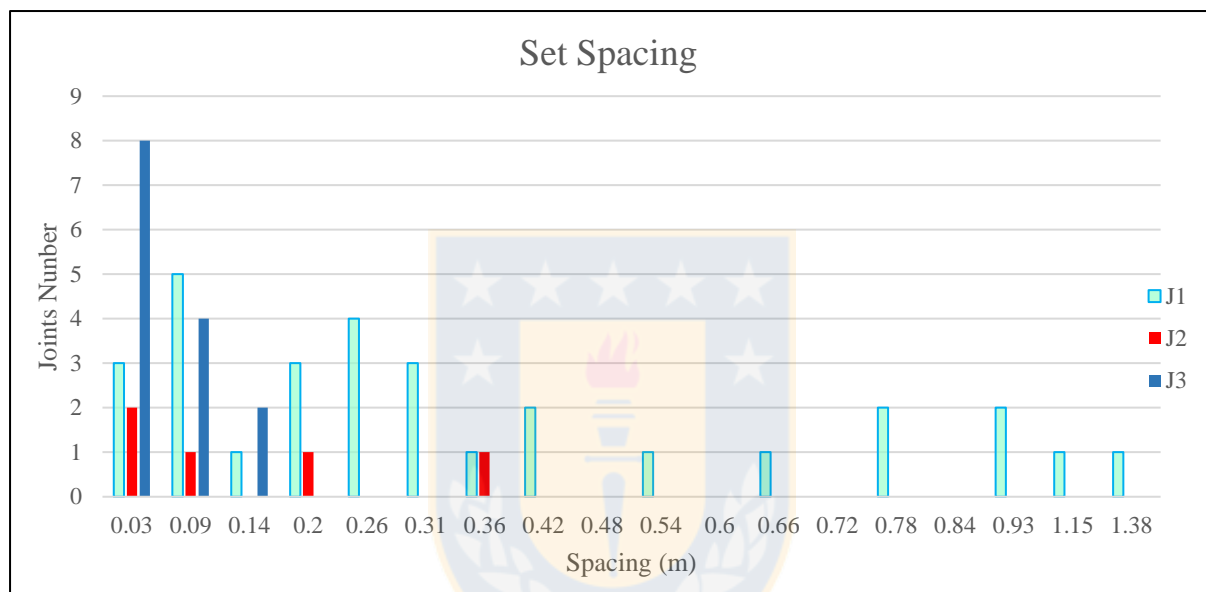


Figure 34. Histogram of spacing per set calculated with Sirovision, Case 1

Following Equation 3 it was possible the RM quality was classified as poor with an RQD of 45.85 (Table 8) which can cause problems of stability and probable dilution, keeping in mind other factors that should be considered. The variability of RQD was also observed and the importance of a detailed and precise estimation: when the entire wall is considered the RQD rises to 82.39 entering the category of good quality. This change is due to the difference of fracture frequency within the wall even when the same joint sets are considered.

Table 8. RQD and S_n factors estimated with Sirovision, set influence

| Set spacing | Spacing Factor (official) | Spacing Factor (complete) |
|-------------|---------------------------|---------------------------|
| S_1 | 0.409 | 0.409 |
| S_2 | 0.079 | 0.523 |
| S_3 | 0.171 | 0.171 |
| | $J_v = 20.9$ | $J_v = 10.19$ |
| | $RQD = 45.85$ | $RQD = 82.39$ |

6.2 Second Case Study

6.2.1 Structural recognition

In the HW analysis with Sirovision it was possible to recognise 39 structures (Table 14, Appendix C) between planes and traces concentrated in the centre of the wall (Figure 35 a)). The structures were classified in three main joint sets (Table 9). The plot of the poles and main planes formed by the selected GS is show in the Figure 35 b).

Table 9. Joint sets estimated with Sirovision in the HW, Case 1

| Set | Type | Dip(°) | Dip Direction (°) | Max Persistence (m) |
|-----------|------|--------|-------------------|---------------------|
| J1 | Red | 78.4 | 37.7 | 15.4 |
| J2 | Aqua | 65.4 | 352.7 | 9.7 |
| J3 | Blue | 74.8 | 287.3 | 11.9 |

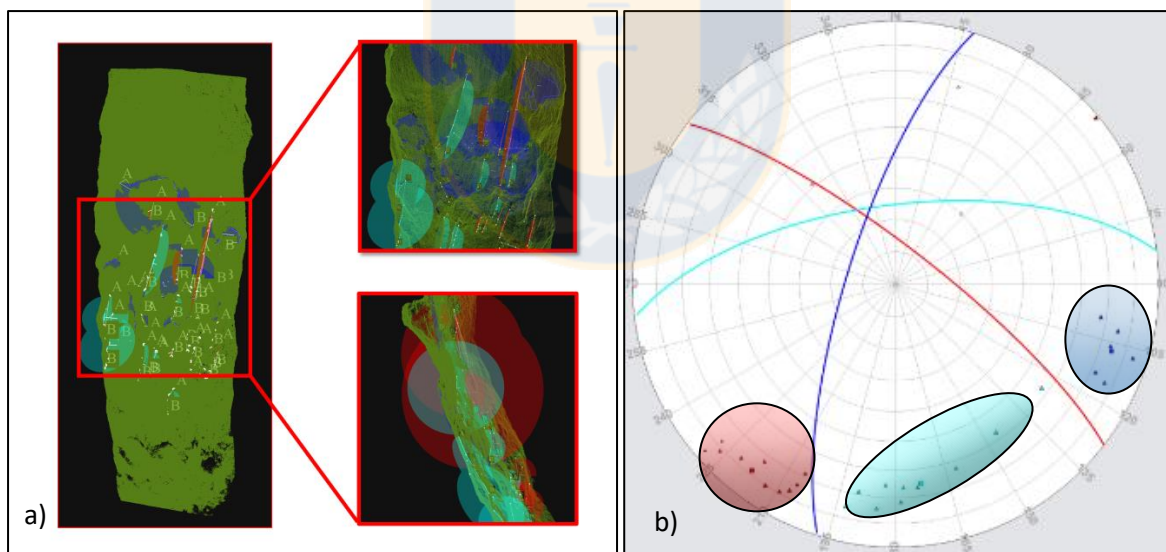


Figure 35. a) Joint sets visualisation; and b) Planes poles concentration estimated with Sirovision, Case2

The structural information in the HW (Figure 36 a)) registered through core logging by the mine was corroborated with HM, as shown in Figure 36 b) the structure represented by a disk is the projection of the green structure behind the wall which was determined previously during the drilling campaign. With HM it was possible to observe how this structure followed its projection and crossed the HW.

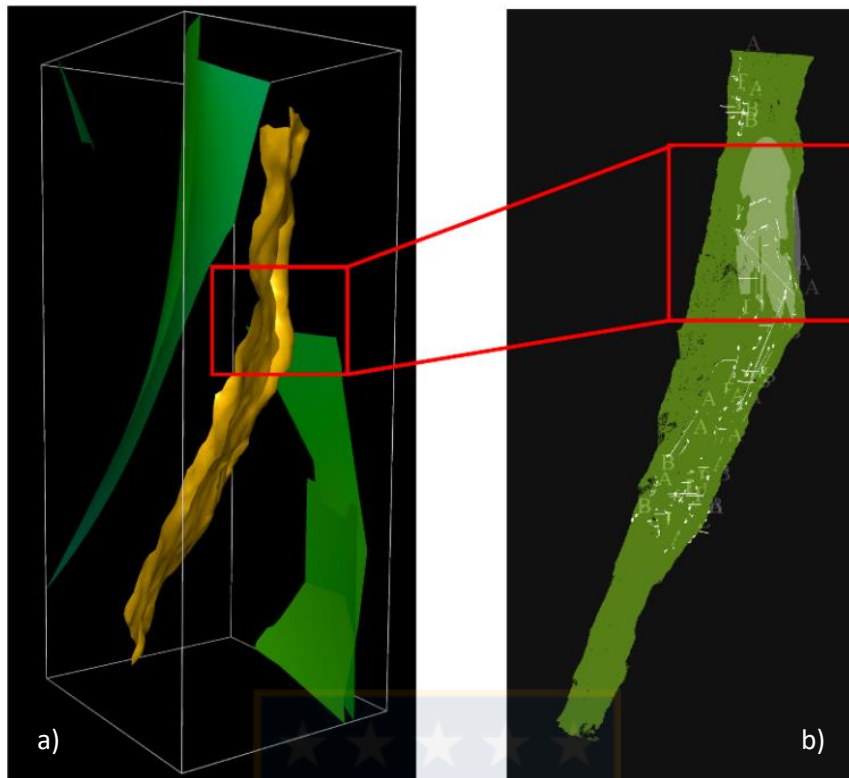


Figure 36.a) Planes estimated with core logging; and b) Plane continuation obtained with Sirovision

There are several structures which were localised with HM (Figure 35 a)) which are not included in the mine geological model. These structures are missing from the model because, to determine a geological structure as a fault or joint a minimum number of cores drilled in different positions and directions are necessary. As this type of models are a secondary result of the drilling campaign conducted to delineate the orebody, only the main structures are large enough to be logged from different positions and present in the model, a situation generated from the scale effect.

The data collected (Figure 37 a)) with the cores classify the conditions in stope B ranging from perfect quality (RQD of 100%, in red) to a very poor quality (RQD of 0%, in blue).

A link between the data obtained with core logging and HM can be observed, specifically in the area where the RQD is on a range between 20 to 40 percent (red windows) which concur with a high fracture frequency in the same zones on the HM scan. However there is an incongruence between core logging and HM results at the wall bottom, where the quality of the RM tends to decrease according to the core information. The difference is caused by the impossibility of structural recognition (HM scan) in the area due to the presence of noise and a lower surface resolution representation.

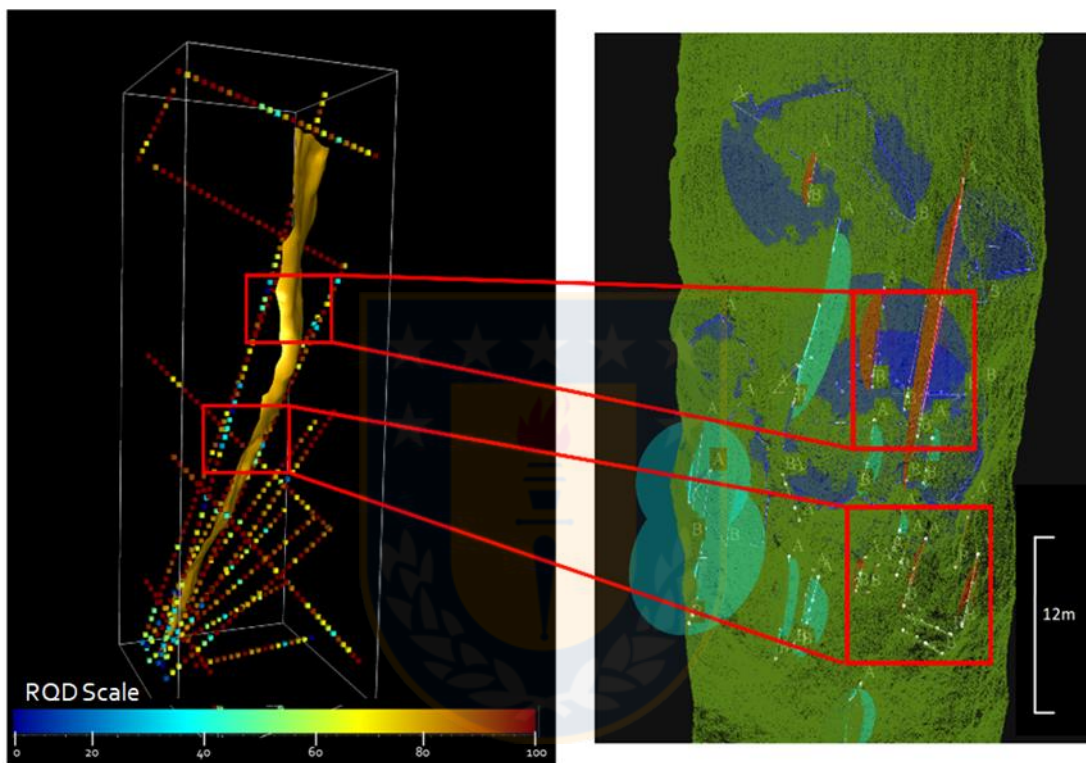


Figure 37. a) RQD estimated with core logging; and b) Joint concentration calculated with Sirovision

6.2.2 Stability analysis

Using the structures and information obtained during the structural recognition with Sirovision (Table 14, Appendix C) the RQD is calculated for the entire HW using the S_n parameters per family of the Figure 38 and Equation 3.

Table 10. Joint sets estimated with Sirovision in the Stope B HW, Case 2

| Set | Colour Identification | Dip (°) | Dip Direction (°) | Max Persistence (m) |
|-----|-----------------------|---------|-------------------|---------------------|
| J1 | Red | 78.4 | 37.7 | 15.4 |
| J2 | Aqua | 65.4 | 352.7 | 9.7 |
| J3 | Blue | 74.8 | 287.3 | 11.9 |

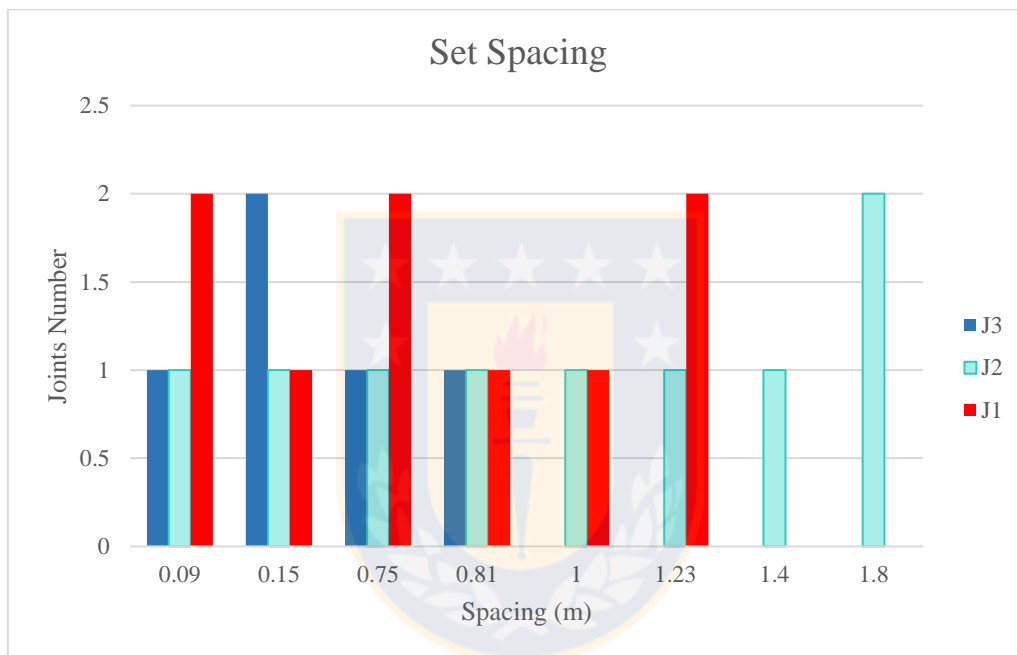


Figure 38. Spacing per set calculated with Sirovision, Case 2

The quality of the RM in this case is classified as very good with an RQD of 97.4% (Table 11). These antecedents in combination with the data presented in Table 1 enable a wall stability estimation.

The first step is to calculate Q' , for calculation purposes the factors: $J_n J_a$ and J_r were considered all together into one factor of 0.125 yielding a Q' of 12.17 (Equation 1). Then for the stability number the factors A , B and C followed the same procedure including all of them into one factor of 0.602. The final value for N is 7.33 which establishes a condition of failure or instability for the HW under study (Figure 56).

Table 11. RQD and Sn factors estimated with Sirovision, Case 2

| Set spacing | Spacing Factor |
|-------------|----------------|
| S_1 | 0.581 |
| S_2 | 0.603 |
| S_3 | 0.511 |
| | $J_v = 5.33$ |
| | $RQD = 97.39$ |

$$Q' = 97.39 \times 0.125 = 12.17$$

$$N = 12.17 \times 0.602 = 7.33$$

Despite the 15% difference between the RQD measured with core logging (82%) and HM (97%), there is not big discordance in terms of stability assessment; both results are situated in failure zone (Figure 56). This does not mean HM can replace core logging but can be use as reconciliation tool to ensure the correct estimation of this factors and get new and detailed information. The difference observed could be produced by the absence of structural information at the bottom of the wall for HM, zone which presents a low RQD.

Another point to keep in mind is that for this type of measurement (RQD) mine companies consider a volume around the wall of approximately 5 meters of width (2.5 meters behind the wall and 2.5 meters in front) enabling in the calculation the integration of structures which run parallel to the wall, an impossible task utilising only HM.

6.2.3 Energy distribution

A) Section with UB

The energy distribution analysis in the UB zone shows a discordance between the actual blast pattern design and the final shape. The limit of the excavation should coincide with a powder factor of 0.72 Kg/ton estimated by the mine blast design (Figure 57, Appendix D) which is represented in the energy distribution by the transition from green to blue (Figure 39). This zone is completely outside the expected shape (Figure 39 a)).

In terms a potential effect of geological structures and their orientation in stope performance the results are not conclusive, because:

1. The quality of the point cloud (noisy and low density) at the bottom of the HW is not good, which makes impossible a structural recognition.

2. There are other factors that should be considered on this type of analysis such as hole deviation. The real position is always different to the design specially when the design includes upholes.

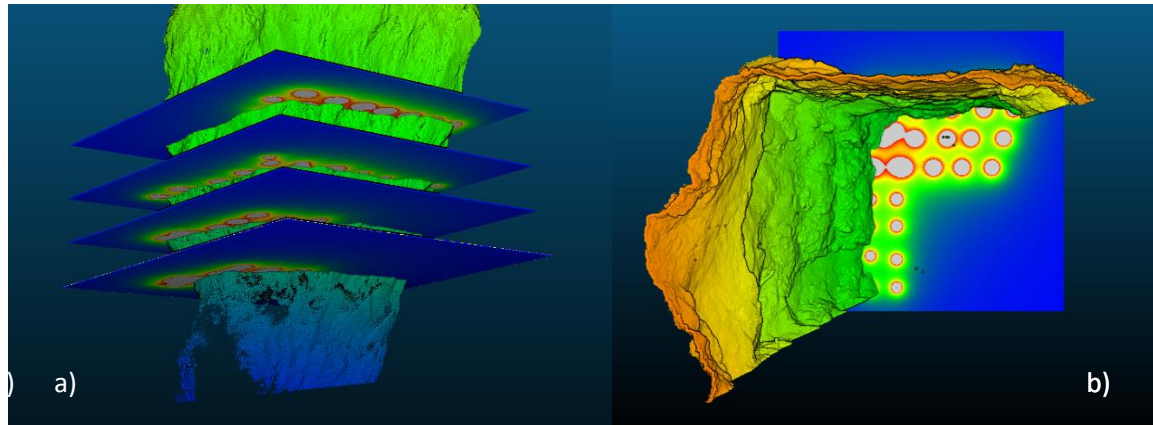


Figure 39. a) Isometric view; and b) plan view of energy distribution in the UB zone, Stope B

B) Section with good performance

In the section with a good performance the blast design seems to be performed correctly (Figure 40), nevertheless the results can not be conclusive, because:

1. Even when the density in this point is higher than in other zones the quality of the representation is still deficient for geotechnical purposes.
2. It is necessary to obtain the real position of the blastholes and include the hole deviation (angular) to perform a study.

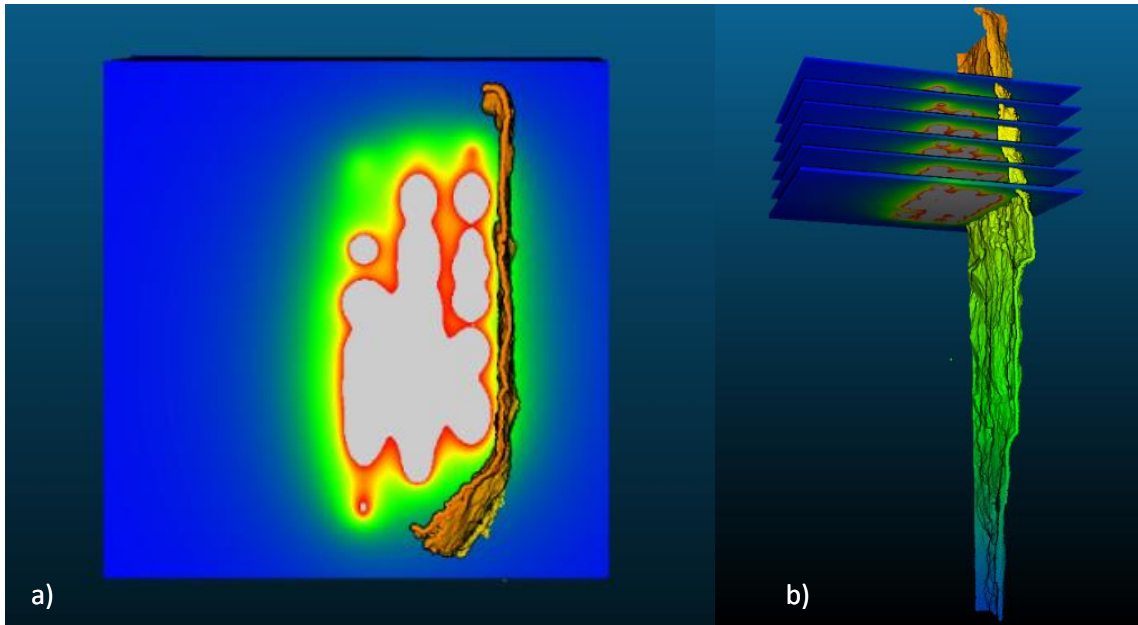


Figure 40. a) Plan view; and b) Front view of energy distribution in the zone with good performance, Stope B

6.2.4 Comparison between Hovermap and CMS

6.2.4.1 Difference of volumes

The estimation of the minimum distance and triangle area are the result of a series “Trial–Error” tests, with the objective of maintaining the representativeness. The representativeness problem is occasioned by the effect of density in the interpolation process during the creation of an estimated surface on low density point clouds, losing veracity. Figure 41 shows the difference between the meshes of both HM and CMS, the volume differs in 263 cubic meters and around 747 tonnes of mineral (considering an average density of 2.84 ton/m^3) approximately a 1.1% of extra tonnes recognised with HM being one of the key factors of that the improved point density in HM.

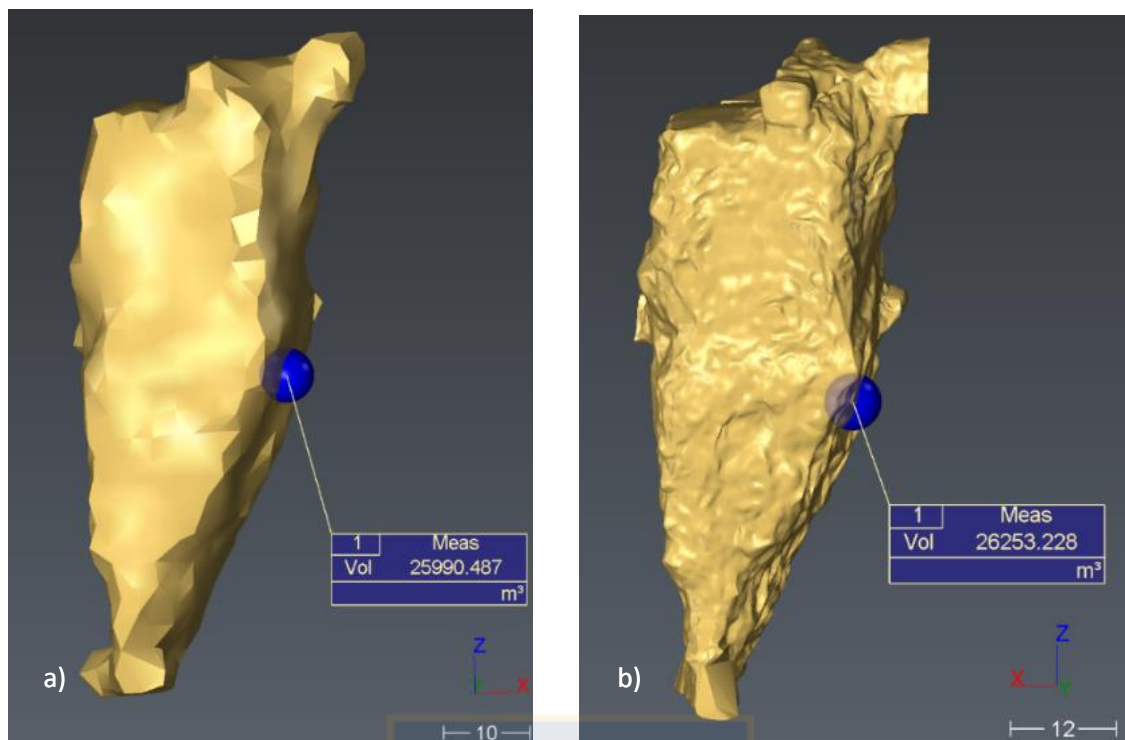


Figure 41. Volume measurements a) CMS mesh; and b) HM mesh

6.2.4.2 Difference of point density

Results show density of points as one of the most relevant differences between CMS and HM scans.

The difference between them is evident (Figure 61, Appendix E), with CMS the density calculated is of 2.63 points per square meter against 5000 points per square meter obtained with HM. Figure 42 exemplifies the situation, a HW portion from Stope B overlapping the point clouds generated with CMS and HM, where green surface is actually a high density point cloud which recreates in high detail the actual conditions of the RM, in the other hand the black dots above the surface represent the CMS point cloud.

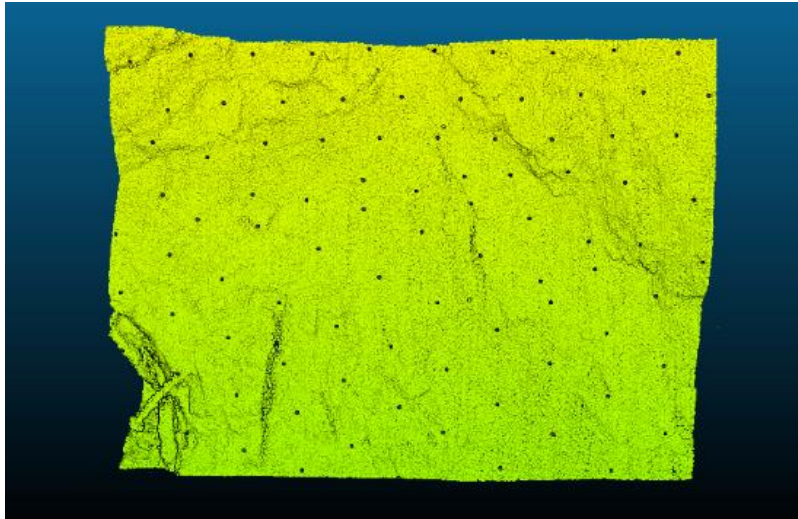


Figure 42. Point cloud obtained with HM (green) against point cloud generated with CMS (black)

The point density difference is produced by the lasers utilised on each technology, the CMS laser was created with a distance measurement purpose and with those results a volume calculation can be carried out. In the other hand, the laser mounted in HM was created for navigation purposes, it is the type of laser used by autonomous cars a case where the scan necessary has to be dense. The objective of the HM laser is to enable the instant decision making for a car or robot which is moving and avoiding obstacles at the same time.

6.3 Case 1 and Case 2: Point clouds difference

6.3.1 First analysis

Densities were compared as a first step to understand the difference between the HM scans qualities on both cases studies. It is important to mention in Case 2(Stope B) the scan setting up involved the alignment of two point clouds from two different access points, in the 260mlevel and the 280m level (Figure 62, Appendix F) to remedy a shadow present in the first measurement (260mlevel).

Figures 65 and 68 (Appendix F) show the concentration of points per square meter in a range of 3000 – 10000 points. The average point density shows a difference between Case 1(Figure 72, Appendix F) and Case 2 (Figure 69, Appendix F) of two times a higher number of points per square meter for Case 1. Which becomes evident when is take in consideration that for Case 2 the range of density under study represent the higher concentration while for Case 1 the same interval of evaluation or range represent the lowest concentration with an average over 30000 points per square meters.

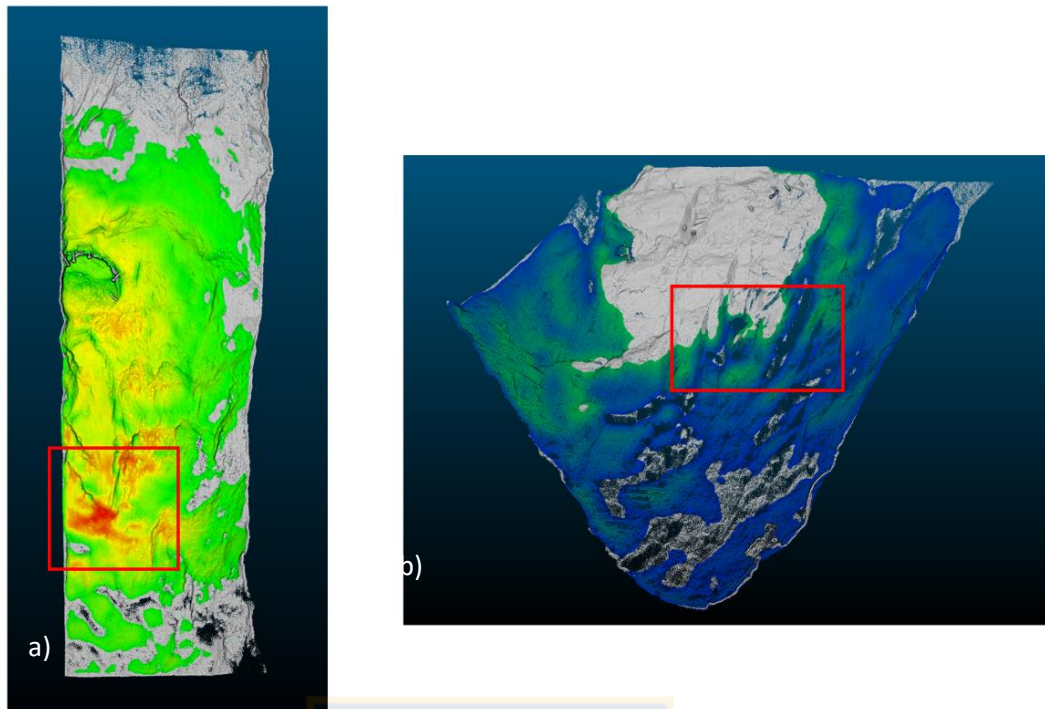


Figure 43. Point density a) HW Case 2; b) HW Case 1. Zones with the similar density represented by red squares

The results evidence the influence of more factors in the scan results, as an example in Figure 43 the coloured surface inside the red frames for both cases have the same density of points (The histograms of concentration or colour scales corresponds to Figure 70 and 73, Appendix F), but the quality and detail between them is completely different and even more for Case 1 that zone is in middle of the area with the best structural representation.

To continue with the analysis, the drone trajectories with their velocities and distances from the wall were examined for both cases:

a) Case 1:

The drone trajectory (Figure 65, Appendix F) describes the entire scan procedure in only one flight of 255 seconds, of which 140 seconds correspond to an effective flight, time where the drone was entirely dedicated to the stope scan. The main trajectory feature is how the drone flights around the stope and gets closer, stay surrounding the same area and return to the origin.

The relation between the velocity and distance from the walls during the drone flight analysing the scan quality during the trajectory (Figure 44, 45 and 46) show that: a low

velocity will increase the density but the only way to get data useful for geotechnical purposes is flying near to the walls.

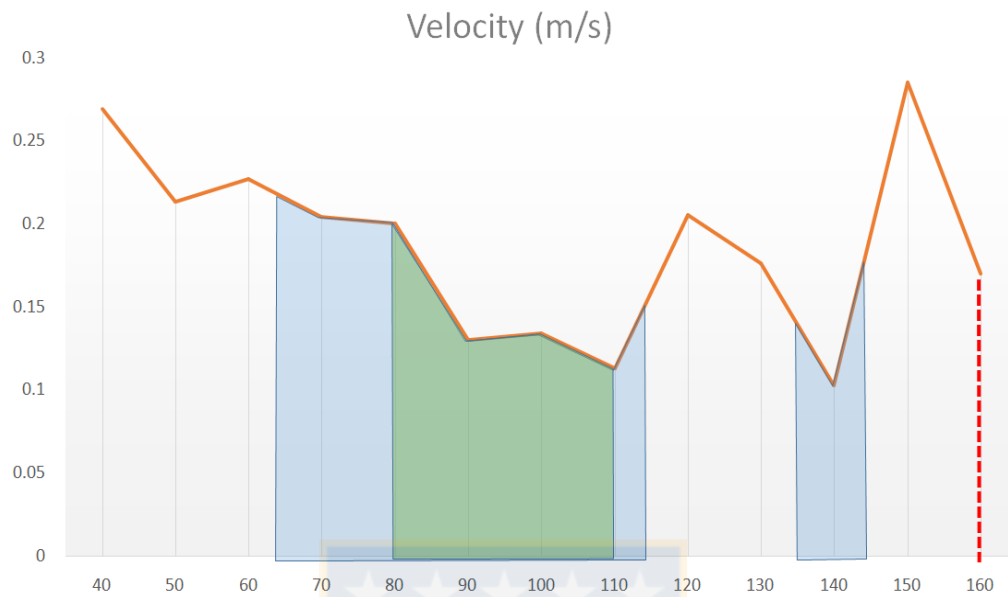


Figure 44. Velocity during the flight; green zone shows an “Optimum” performance, Case 1

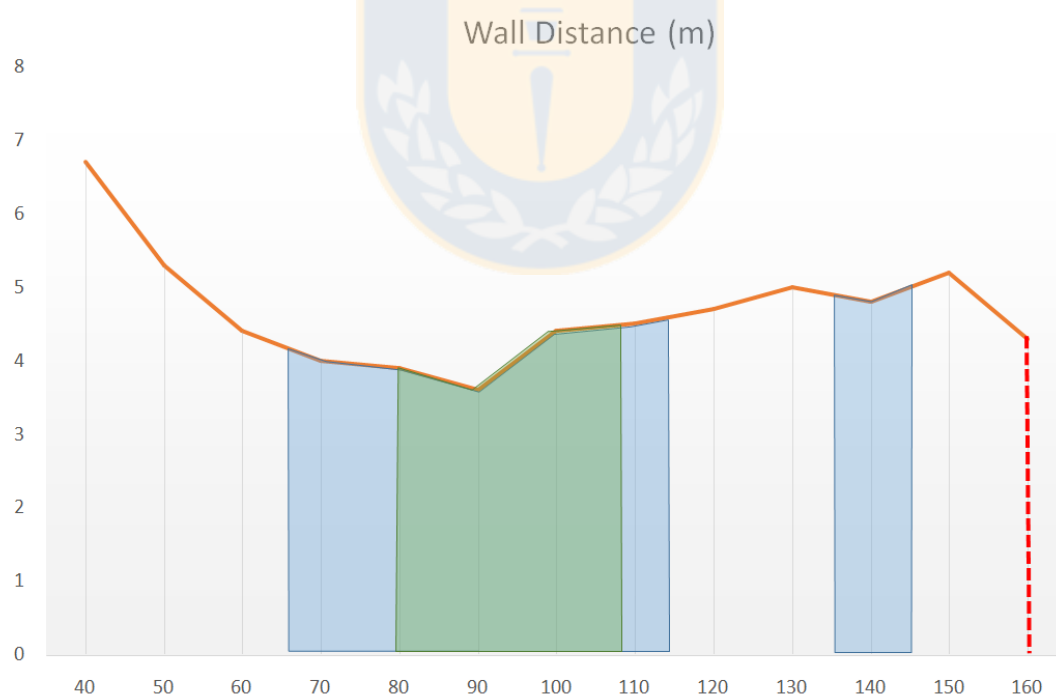


Figure 45. Distance to the wall during the flight; green zone shows an “Optimum” performance, Case 1

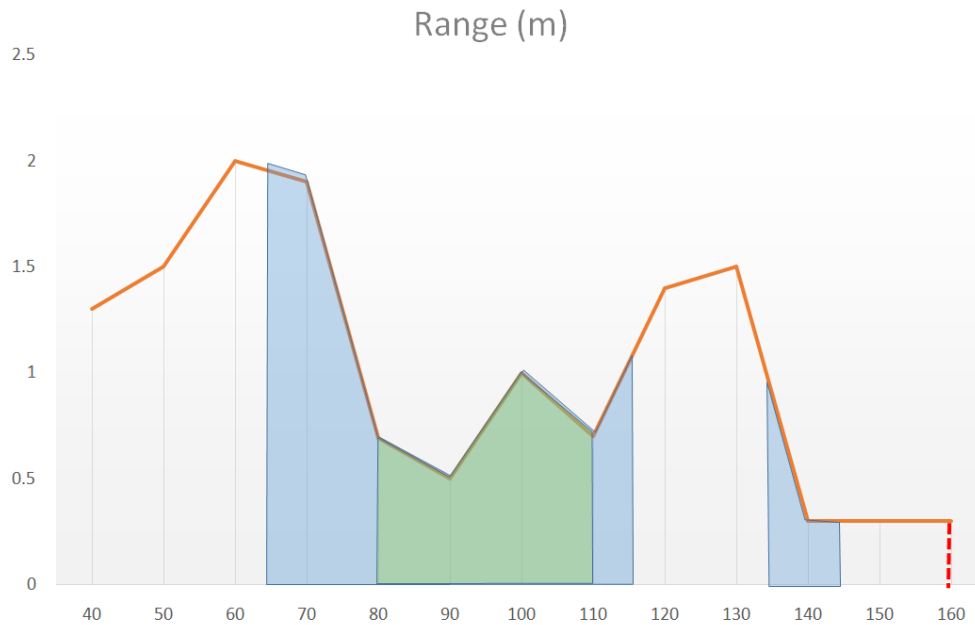


Figure 46. Range during the flight; green zone shows an “Optimum” performance, Case 1

Finally, the study reveals an optimum quality of scan between the seconds 80 and 110, for that period of time the drone described a trajectory with a velocity between 0.13 - 0.2 meters per second (Figure 44), and a distance from the wall between 3.6 – 4.5 (Figure 45).

b) Case 2:

As the creation of this point cloud involved the alignment of two scans from different levels two trajectories would be studied.

The scan performed from the 260m level (Figure 66, Appendix F) has a high presence of shadows in the HW, occasioned by the drone position during the procedure, generating angular occlusion and angular deviation. As an example, Figure 44 shows the effect of the position during the scan, the orange circles represent the drone, while the blue lines the pulses of light.

For a drone position as appears in Figure 47 a) there are zones which were not scanned, because of angular occlusion and angular deviation (red). The angular occlusion is linked to the “visibility” angle of the drone and the angular deviation is the separation between pulses of light generated by the drone distance from walls during the flight.

To avoid the problems of angular occlusion and angular deviation the drone should fly all around the stope, getting a visibility angle of 360° and taking a trajectory close to the walls, respectively (Figure 47 b)).

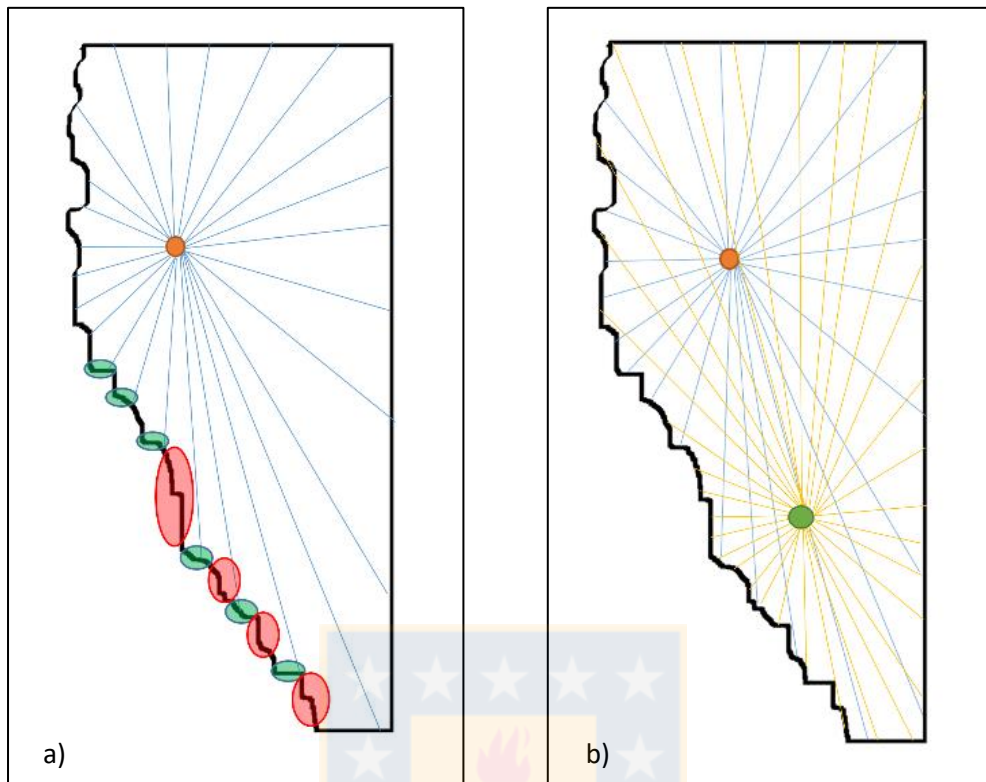


Figure 47. a) Limited trajectory, zones normally scanned (green), zones with shadow and angular obstruction (red); and b) Trajectory includes a flight along the slope to avoid shadow and angular obstruction

For the first scan and from a total of 66 seconds of flight only 30 seconds correspond to an effective flight (the drone was scanning only the slope). The drone position with respect to the wall generates angular occlusion and with that the entire scan is classified as Basic (Figure 66, Appendix F).

For the second scan (from 280m level) the conditions were different and the drone went completely inside the slope (Figure 65, Appendix F). From a total of 255 seconds flight 120 of them represented effective flight. Almost the entire effective flight shows a Basic scan quality, except for 20 seconds close to the end of the flight where the quality increases to regular. This improvement coincides with a decrease in speed, around 0.26 meters per second maintaining a distance from the walls nearly constant (11–12 meters).

On the same range of velocity for Case 1 the results were optimum but the distance to the wall was the half of that in Case 2, this shows the relation between the flight factors and suggests an optimal velocity range of 0.12 – 2.0 meters per second and wall distance range of 3.5 – 4.0 meters for the drone to achieve information for geotechnical purposes.

6.3.2 Second analysis

A deeper analysis enables the determination of the four flight parameters during the three different tracks (time intervals), Table 12 summarises the results of the study.

Table 12. Track analysis results, Case 1

| Trajectory | Distance | Time | Pattern | Range | SEV |
|-------------------|-----------------|-------------|----------------|--------------|------------|
| Track 1 | 6.87 | 31 | 1.78 | 5.75 | 0.31 |
| Track 2 | 6.02 | 40 | 2.01 | 4.92 | 0.41 |
| Track 3 | 4.32 | 30 | 1.08 | 5.74 | 0.19 |

In terms of scan quality the Track 3 showed an optimum performance and the opposite occurs with the Track 2 (Figures 73, 74 and 75, Appendix F). These results were corroborated with the SEV calculated for each track demonstrating the important relation between velocity, wall distance and time spend during the scan.



7. Conclusions

All the process and stages of analysis applied to HM data have shown the potential of this instrument to be utilised as a new source of information, enabling the creation of an alternative approach for geotechnical analysis in underground mines.

Furthermore, the quality and accuracy of HM were demonstrated in terms of volumetric measurement, although the difference in percentage terms is only 1.1% between the mined tonnes calculated by the mine and the volumetric analysis made to the HM scans for Case 2. In situations as complex stopes shapes and high probability of shadow for CMS scans, HM will perform without problem, ensuring the representativeness and avoiding the excessive interpolation which turns into lack of information.

The detail of the point cloud of HM can be adjusted according to the purpose of analysis changing the point cloud density. The accuracy also was demonstrated through the recognition of structures in both case studies. Specifically the comparison between the RQD and geological model provided by the mine and the structures recognised with HM is a good example of its capacity. Nevertheless, the point cloud present some drawbacks as the size of the files and the amount of information which difficult the processing of results, is important to understand that more points does not mean a better surface representation, is just one factor to take in consideration in combination with others like for example: drone velocity, distance from walls and flight pattern.

The structural data collected with HM and analysed with Sirovision enables a complete stability study estimating a volumetric fracture factor and the use of Mathew's Graph. The results in Case 1 were satisfactory in terms of structural recognition, unfortunately this information could not be compared against a standard. The results for the same analysis in Case 2 showed a good performance with only 1.13 points of difference in the stability number calculated and the information granted by the mine. According to the results that difference was occasioned by an accumulation of noise at the bottom of the wall, same zone with the lowest RQD, another factor that could influence the results is the limited information given by the mine which affects the quality of the standard comparison.

The difference of qualities between both cases opened an assessment to determine the optimum circumstances and conditions of data collection, with the following results:

- Optimum results were achieved during a flight velocity between 0.12 – 0.2 meters per second and maintaining a distance from the wall no more than 5 meters.
- The scan results would improve if the flight is carried out all around the stopes, in order to prevent angular deviation and angular occlusion.
- The key factor to perform a scan for geotechnical purposes is to ensure the SEV and maintain a balance between velocity and time spent to obtain the scan of certain area.

From an industrial perspective the HM data needs to be improved to make it user friendly and big data techniques employed to reduce the time of processing and analysis.

The performance of Sirovision shows auspicious results, evidencing a clear advantage over DSE, because:

- The Automatic software do not recognise traces.
- HM and in general all the laser scans had evidence of shadow which hinders the recognition of structures automatically (not enough points)
- Processing time in DSE is too high (over one hour for 350 square meters area) for automatic software.

HM has shown the potential to continue improving and bringing new information to the underground mines on a process of continuous adaptation.

8. Future work and recommendations

Recommendations and future work arising from this thesis follow:

1. It is necessary to test the HM performance under high humidity and dust conditions, principal problems in underground mines and a recurrent issues for CMS scans.
2. It is necessary to determine the purposes of the scan in order to have a better control of the amount of information, improve user experience and speed of analysis.
3. This new information can be incorporated in the process of extraction sequence as part of an optimisation process. The idea is to decrease the risk of extraction and to ensure the benefits creating robust extraction models.
4. As new source of information, HM opens new fields of study and can help to better understand and predict process such as blasting behaviour.
5. HM opens the search for new approaches to RM characterisation as the utilisation of reflectiveness to determine the type of material and ore grade using the same pulses of light that created the point clouds.



9. References

1. Goodman, R.E., *Introduction to rock mechanics*. Vol. 2. 1989: Wiley New York.
2. Maerz, N.H., J. Ibarra, and J.A. Franklin, *Overbreak and underbreak in underground openings Part I: measurement using the light sectioning method and digital image processing*. *Geotechnical & Geological Engineering*, 1996. **14**(4): p. 307-323.
3. Singh, S.P. and P. Xavier, *Causes, impact and control of overbreak in underground excavations*. *Tunnelling and Underground Space Technology*, 2005. **20**(1): p. 63-71.
4. Mawdesley, C., R. Trueman, and W. Whiten, *Extending the Mathews stability graph for open–slope design*. *Mining Technology*, 2001. **110**(1): p. 27-39.
5. Mathews, K., et al., *Prediction of stable excavation spans for mining at depths below 1000 m in hard rock*. CANMET DSS Serial No: 0sQ80-00081., Ottawa, 1981.
6. Villaescusa, E., *Geotechnical Design for Sublevel Open Stoping*. 2014.
7. Villaescusa, E., *Quantifying open slope performance*. *Proceedings of Mass Min*, 2004: p. 96-104.
8. Villaescusa, E., *Geotechnical design for dilution control in underground mining*. *Mine Planning and Equipment Selection*, 1998: p. 141-149.
9. Guido, S., M. Grenon, and P. Germain. *Slope Performance Assessment at the Goldcorp Eleonore Mine Using Bivariate Analysis*. in *ISRM AfriRock-Rock Mechanics for Africa*. 2017. International Society for Rock Mechanics and Rock Engineering.
10. Germain, P. and J. Hadjigeorgiou, *Influence of slope geometry and blasting patterns on recorded overbreak*. *International Journal of Rock Mechanics and Mining Sciences*, 1997. **34**(3-4): p. 115. e1-115. e12.
11. Palmstrom, A., E.J.T. Broch, and u.s. technology, *Use and misuse of rock mass classification systems with particular reference to the Q-system*. 2006. **21**(6): p. 575-593.
12. Barton, N., R. Lien, and J.J.R.m. Lunde, *Engineering classification of rock masses for the design of tunnel support*. 1974. **6**(4): p. 189-236.
13. Bieniawski, Z.T. and Z. Bieniawski, *Engineering rock mass classifications: a complete manual for engineers and geologists in mining, civil, and petroleum engineering*. 1989: John Wiley & Sons.

14. Lee, S. and Y. Choi, *Reviews of unmanned aerial vehicle (drone) technology trends and its applications in the mining industry*. Geosystem Engineering, 2016. **19**(4): p. 197-204.
15. Palmstrom, A., *Measurements of and correlations between block size and rock quality designation (RQD)*. Tunnelling and Underground Space Technology, 2005. **20**(4): p. 362-377.
16. Vallejos, J., et al. *Development of an integrated platform for stability analysis and design in sublevel stoping mines—MineRoc®*. in *Proceedings of the International Seminar on Design Methods in Underground Mining*. 2015. Australian Centre for Geomechanics.
17. Onederra, I. and G. Chitombo, *Design methodology for underground ring blasting*. Mining Technology, 2007. **116**(4): p. 180-195.
18. Da Gama, D. *Use of comminution theory to predict fragmentation of jointed rock masses subjected to blasting*. in *Proc. First Int. Symp. on Rock Frag. By Blasting, Lulea, Sweden*. 1983.
19. Cunningham, C. and A. Goetzsche, *The specification of blast damage limitations in tunnelling contracts*. Tunnelling and Underground Space Technology, 1990. **5**(3): p. 193-198.
20. Sanders, J.L., *On the Griffith-Irwin fracture theory*. 1959: Citeseer.
21. Kutter, H. and C. Fairhurst. *On the fracture process in blasting*. in *International Journal of Rock Mechanics and Mining Sciences & Geomechanics Abstracts*. 1971. Elsevier.
22. Far, M.S. and Y. Wang, *Probabilistic analysis of crushed zone for rock blasting*. Computers and Geotechnics, 2016. **80**: p. 290-300.
23. Torbica, S. and V. Lapčević, *Estimating extent and properties of blast-damaged zone around underground excavations*. Rem: Revista Escola de Minas, 2015. **68**(4): p. 441-453.
24. Bolkas, D., et al., *Detection of Rock Discontinuity Traces Using Terrestrial LiDAR Data and Space-Frequency Transforms*. Geotechnical and Geological Engineering: p. 1-21.
25. Slob, S., et al. *Fracture mapping using 3D laser scanning techniques*. in *11th ISRM Congress*. 2007. International Society for Rock Mechanics.
26. Brzovic, A., *Integrated photogrammetry and discrete fracture network modeling to determine rock structure around excavations at the El Teniente mine*. 2017.

27. Fekete, S., *Geotechnical applications of LiDAR for geomechanical characterization in drill and blast tunnels and representative 3-dimensional discontinuum modelling*. 2010.
28. Vazaios, I., et al., *A DFN-LiDAR-optical sensor method for the estimation of rockmass conditions in underground projects*.
29. Lato, M.J., M.S. Diederichs, and D.J. Hutchinson, *Bias Correction for View-limited Lidar Scanning of Rock Outcrops for Structural Characterization*. *Rock Mechanics and Rock Engineering*, 2010. **43**(5): p. 615-628.
30. Priest, S.D., *Discontinuity analysis for rock engineering*. 2012: Springer Science & Business Media.
31. Akbari, M., et al., *Blastability evaluation for rock mass fragmentation in Iran central iron ore mines*. *International Journal of Mining Science and Technology*, 2015. **25**(1): p. 59-66.
32. Benton, D., et al. *Photogrammetry in underground mining ground control—Lucky Friday mine case study*. in *Proceedings of the Eighth International Conference on Deep and High Stress Mining*. 2017. Australian Centre for Geomechanics.
33. Lato, M., et al., *Rock bench: Establishing a common repository and standards for assessing rockmass characteristics using LiDAR and photogrammetry*. *Computers & Geosciences*, 2013. **50**: p. 106-114.
34. Bonilla-Sierra, V., et al., *Rock slope stability analysis using photogrammetric data and DFN–DEM modelling*. *Acta Geotechnica*, 2015. **10**(4): p. 497-511.
35. Baltsavias, E.P., *A comparison between photogrammetry and laser scanning*. *ISPRS Journal of photogrammetry and Remote Sensing*, 1999. **54**(2-3): p. 83-94.
36. Amann, M.-C., et al., *Laser ranging: a critical review of unusual techniques for distance measurement*. *Optical engineering*, 2001. **40**(1): p. 10-20.
37. Riquelme, A.J., et al., *A new approach for semi-automatic rock mass joints recognition from 3D point clouds*. *Computers & Geosciences*, 2014. **68**: p. 38-52.
38. Lato, M., *Geotechnical applications of LiDAR pertaining to geomechanical evaluation and hazard identification*. 2010.
39. Cacciari, P.P. and M.M. Futai, *Mapping and characterization of rock discontinuities in a tunnel using 3D terrestrial laser scanning*. *Bulletin of Engineering Geology and the Environment*, 2016. **75**(1): p. 223-237.
40. Riquelme, A.J., A. Abellán, and R. Tomás, *Discontinuity spacing analysis in rock masses using 3D point clouds*. *Engineering Geology*, 2015. **195**: p. 185-195.

41. Jordá Bordehore, L., et al., *Comparing manual and remote sensing field discontinuity collection used in kinematic stability assessment of failed rock slopes*. 2017.
42. Barla, G. and M. Barla, *Continuum and discontinuum modelling in tunnel engineering*. Rudarsko-Geolosko-Naftni Zbornik, 2000. **12**(1): p. 45.
43. Dove, J.E., et al., *Remote characterization of rock exposures using terrestrial LIDAR*, in *GeoCongress 2008: Characterization, Monitoring, and Modeling of GeoSystems*. 2008. p. 484-491.
44. Gigli, G. and N. Casagli, *Semi-automatic extraction of rock mass structural data from high resolution LIDAR point clouds*. International Journal of Rock Mechanics and Mining Sciences, 2011. **48**(2): p. 187-198.
45. Vöge, M., M.J. Lato, and M.S. Diederichs, *Automated rockmass discontinuity mapping from 3-dimensional surface data*. Engineering Geology, 2013. **164**: p. 155-162.
46. Chen, J., H. Zhu, and X. Li, *Automatic extraction of discontinuity orientation from rock mass surface 3D point cloud*. Computers & Geosciences, 2016. **95**: p. 18-31.
47. Kaasalainen, S., et al., *Analysis of incidence angle and distance effects on terrestrial laser scanner intensity: Search for correction methods*. Remote Sensing, 2011. **3**(10): p. 2207-2221.
48. Freire, G. and R. Cota. *Capture of images in inaccessible areas in an underground mine using an unmanned aerial vehicle*. in *Proceedings of the First International Conference on Underground Mining Technology*. 2017. Australian Centre for Geomechanics.
49. Guoquan, W.Y.L.H.S.J.M.M., *Modeling and Stability Analysis of the Mined-Out Area in Underground Mine by CMS [J]*. 2009. **8**: p. 003.
50. Luo, Z.-q., et al., *Cavity 3D modeling and correlative techniques based on cavity monitoring*. 2008. **15**(5): p. 639-644.
51. Guo, J., et al., *Application of cavity monitoring system in underground mines*. 2005: p. S1.
52. Ahmed, S.N., et al., *New methods and equipment for three-dimensional laser scanning, mapping and profiling underground mine cavities*, in *Proceedings of the First International Conference on Underground Mining Technology*, M. Hudyma and Y. Potvin, Editors. 2017, Australian Centre for Geomechanics: Sudbury. p. 467-473.
53. Hustrulid, W.A., W.A. Hustrulid, and R.C. Bullock, *Underground mining methods: Engineering fundamentals and international case studies*. 2001: SME.

54. Chmelina, K., et al., *Drone Based Deformation Monitoring at the Tunnel Project Zentrum am Berg*. 2018.
55. Dewez, T.J., et al., *FACETS: A CLOUDCOMPARE PLUGIN TO EXTRACT GEOLOGICAL PLANES FROM UNSTRUCTURED 3D POINT CLOUDS*. International Archives of the Photogrammetry, Remote Sensing & Spatial Information Sciences, 2016. **41**.
56. Riquelme, A., et al., *Automatic Mapping of Discontinuity Persistence on Rock Masses Using 3D Point Clouds*. 2018.
57. Dominy, S.C., et al., *Integrating the theory of sampling into underground mine grade control strategies*. 2018.
58. Van Der Merwe, H. *Sirovision: A proposed solution for the implementation of a digital geological mapping system at AngloGold Ashanti's Moab Khotsong mine*. in *Proceedings of the World Gold Conference, Misty Hills, South Africa*. 2009.
59. Wu, X., et al., *Top 10 algorithms in data mining*. 2008. **14**(1): p. 1-37.
60. Bassier, M., et al., *Semi-automated Creation of Accurate FE Meshes of Heritage Masonry Walls from Point Cloud Data*, in *Structural Analysis of Historical Constructions*. 2019, Springer. p. 305-314.

Appendix A

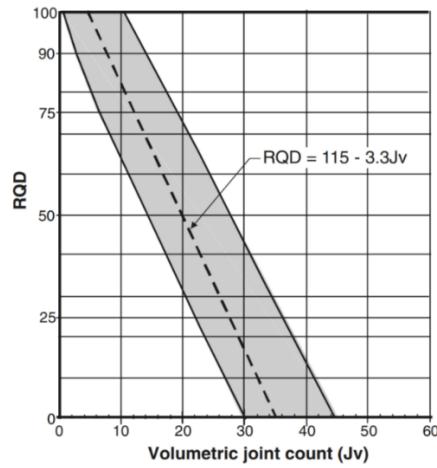


Figure 48. Relationship between Volumetric joint count and RQD [2]

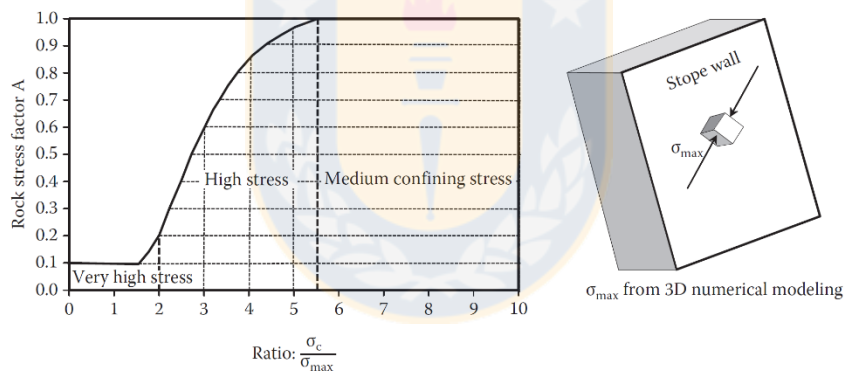


Figure 49. Stress factor A, Stability number [2]

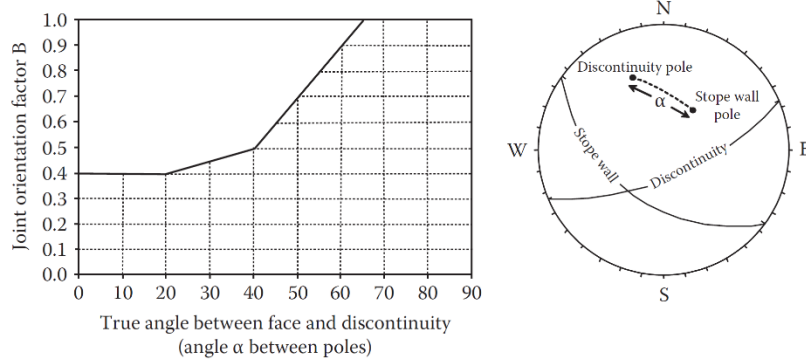


Figure 50. Influence of joint orientation - factor B, Stability number [2]

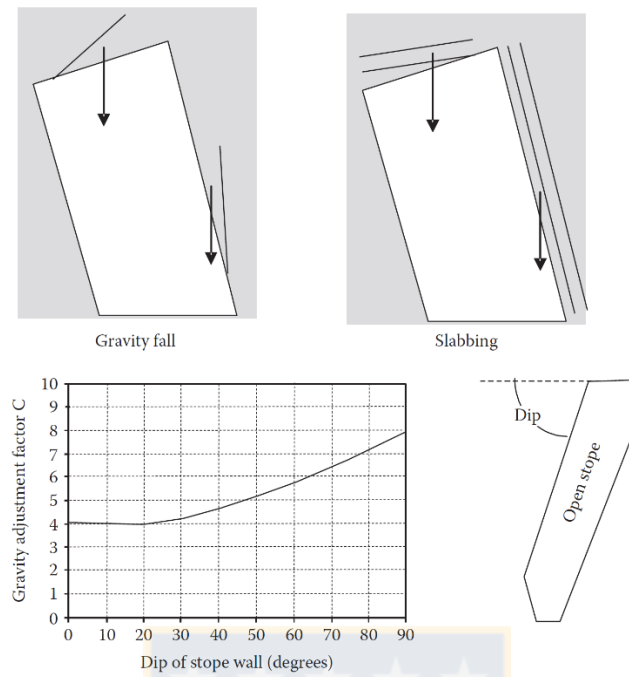


Figure 51. Determination gravity effect - Factor C, Stability number [2]

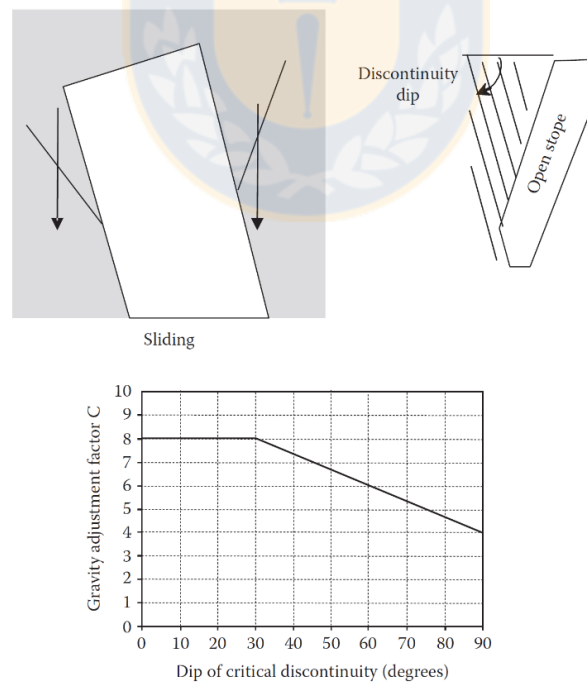


Figure 52. Determination of sliding effect on critical joint - Factor C, Stability number [2]

Appendix B

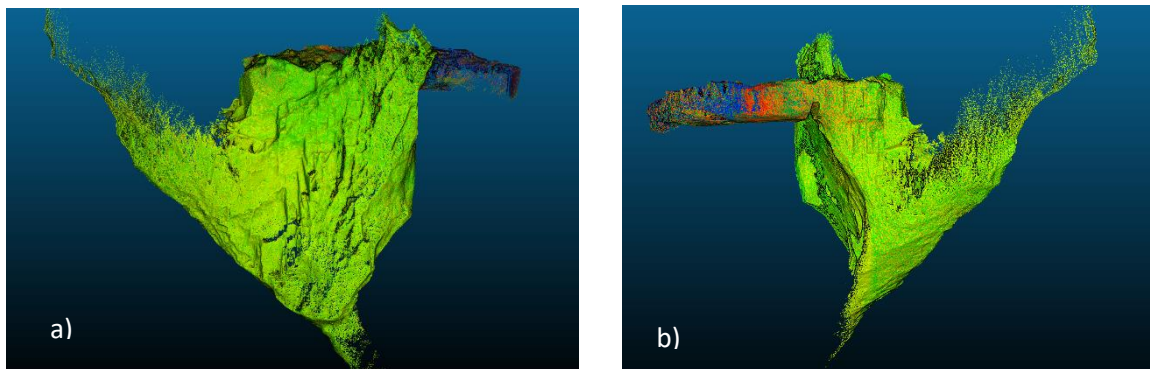


Figure 53. a) Isometric view Stope A; and b) HW view of Stope A

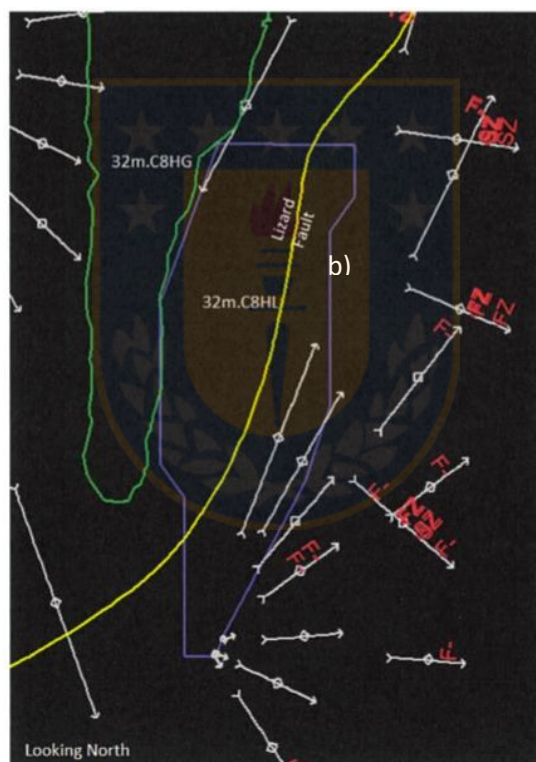


Figure 54. Geologic structures identified with core logging, lateral view

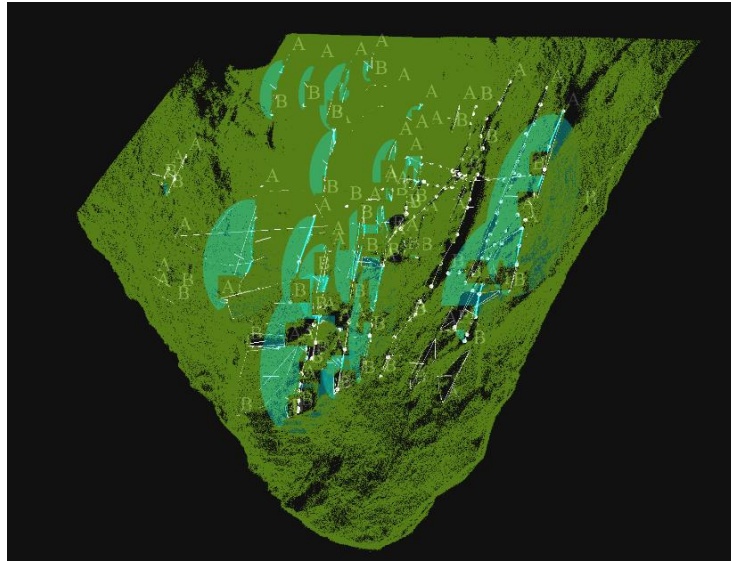


Figure 55. Set 1, HW Case Study 1

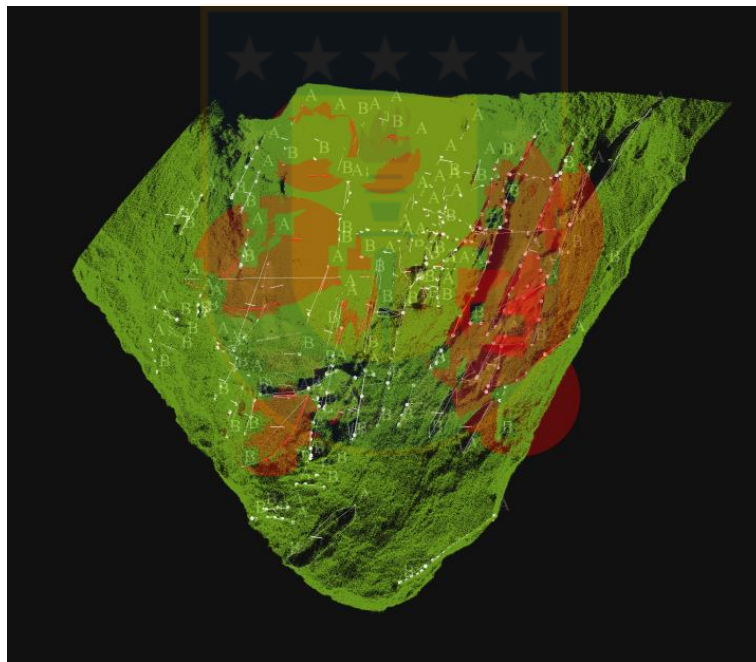


Figure 56. Set 2, HW Case Study 1

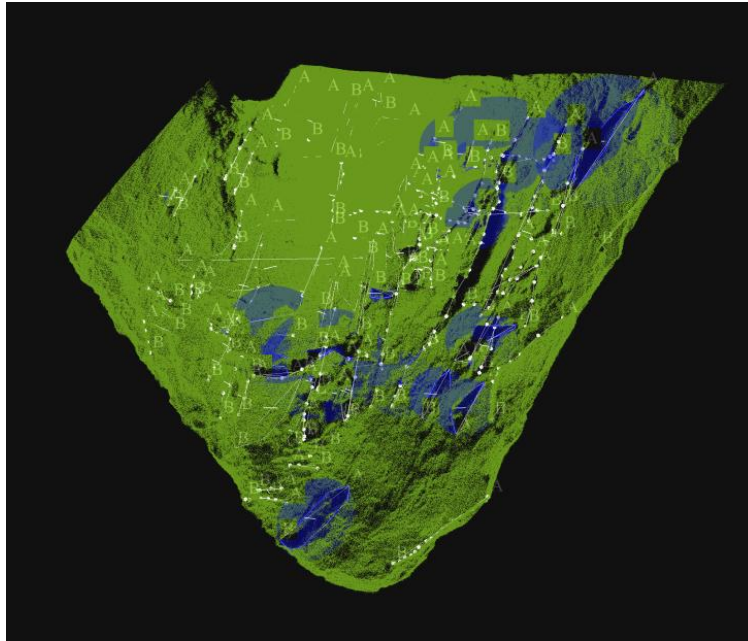


Figure 57. Set 3, HW Case Study 1



Appendix C

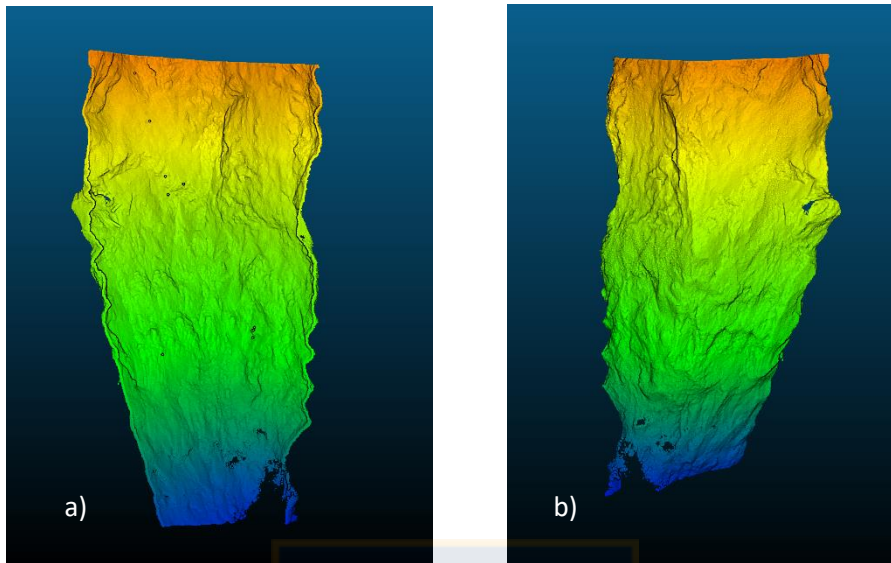


Figure 58. UB Section a) Inside view; and b) Outside view.

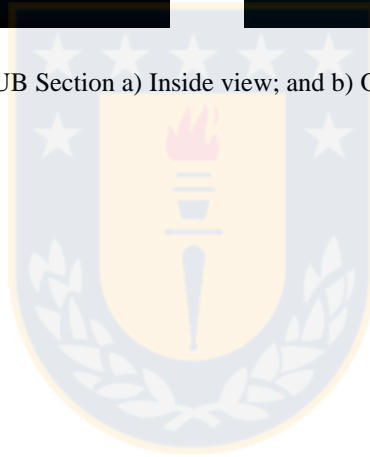


Table 13. GS information obtained with Sirovision, Case Study 2

| ID | X | Y | Z | Type | Dip | Dip Direction | Plunge | Trend | Persistence | Orientation | End to End |
|----|----------|----------|---------|--------|------|---------------|--------|-------|-------------|-------------|------------|
| 1 | 1998.321 | 5264.731 | 963.791 | Trace | 80.1 | 33 | 9.9 | 213 | 15.369 | N/A | 15.556 |
| 2 | 1996.36 | 5265.942 | 958.729 | Trace | 74.4 | 4.9 | 15.6 | 184.9 | 3.121 | N/A | 3.314 |
| 3 | 1993.629 | 5265.007 | 955.403 | Trace | 73.7 | 26.2 | 16.3 | 206.2 | 3.569 | N/A | 3.814 |
| 4 | 1992.765 | 5265.211 | 952.187 | Trace | 77.2 | 41.7 | 12.8 | 221.7 | 3.661 | N/A | 3.82 |
| 5 | 1994.195 | 5267.978 | 953.232 | Trace | 72.7 | 36.5 | 17.3 | 216.5 | 3.616 | N/A | 3.754 |
| 6 | 1998.724 | 5265.779 | 962.897 | Trace | 77 | 27.3 | 13 | 207.3 | 5.451 | N/A | 5.635 |
| 7 | 1996.868 | 5274.629 | 951.739 | Trace | 75.3 | 12.7 | 14.7 | 192.7 | 5.232 | N/A | 5.29 |
| 8 | 1994.634 | 5268.358 | 954.192 | Trace | 68.6 | 25.5 | 21.4 | 205.5 | 2.068 | N/A | 2.069 |
| 9 | 2001.12 | 5270.76 | 964.898 | Trace | 69 | 10.1 | 21 | 190.1 | 9.706 | N/A | 9.862 |
| 10 | 1999.259 | 5273.018 | 956.896 | Trace | 67.7 | 197.6 | 22.3 | 17.6 | 2.432 | N/A | 2.473 |
| 11 | 2000.715 | 5278.3 | 957.884 | Trace | 57.5 | 305.4 | 32.5 | 125.4 | 6.472 | N/A | 6.531 |
| 12 | 1999.027 | 5278.878 | 954.307 | Trace | 57.5 | 325.8 | 32.5 | 145.8 | 8.361 | N/A | 9.059 |
| 13 | 1993.18 | 5272.347 | 946.396 | Trace | 62.6 | 341.8 | 27.4 | 161.8 | 3.822 | N/A | 4.031 |
| 14 | 1997.566 | 5269.194 | 958.7 | Trace | 71.6 | 358.6 | 18.4 | 178.6 | 3.597 | N/A | 3.718 |
| 15 | 1999.532 | 5267.512 | 964.006 | Trace | 88.9 | 230.2 | 1.1 | 50.2 | 5.045 | N/A | 5.213 |
| 16 | 1995.26 | 5268.445 | 955.165 | Trace | 65.4 | 2.9 | 24.6 | 182.9 | 2.4 | N/A | 2.508 |
| 17 | 1995.18 | 5270.718 | 953.313 | Trace | 85.6 | 48.9 | 4.4 | 228.9 | 1.881 | N/A | 1.899 |
| 18 | 1994.898 | 5270.13 | 953.099 | Trace | 78 | 48 | 12 | 228 | 1.511 | N/A | 1.561 |
| 19 | 1999.206 | 5267.771 | 962.301 | Trace | 76.7 | 295.3 | 13.3 | 115.3 | 10.593 | 65.6 | 13.739 |
| 20 | 1995.926 | 5273.931 | 951.496 | Trace | 66.4 | 357.8 | 23.6 | 177.8 | 3.975 | N/A | 4.011 |
| 21 | 1995.65 | 5273.752 | 951.287 | Trace | 66.6 | 353.8 | 23.4 | 173.8 | 3.78 | N/A | 3.827 |
| 22 | 1993.305 | 5267.346 | 950.996 | Trace | 41.2 | 140.3 | 48.8 | 320.3 | 2.549 | N/A | 2.56 |
| 23 | 1993.046 | 5267.594 | 950.087 | Trace | 29.9 | 223 | 60.1 | 43 | 2.502 | N/A | 2.596 |
| 24 | 1999.131 | 5263.351 | 967.626 | Trace | 79.4 | 29.3 | 10.6 | 209.3 | 12.923 | N/A | 13.223 |
| 25 | 1993.073 | 5268.216 | 949.414 | Trace | 61.1 | 292.1 | 28.9 | 112.1 | 4.847 | 73.7 | 6.218 |
| 26 | 2000.882 | 5275.404 | 957.775 | Plane* | 67.9 | 279.1 | 22.1 | 99.1 | 7.355 | 8.8 | 19.577 |

| | | | | | | | | | | | |
|-----------|----------|----------|---------|--------|------|-------|------|-------|--------|------|--------|
| 27 | 2002.684 | 5270.068 | 972.011 | Plane* | 81.2 | 46.5 | 8.8 | 226.5 | 2.709 | 17.1 | 5.748 |
| 28 | 2003.003 | 5275.362 | 963.443 | Plane* | 73.9 | 286.1 | 16.1 | 106.1 | 4.303 | 15.5 | 11.501 |
| 29 | 1997.443 | 5267.861 | 959.292 | Plane* | 71.8 | 293.7 | 18.2 | 113.7 | 11.596 | 9.5 | 32.681 |
| 30 | 2002.593 | 5269.146 | 973.556 | Plane* | 83.7 | 287.3 | 6.3 | 107.3 | 11.997 | 17.1 | 28.797 |
| 31 | 1998.813 | 5261.212 | 968.6 | Plane* | 75.3 | 281.9 | 14.7 | 101.9 | 5.811 | 11.2 | 15.884 |
| 32 | 1994.484 | 5271.627 | 950.221 | Plane* | 76.7 | 287 | 13.3 | 107 | 5.033 | 11.3 | 14.271 |
| 33 | 1997.99 | 5277.854 | 951.279 | Trace | 58.4 | 241.4 | 31.6 | 61.4 | 5.493 | N/A | 6.225 |
| 34 | 1993.86 | 5266.803 | 953.013 | Trace | 73.5 | 29.6 | 16.5 | 209.6 | 2.604 | N/A | 2.612 |
| 35 | 2003.303 | 5272.437 | 968.99 | Trace | 42.8 | 340.9 | 47.2 | 160.9 | 1.871 | N/A | 1.934 |
| 36 | 2005.366 | 5274.976 | 986.444 | Trace | 66.8 | 23.2 | 23.2 | 203.2 | 1.91 | N/A | 1.92 |
| 37 | 2004.664 | 5274.944 | 989.468 | Trace | 67.8 | 338 | 22.2 | 158 | 3.661 | N/A | 3.663 |
| 38 | 2004.992 | 5275.451 | 986.967 | Trace | 57.6 | 11 | 32.4 | 191 | 1.784 | N/A | 1.87 |
| 39 | 2005.534 | 5274.388 | 986.343 | Trace | 61.2 | 16.6 | 28.8 | 196.6 | 3.498 | N/A | 3.765 |

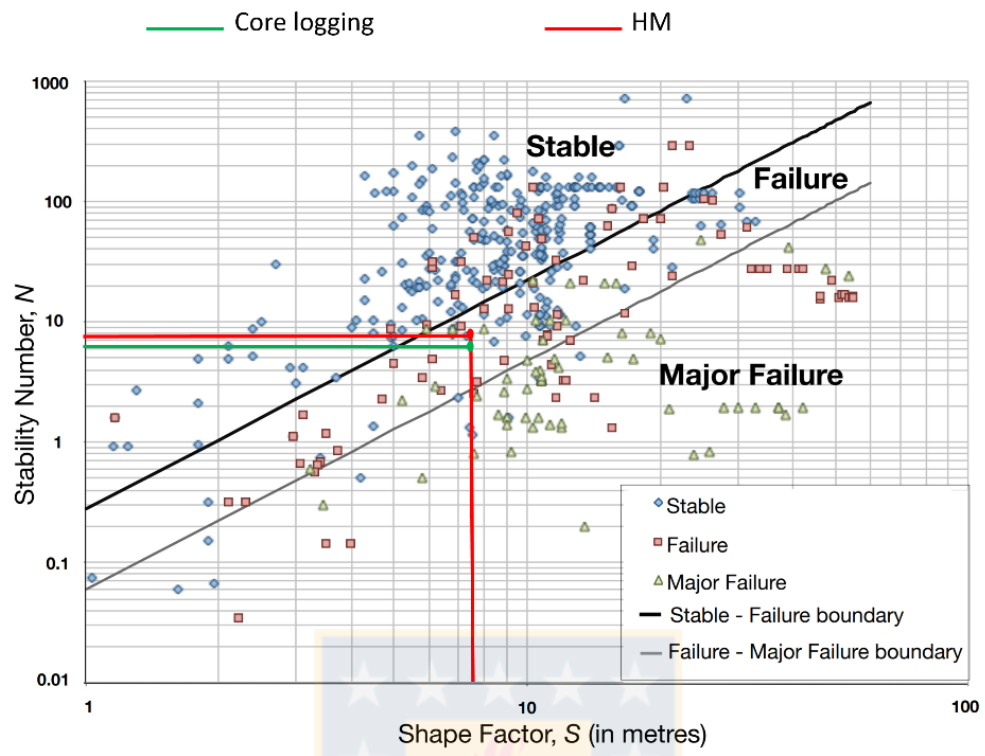


Figure 59. Mathew's Graph Analysis, Study Case 2

Appendix D

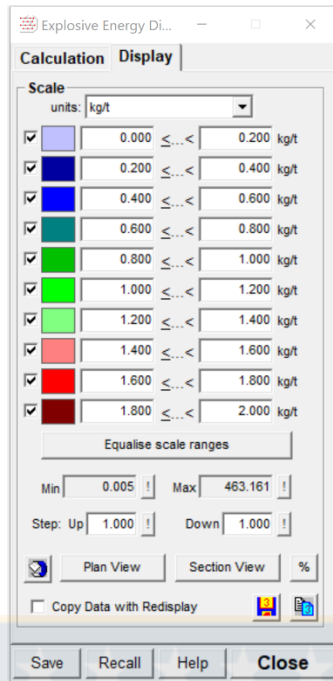
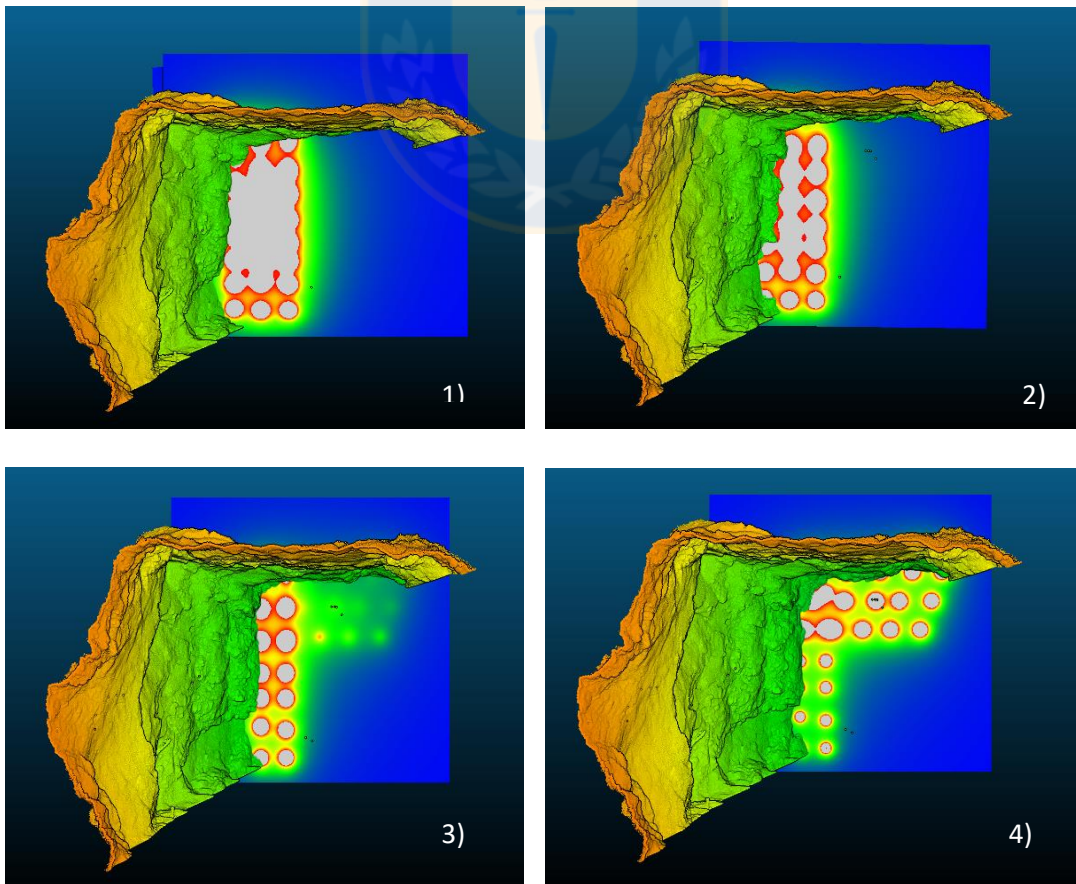


Figure 60. JKSimblast Energy distribution scale



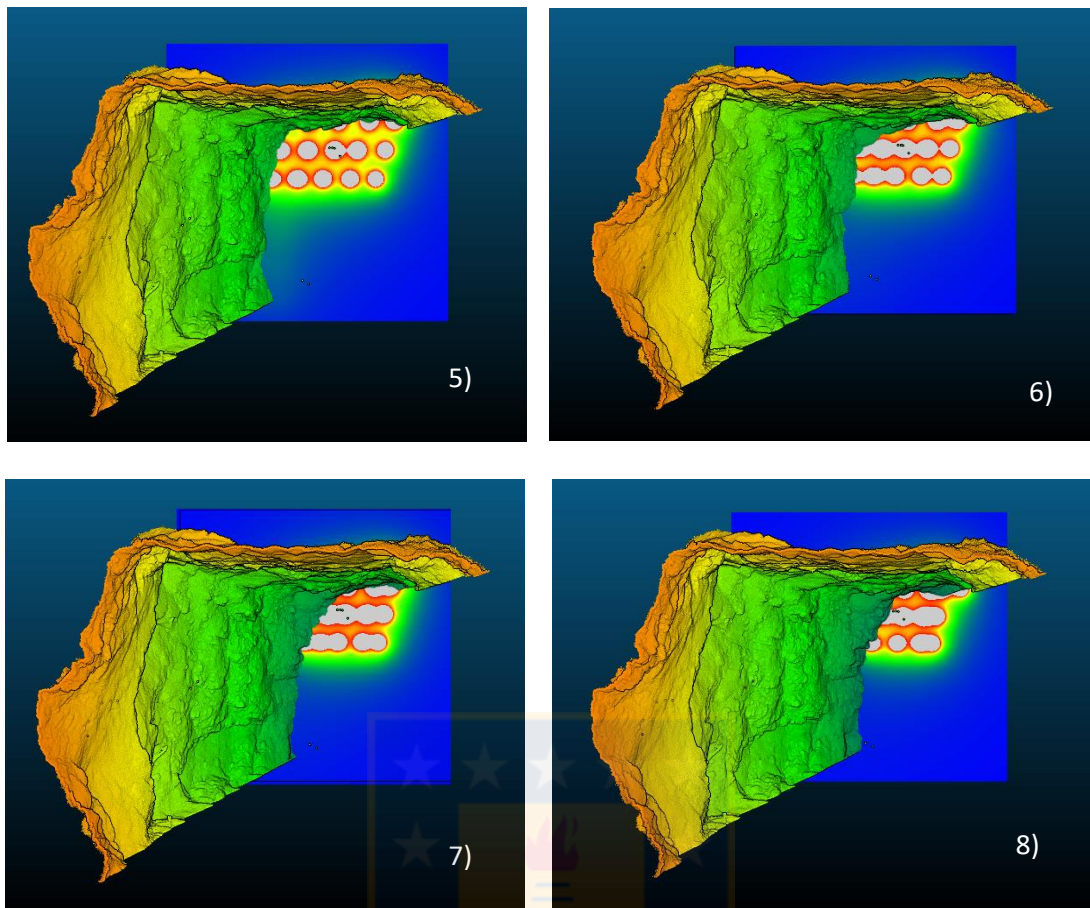
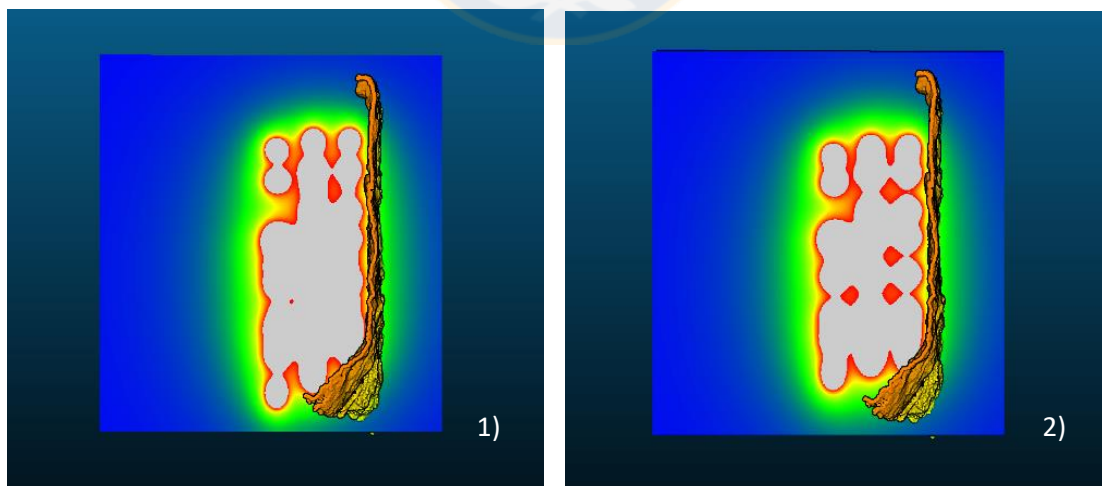


Figure 61. Plan view energy distribution UB zone; every 4 meters from 314mLv until 282mLv



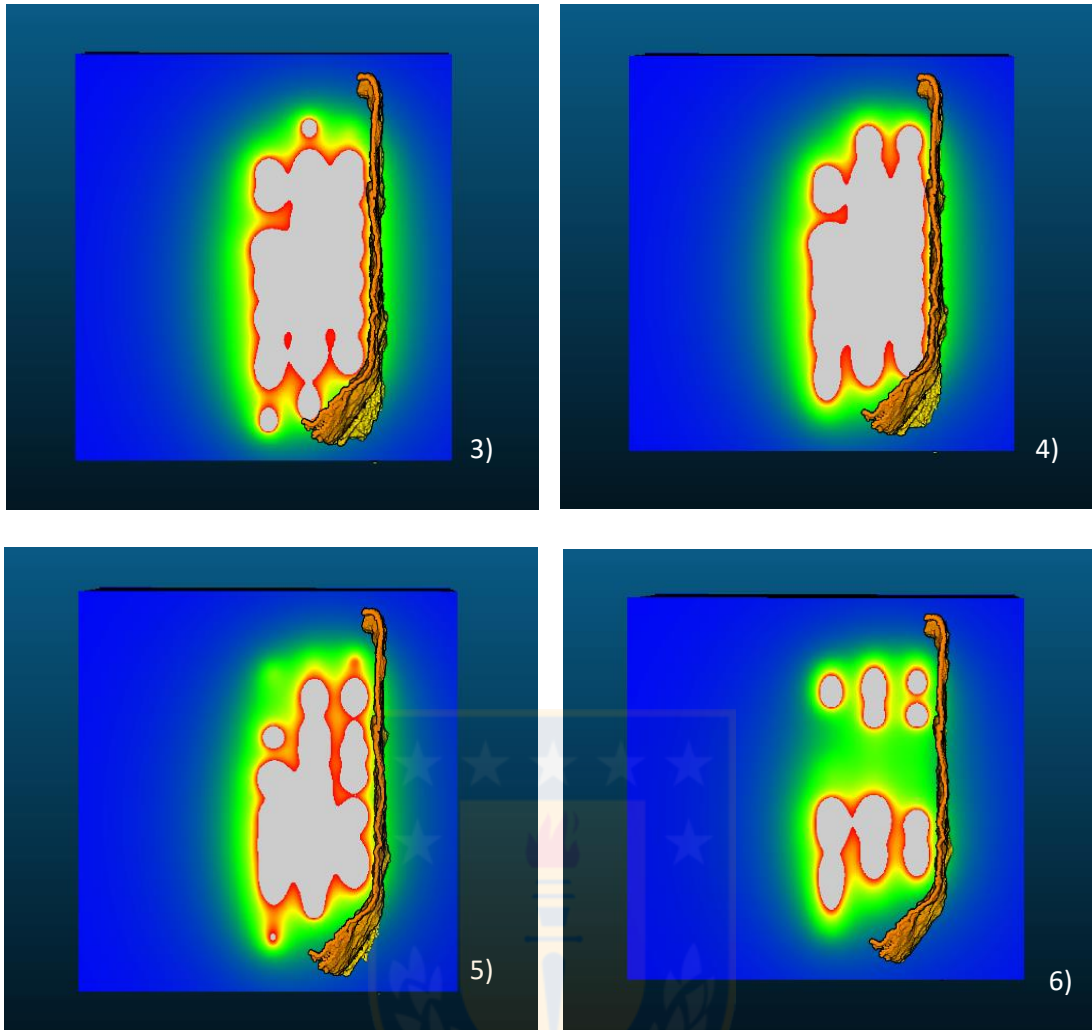


Figure 62. Plan view energy distribution " Good Performance" zone; every 4 meters from 264mLv until 280mLv

Appendix E

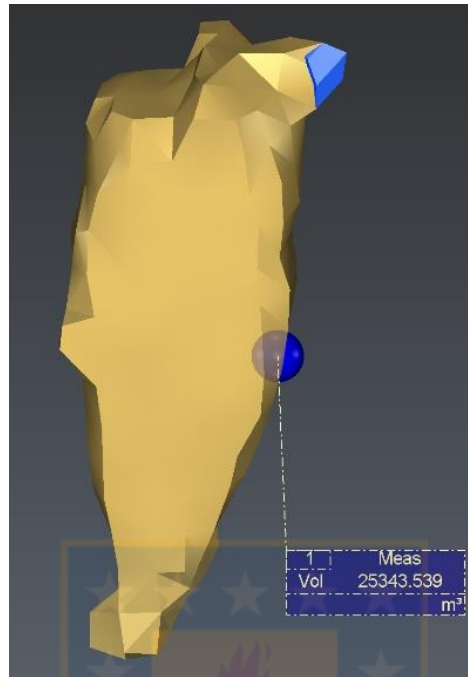


Figure 63. Volume measurement with lower density and faster interpolation process

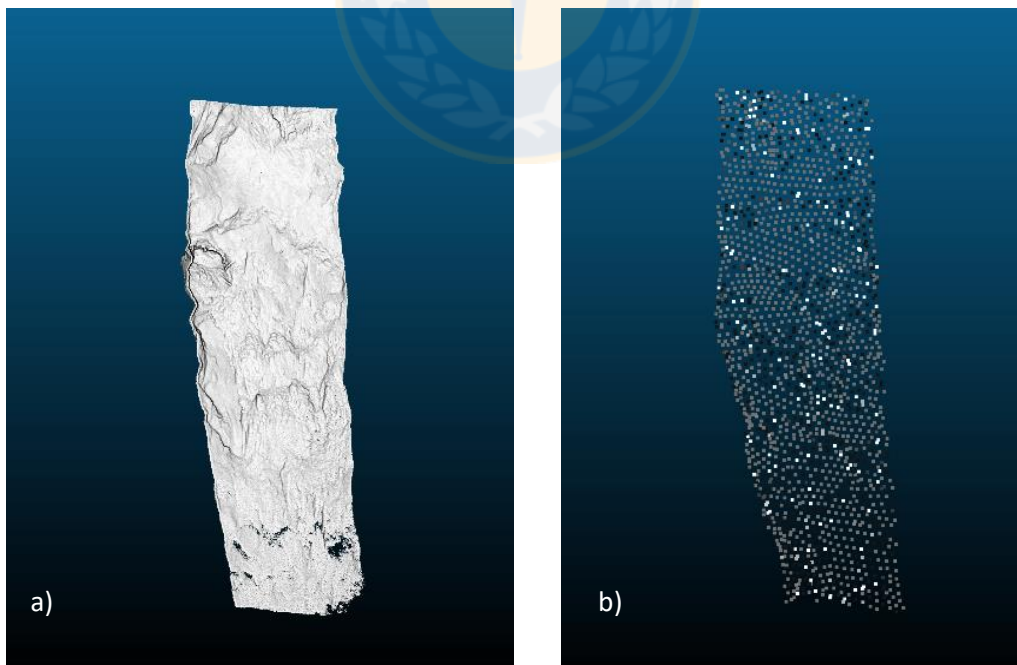


Figure 64. Difference in the point cloud density; a) HM scan; and b) CSM scan

Appendix F

Equation 6. Distance between two points in 3D space

For $P1 = (x_1, y_1, z_1)$ and $P2 = (x_2, y_2, z_2)$, the distance is between them is as follow:

$$d(P1, P2) = \sqrt{(x_1 - x_2)^2 + (y_1 - y_2)^2 + (z_1 - z_2)^2}$$

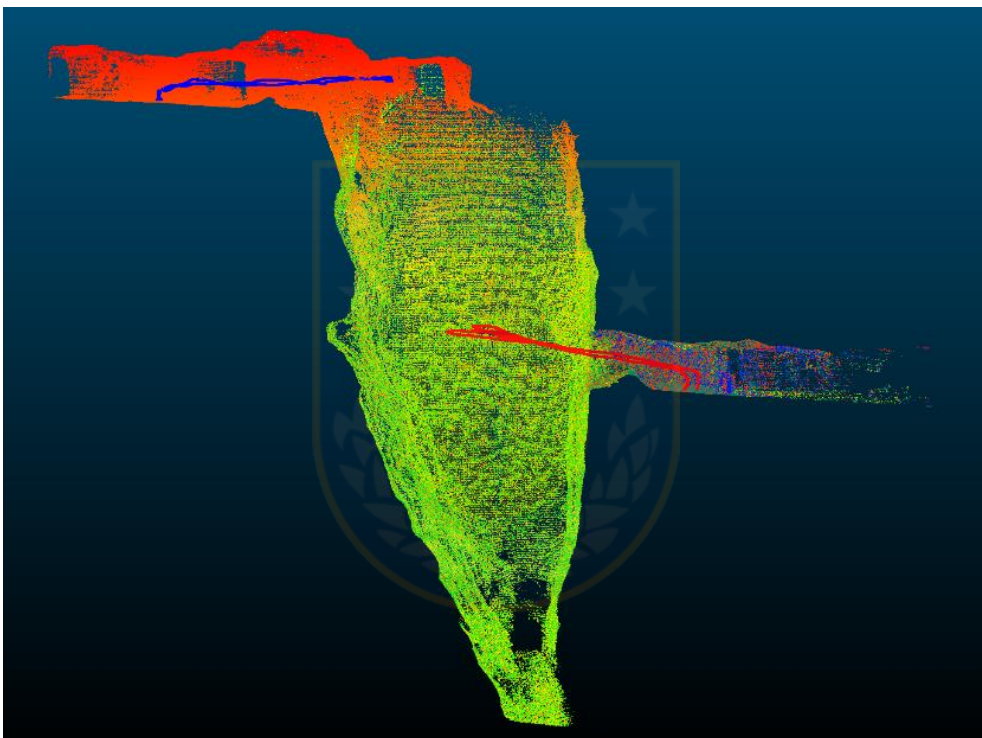


Figure 65. Drone trajectories, Case 2

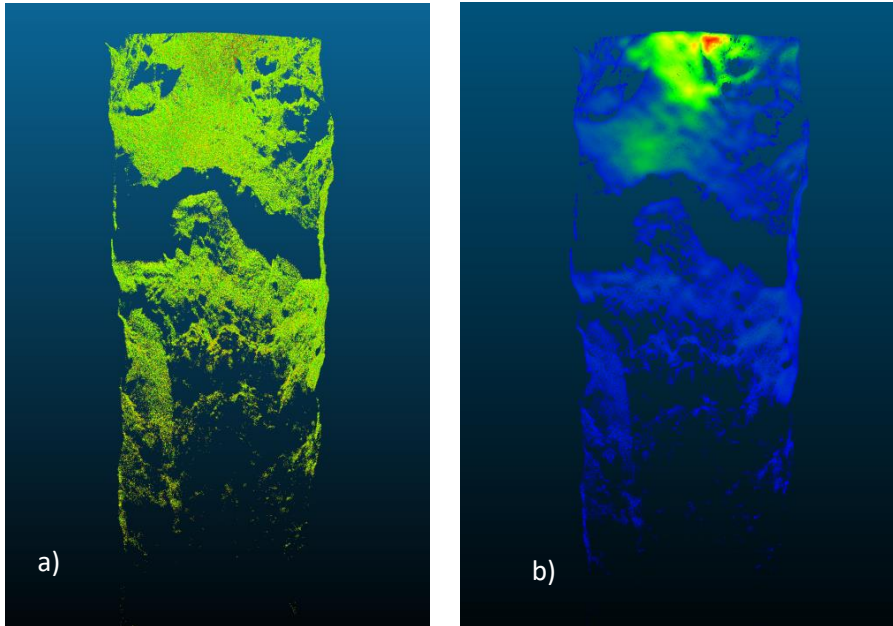


Figure 66. First scan; a) Point cloud results; and b) Point cloud density, Case 2

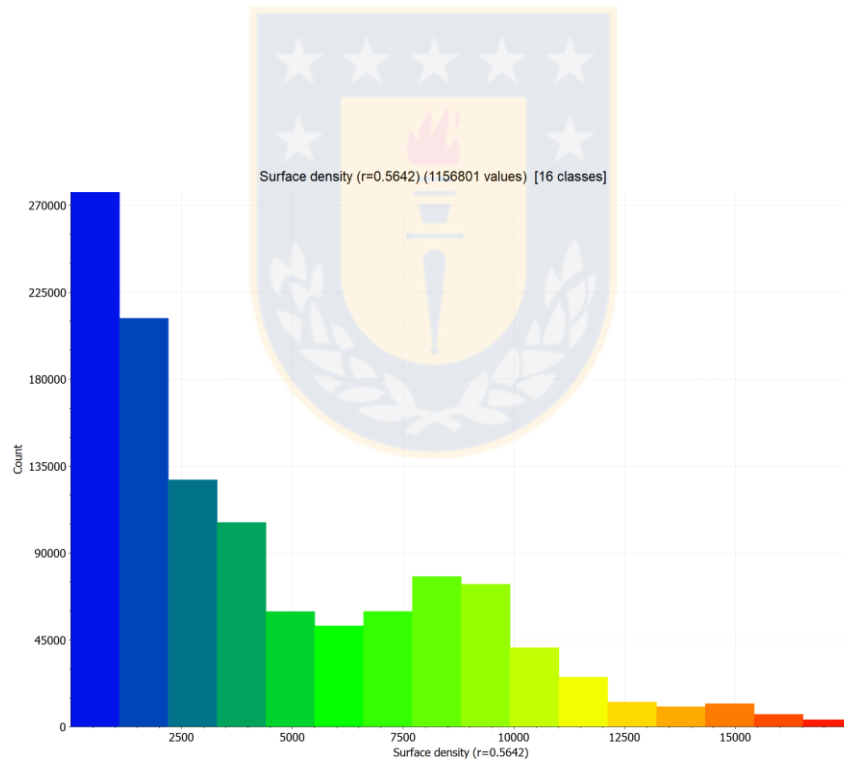


Figure 67. First scan density distribution, Case 2

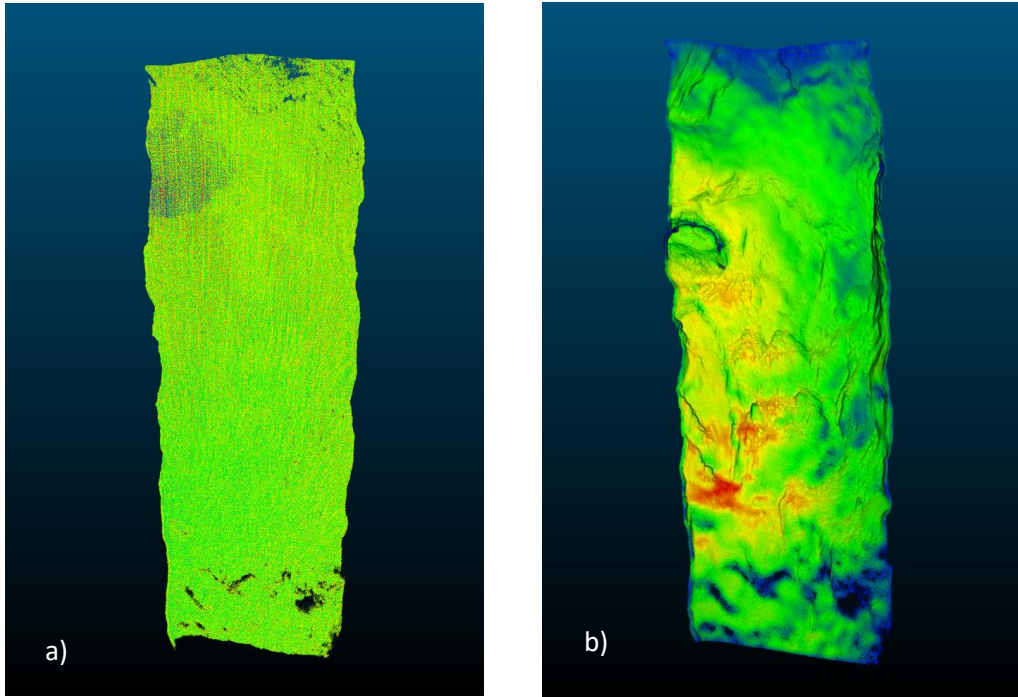


Figure 68. Second scan; a) Point cloud results; and b) Point cloud density, Case 2

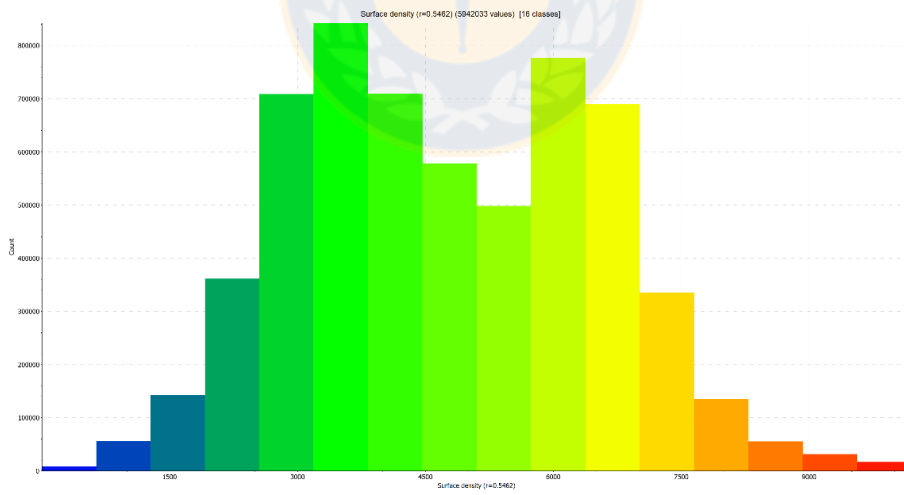


Figure 69. Second scan density distribution, Case 2

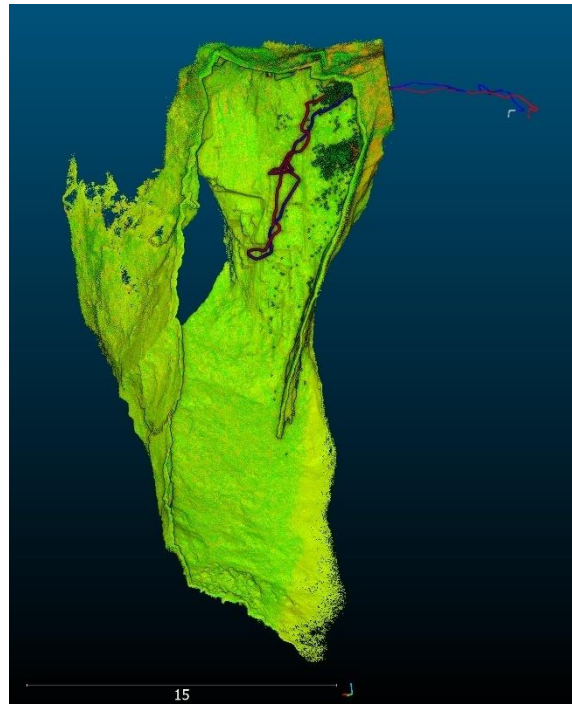


Figure 70. Drone trajectory, Case 1

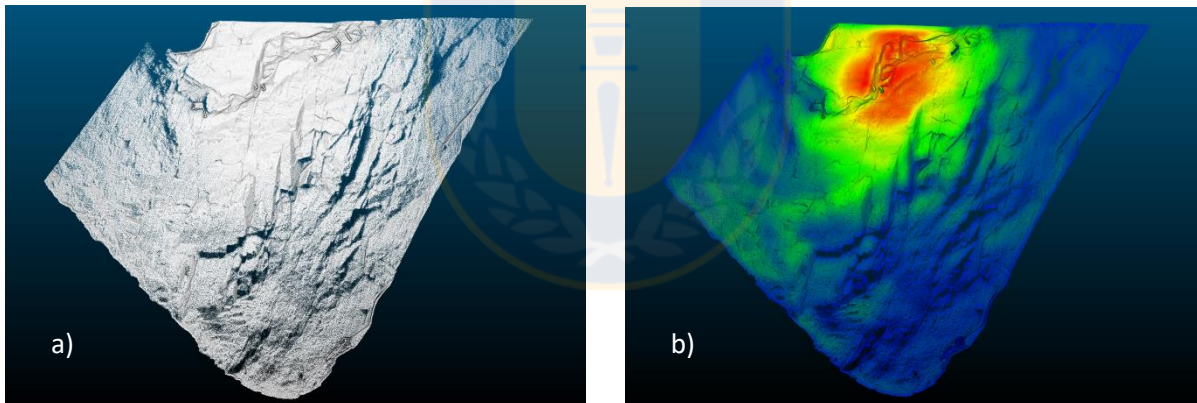


Figure 71. HM scan; a) Point cloud results; and b) Point cloud density, Case 1

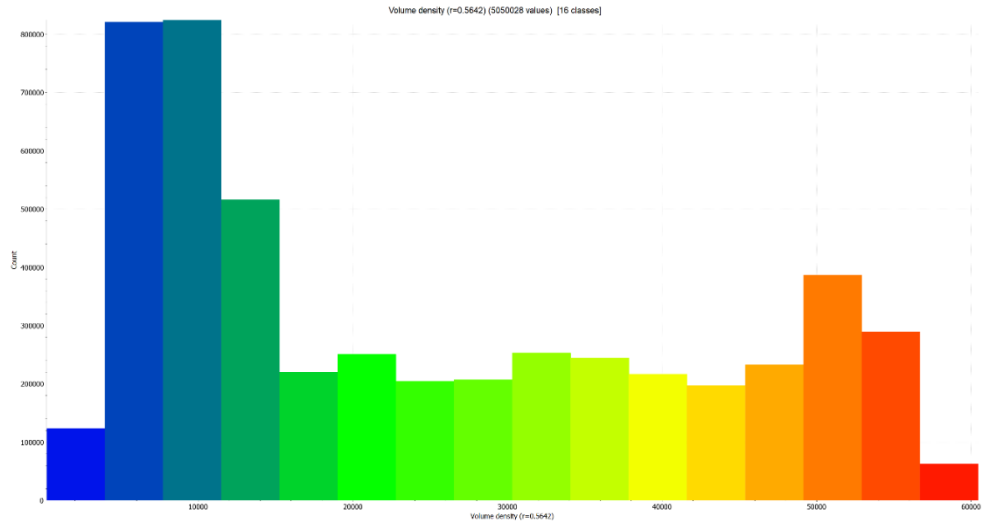


Figure 72. HM scan density distribution, Case 1

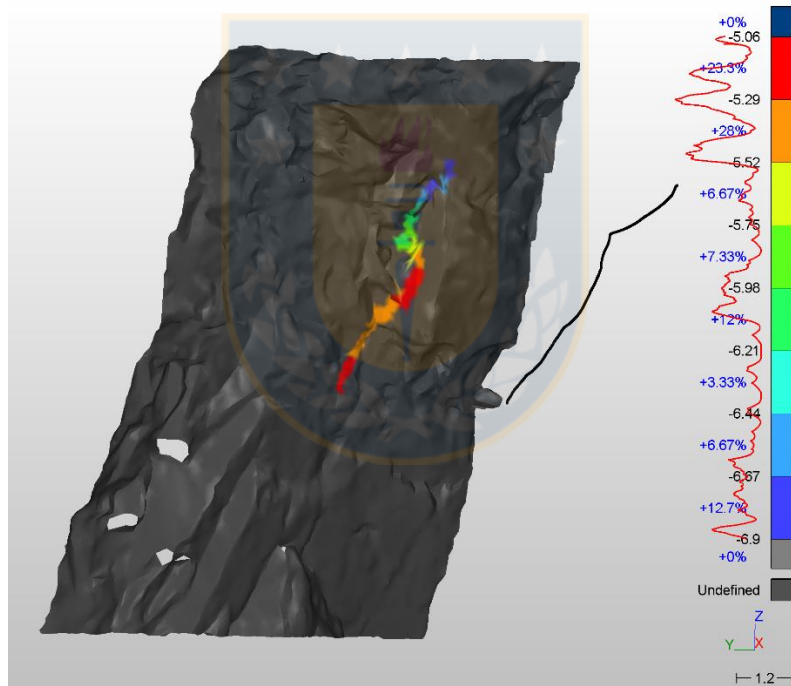


Figure 73. Range calculation for Track 1

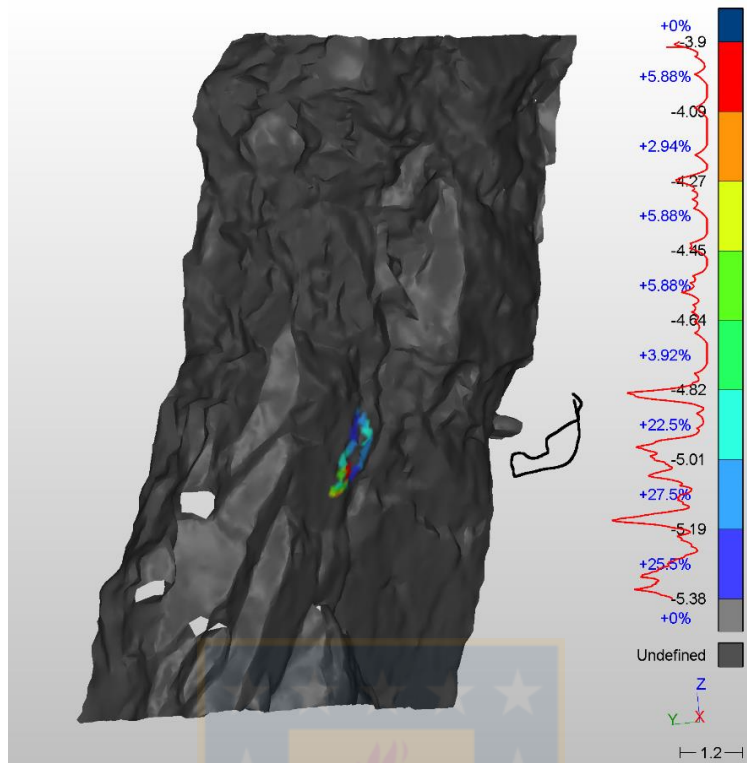


Figure 74. Range calculation for Track 2

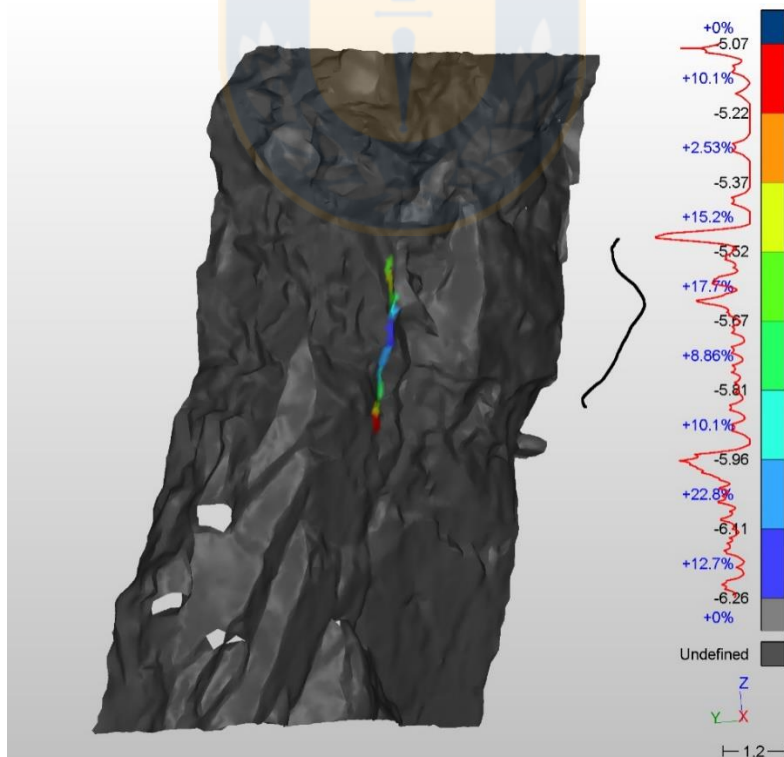


Figure 75. Range calculation for Track 3